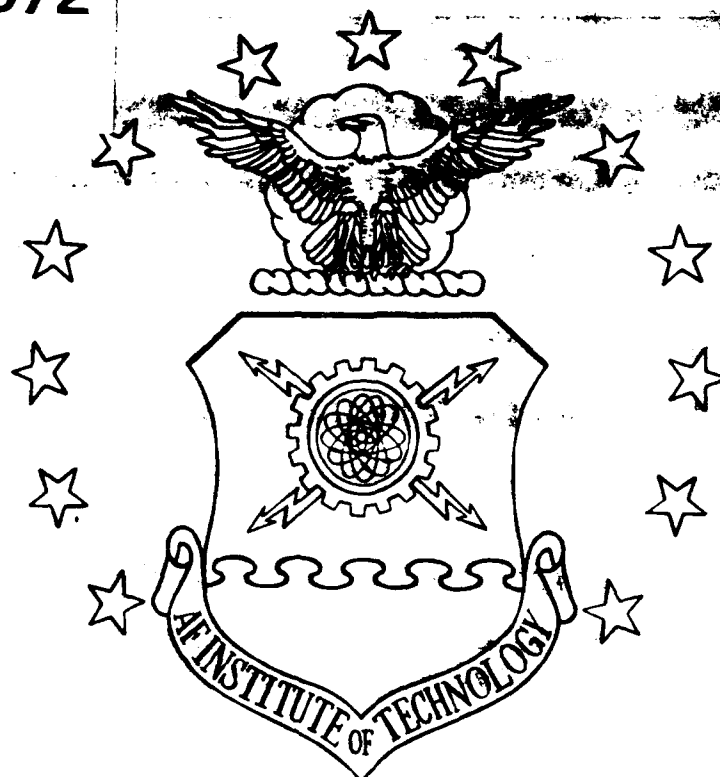


AD-A270 672



EXCITED ATOMIC BROMINE
ENERGY TRANSFER
AND QUENCHING MECHANISMS

DISSERTATION

Ray O. Johnson
Captain, USAF

AFIT DS/ENP/93-05

DTIC
ELECTE
OCT. 12 1993
S B D

DEPARTMENT OF THE AIR FORCE
AIR UNIVERSITY

AIR FORCE INSTITUTE OF TECHNOLOGY

Wright-Patterson Air Force Base, Ohio

DISTRIBUTION STATEMENT
Approved for public release
Distribution Unlimited

AFIT/DS/ENP/93-05

EXCITED ATOMIC BROMINE
ENERGY TRANSFER
AND QUENCHING MECHANISMS

DISSERTATION

Ray O. Johnson
Captain, USAF

AFIT/DS/ENP/93-05

Approved for public release; distribution unlimited

93 10 8 150

93-23996



**EXCITED ATOMIC BROMINE
ENERGY TRANSFER
AND QUENCHING MECHANISMS**

DISSERTATION

Presented to the Faculty of the School of Engineering
of the Air Force Institute of Technology

Air University

In Partial Fulfillment of the
Requirements for the Degree of
Doctor of Philosophy

Ray O. Johnson, B.S., M.S.
Captain, USAF

Accession For	
NTIS GRA&I	<input checked="checked" type="checkbox"/>
DTIC TAB	<input type="checkbox"/>
Unannounced	<input type="checkbox"/>
Justification	
By	
Distribution/	
Availability Codes	
Dist	Avail and/or Special
A-1	

August 1993

DTIC QUALITY INSPECTED 9

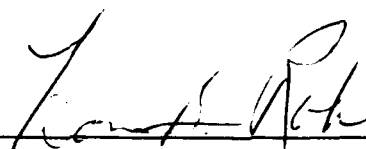
Approved for public release; distribution unlimited

**EXCITED ATOMIC BROMINE
ENERGY TRANSFER
AND QUENCHING MECHANISMS**

Ray O. Johnson, B.S., M.S.

Captain, USAF


Approved:


Dr. Won B. Roh, Chairman

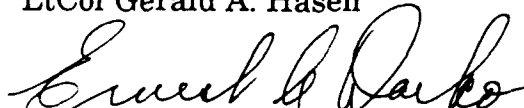
27 Aug 93


Maj Glen P. Perram

27 Aug 93


LtCol Gerald A. Hasen

24 Aug 93


Dr. Ernest A. Dorko

19 Aug 93


Dr. David E. Weeks

23 Aug 93

Accepted:



Dean, School of Engineering

Preface

Before recognizing those who made this scientific research possible, it is important to point out a very significant fact relative to this and to *all* science and engineering; *details matter*. Overlooked or ignored details make the difference between research success and failure.

This author sincerely thanks the Phillips Laboratory and his committee members for all of the assistance and support provided during this research effort. The author believes that the loss of any of the above constituents would have degraded the investigation.

Dr. Ernest A. Dorko provided the initial finances which began this area of research at AFIT. His continued support on this project is appreciated, and his continuing interest is necessary to insure Air Force-sponsored research remains AFIT's primary focus.

Dr. Won B. Roh, the research committee chairman, offered support throughout all phases of this effort; actually beginning before this particular investigation. His initial advice concerning the research area, course work, and qualifying examinations was crucial to the successful completion of the research and the degree program.

Major Glen P. Perram was the heart and soul of this research; his interest and expert knowledge in chemical kinetics and lasers is second to none. Major Perram provided the vector corrections necessary for a sustained research effort. *Thank you* does not seem like words enough to express the author's feelings of gratitude.

The author offers thanks to the laboratory, secretarial, and support staff also critical to laboratory research. The laboratory technicians Jim Reynolds and Greg Smith provided the day-to-day technical knowledge required to keep the research equipment working and the supplies needed to perform the experiments.

Mike Ray at the Wright Laboratory glass shop kept the research going on several occasions by responding to short-notice tasks which are common to high-vacuum, gas-phase chemical kinetic research. The AFIT fabrication shop also provided several key items used in the experiments.

A special thank you goes to Cliff Wever, whose generous gifts of computer hardware and software made much of the data analysis possible.

Finally, the author thanks his wife, Joan, and their children for their never-ending patience, understanding, and support during this extensive education and research effort.

Ray O. Johnson

Table of Contents

	Page
Preface.....	iii
Table of Contents.....	v
List of Figures.....	ix
List of Tables.....	xiii
Abstract.....	xiv
I. Introduction	1
A. Overview.....	2
B. Problem Statement	5
C. Presentation	6
II. Background Theory	7
A. Introduction.....	7
B. Spectroscopic Theory	7
1. Bromine Molecular Theory.....	7
2. Bromine Photolysis.....	14
3. Electronic-to-Vibrational Energy Transfer	20
C. Current Knowledge.....	21
1. Quenching Rate Studies.....	21
a) Quenching Rate Temperature Dependence Studies.....	31
2. Laser Demonstrations	33
III. Atomic Bromine Excitation and Quenching Experiments.....	39
A. Introduction.....	39
B. Theory of Photolysis.....	40
1. Br($^2P_{1/2}$) Excitation and Quenching Kinetics	40

2. Steady-State Analysis	42
3. Pulsed Lifetime Analysis.....	46
4. Effect of Diffusion and Three Body Recombination	47
C. Experiment.....	52
1. Steady-State Experiment Equipment	52
a) Gas Handling System	52
b) Argon-Ion Laser.....	56
c) Absorption Diagnostic System.....	57
d) Detection and Data Collection	59
2. Pulsed-Experiment Equipment	63
3. Cell Pressure-Change Measurement Equipment	65
D. Results.....	67
1. Bromine Absorption Data	67
2. Pulsed Lifetime Studies	68
3. Steady-State Photolysis Studies	72
4. Quenching Rate Temperature Dependence	78
5. Diffusion, Pressure Change, and Concentration Measurements	85
a) Diffusion Measurements.....	85
b) Pressure Change Measurements.....	87
c) Atomic and Molecular Bromine Concentration Measurements.....	97
E. Discussion.....	100
1. Overview	100
2. Data Correlation.....	102
F. Conclusion	106

IV. Laser Prototype Demonstration.....	107
A. Introduction.....	107
B. Background Theory.....	107
1. Candidate Laser Species Analysis.....	107
2. Laser Physics	111
C. Experiment.....	117
D. Results	120
1. Br* Laser.....	120
2. CO ₂ Laser.....	124
3. NO Laser	127
E. Discussion.....	131
F. Conclusion	135
V. Conclusions and Recommendations.....	137
A. Conclusions	137
1. Summary of Bromine Quenching Rate Studies	137
2. Summary of Laser Prototype Demonstration.....	138
B. Recommendations	139
1. Electronic-to-Vibrational Energy Transfer Laser Development and Analysis	139
2. Steady-State Bromine Studies.....	140
VI. Bibliography	141
Appendix A: Photolysis Experiment System Operation and Procedures.....	145
A. Argon Ion Laser and Detector Alignment.....	145
B. Pulsed Laser Alignment and Oscilloscope Signal Averaging	146
C. Gas Handling	147
D. Data Collection.....	148

Appendix B: Bromine Distillation and Purification.....	149
Appendix C: Bromine Laser Cavity and Detector Alignment	152
Appendix D: E→V Energy Transfer Theoretical Mechanisms	155
A. Quantum Mechanical Calculations.....	155
B. Long-Range Attractive Forces	156
C. Curve Crossing Mechanisms	157
Appendix E: Error Analysis	159
Appendix F: Buffer Gas Purity	162
Vita	163

List of Figures

Figure	Page
2.1 Bromine Atom Energy Level Diagram	8
2.2 Ground State Diatomic Halogen Molecular Orbital Diagram.....	10
2.3 Diatomic Halogen Correlation Diagram.....	12
2.4 Br ₂ Potential Energy Diagram.....	13
2.5 Br ₂ Absorption Coefficients.....	15
2.6 Molecular Bromine Absorption Spectrum and Potential Energy Curves	17
2.7 Quantum Yields of Br(² P _{1/2}) Production from Br ₂ Photolysis.....	18
2.8 IBr Potential Energy Diagram.....	19
2.9 Partial Energy-Level Diagram of Br*–CO ₂ System.....	35
3.1 Predicted Br* Emission Intensity versus Molecular Bromine Concentration	44
3.2 Schematic Diagram of the Steady-State Photolysis Experimental Apparatus	53
3.3 Absorption Measurement System.....	57
3.4 Br* Detection System	60
3.5 Broadband 2.71 μm Filter Transmission Characteristics.....	61
3.6 Schematic Diagram of the Pulsed Photolysis Experimental Apparatus	64
3.7 Br* Pulsed Fluorescence Lifetime Data	65
3.8 Differential Amplifier Circuit	66
3.9 Molecular Bromine Absorption Data.....	68
3.10 Carbon Dioxide Quenching of Br* Stern-Volmer Plot	70

3.11 Bromine Pulsed Self-Quenching Stern-Volmer Plot.....	71
3.12 Br* Fluorescence Intensity versus Molecular Bromine Pressure	74
3.13 Bromine Steady-State Self-Quenching Stern-Volmer Plot.....	75
3.14 CF ₄ -Br* Steady-State Quenching Data	76
3.15 Normalized Transmitted 488 nm Laser Intensity for the Temperature Range 300–425 K	78
3.16 Normalized Temperature-Dependent Br ₂ Quenching Cross Section	79
3.17 Normalized Temperature-Dependent CO ₂ Quenching Cross Section	81
3.18 Normalized Temperature-Dependent N ₂ O Quenching Cross Section	82
3.19 Normalized Temperature-Dependent HCl Quenching Cross Section	82
3.20 Normalized Temperature-Dependent COS Quenching Cross Section	83
3.21 Normalized Temperature-Dependent NO Quenching Cross Section	84
3.22 Normalized Temperature-Dependent NO ₂ Quenching Cross Section	84
3.23 Transmitted 488 nm Ar ⁺ Intensity Showing Diffusion Results	86
3.24 Change in Cell Pressure for 10 Torr of Argon Added to 2 Torr of Molecular Bromine	89
3.25 Change in Cell Pressure for 100 Torr of Argon Added to 2 Torr of Molecular Bromine	90

3.26 Change in Atomic Bromine Concentration for Three Laser Powers and Small Radius Cell.....	94
3.27 Change in Atomic Bromine Concentration for Large Radius Cell	95
3.28 Change in Atomic Bromine Concentration Calculated from Absorbed Power	96
3.29 Curve Fit to Change in Atomic Bromine Concentration Calculated from Absorbed Power.....	97
3.30 On-axis Ar ⁺ Transmitted Laser Power.....	98
3.31 Percent of Atomic Bromine for Two Laser Powers Calculated from Absorbed Power	99
3.32 Buffer Gas Quenching Rate versus Energy Defect for 13 Molecules.....	103
4.1 NO Rotational Line Distribution as a Function of <i>J</i>	116
4.2 Schematic Diagram of the Laser Demonstration Apparatus	118
4.3 Family of Br* Laser Pulse Shapes for Varying Pump Energy	121
4.4 Normalized Br* Laser Energy as a Function of Pump Energy	122
4.5 Family of Br* Laser Pulse Shapes for Varying IBr Pressure.....	123
4.6 Normalized Br* Laser Pulse Energy as a Function of IBr Pressure.....	123
4.7 Family of CO ₂ Laser Pulse Shapes for Varying Pump Energy	124
4.8 Normalized CO ₂ Laser Energy as a Function of Pump Energy	125
4.9 Family of CO ₂ Laser Pulse Shapes for Varying CO ₂ Pressure	126
4.10 Normalized CO ₂ Laser Pulse Energy as a Function of CO ₂ Pressure	127
4.11 Family of NO Laser Pulse Shapes for Varying Pump Energy	128
4.12 Normalized NO Laser Energy as a Function of Pump Energy	129
4.13 Family of NO Laser Pulse Shapes for Varying NO Pressure.....	130

4.14	Normalized NO Laser Energy as a Function of NO Pressure	130
4.15	Temporal Profile of CO ₂ and NO Laser Pulses	131
4.16	Modeled Temporal Plot of the NO Laser Intensity	134
B.1	Bromine Distillation and Purification Schematic Diagram	149
C.1	Laser Demonstration Apparatus	153

List of Tables

Table	Page
2.1 Molecular Bromine Spectroscopic Constants	14
2.2 Br($^2P_{1/2}$) Spin-Orbit Relaxation Rate Coefficients	23
3.1 Carbon Dioxide Pulsed Quenching Rate Coefficients.....	70
3.2 Br ₂ Pulsed Self-Quenching Rate Coefficients	72
3.3 Steady-State Experimental Rate Coefficients.....	77
4.1 List of Infrared Lasing Molecules	109
4.2 Candidate Laser Acceptor Molecules.....	110
F.1 Table of Buffer Gases, Manufacturer, and Purity	162

Abstract

Pulsed and steady-state photolysis experiments have been conducted to determine the rate coefficients for collisional deactivation of the spin-orbit excited state of atomic bromine, $\text{Br}(^2\text{P}_{1/2})$. Pulsed lifetime studies for quenching by Br_2 and CO_2 established absolute rate coefficients at room temperature of $k_{\text{Br}_2} = 1.2 \pm 0.1 \times 10^{-12}$ and $k_{\text{CO}_2} = 1.5 \pm 0.2 \times 10^{-11}$ $\text{cm}^3/\text{molecule-s}$. Steady-state photolysis methods were used to determine the quenching rates for the rare gases, N_2 , O_2 , H_2 , D_2 , NO , NO_2 , N_2O , SF_6 , CF_4 , CH_4 , CO , CO_2 , COS , SO_2 , H_2S , HBr , HCl , and HI relative to that for Br_2 . Quenching rate temperature dependence was examined for Br_2 , CO_2 , N_2O , HCl , COS , NO , and NO_2 for temperatures from 300 to 420 K. Diffusion and three body effects were examined in order to determine the slowest relative quenching rate measurable by this experimental technique.

Prototype $\text{Br}(^2\text{P}_{1/2} \rightarrow ^2\text{P}_{3/2})$, $\text{CO}_2(101 \rightarrow 100)$, and $\text{NO}(\nu = 2 \rightarrow 1)$ electronic-to-vibrational energy transfer infrared lasers have been demonstrated operating at 2.71, 4.3, and 5.4 μm respectively. Electronic energy from $\text{Br}(^2\text{P}_{1/2})$ bromine atoms photodissociated from iodine monobromide (IBr) using frequency-doubled 532 nm pulses from a Nd:YAG laser are transferred to vibrational energy in the acceptor molecular species. Temporal pulse profiles were obtained as a function of IBr and laser species gas pressures and YAG laser energy, and analysis was performed to determine laser gain, pump energy threshold, and operational feasibility.

EXCITED ATOMIC BROMINE

ENERGY TRANSFER AND QUENCHING MECHANISMS

I. Introduction

In this experimental research, pulsed and steady-state photolysis techniques are used to photodissociate molecular bromine, Br_2 , into atomic spin-orbit split states $\text{Br}(^2\text{P}_{3/2})$ and $\text{Br}(^2\text{P}_{1/2})$. The $\text{Br}(^2\text{P}_{1/2})$ electronically-excited state, subsequently called Br^* , is 0.456 electron-volts (eV) or 3685 cm^{-1} above the $\text{Br}(^2\text{P}_{3/2})$ ground state. Pulsed laser photolysis and subsequent Br^* lifetime measurements are used to determine absolute Br^* self-quenching rates; that is the Br_2 quenching rate on Br^* . Pulsed laser experiments are also used to verify the well-known CO_2 on Br^* quenching rate. Then steady-state photolysis is used to determine the quenching rate of a set of quenching gases relative to the now well-determined Br_2 self-quenching rate. Quenching rate temperature dependence and energy considerations are used to determine possible electronic-to-vibrational energy transfer mechanisms. Additionally, atomic and molecular stimulated emission and lasing are observed from prototype Br^* , and CO_2 and NO molecular energy transfer lasers. Analysis is performed to determine laser gain and threshold characteristics.

The following section describes the motivation for this research and its relevance to the Air Force. The next section of the introduction presents the problem statement, and the final section presents an outline of the dissertation.

A. Overview

The spin-orbit properties of the halogen atoms Br and I make them interesting for study. The relatively large spin-orbit separations of Br and I of 3685 and 7603 cm^{-1} , respectively, make it possible that energy transferred to an acceptor molecule might populate vibrational levels higher than the first, even for relatively high-frequency vibrations. This fact makes it conceivable that population inversion and lasing by the acceptor species can take place after this energy transfer. Most molecules quench I^* about ten times more slowly than they quench Br^* ; a property which possibly makes the energy transfer process more observable in Br^* transfer lasers.

The collisional deactivation of $\text{Br}(^2\text{P}_{1/2})$ has been studied extensively,¹⁻⁵ in part due to the interest in developing mid-infrared lasers.⁶⁻⁷ The Br^* quenching is particularly rapid for near resonant electronic-to-vibrational ($\text{E} \rightarrow \text{V}$) energy transfer,⁸⁻⁹ a field which has received much interest in laboratories around the world. Atomic bromine lasers or energy transfer lasers have received renewed attention¹⁰ due to the desire to develop an efficient, moderate-power 3-5 μm laser for tactical military applications.

This research seeks to extend the kinetic data base for quenching of Br^* by various collision partners using pulsed and steady-state photolysis techniques and demonstrate prototype $\text{E} \rightarrow \text{V}$ energy transfer lasers. Photolysis of Br_2 near $\lambda = 400 \text{ nm}$ produces nearly equal proportions of $\text{Br}(^2\text{P}_{1/2})$ and $\text{Br}(^2\text{P}_{3/2})$ via the repulsive limb of the $\text{B}^3\Pi(0^+)$ state. The resulting weak $\text{Br}(^2\text{P}_{1/2} - ^2\text{P}_{3/2})$ fluorescence at 2.71 μm is monitored as a function of buffer gas pressure to determine quenching rate coefficients.

An Air Force requirement exists to develop kilowatt-class infrared (IR) lasers operating in the 3 to 5 μm region of the spectrum for electro-optic countermeasures. These lasers would be mounted as internal or external aircraft pods. A candidate laser must be energy efficient so as not to take excessive energy from the aircraft's limited available power. Additionally, the laser should have wavelength agility to respond to various threats and thus making counter-countermeasures more difficult. The laser should have good beam quality so beam divergence does not increase the laser's power requirements. Finally, the laser must be able to function in a high-vibration, operational environment which could lead to cavity stability problems.

Possible laser candidates are photolytically and optically pumped lasers, and in the long term, new semiconductor lasers operating at the desired infrared wavelengths. Although semiconductor lasers have been demonstrated, they do not yet have the power necessary for this application nor do they operate at the required infrared wavelengths. The candidate laser could also use direct photolysis or photolysis and subsequent $E \rightarrow V$ energy transfer to molecular candidates.

An advantage of photolysis versus optical pumping is a less stringent requirement on the wavelength stability of the dissociating source. In optically-pumped laser systems, the pump source directly accesses atomic and molecular ro-vibrational levels, therefore, the source must be very stable to access particular ro-vibrational levels. In the photolysis method, the dissociating laser source can vary over a relatively broad wavelength range as long as the energy lies within the candidate's absorption continuum. For this reason, photodissociation requires less source-wavelength stability; an important concern in an aircraft's operational environment. Other

advantages of photolysis are closed-cycle operation and easier thermal control compared to semiconductor lasers.

In the direct photolysis method, a simple molecule like a diatomic, or a more complex polyatomic molecule is photodissociated by a light source into ground state and at least one excited-state atom. These excited atoms then become the lasing species. A potential drawback with this direct photolysis method is the lack of laser wavelength tunability since the photolysis produces an atomic species.

In the $E \rightarrow V$ energy transfer process, the excited atoms transfer energy to ro-vibrational modes of an appropriate molecular laser species. This collisional quenching of electronically excited atoms and molecules, with resulting excitation of molecular vibrations is under study in a number of laboratories.⁷

In the $E \rightarrow V$ transfer method, the laser could use frequency conversion of a compact, high power, diode-pumped Nd:YAG laser. The YAG laser frequency is doubled, and this 532 nm energy becomes the appropriate source for photodissociating halogen molecules to form the electronically-excited and ground-state halogen atoms. A disadvantage of this method is the new quantum efficiency, or the ratio of the pumping to lasing wavelengths. Efficiency is reduced when converting 1.06 μm photons to 532 nm photons in the doubling process and then back to infrared photons during the subsequent emission.

A possible realization of this laser is to use $E \rightarrow V$ energy transfer from gas-phase, electronically-excited bromine atoms to the ro-vibrational modes of a suitable molecular laser species. Such a laser would be discretely tunable over a finite bandwidth, defeating simple filter counter-

countermeasures. This tunability is achieved by accessing various rotational levels in the receptor molecule by means of intra-cavity tuning. Electronic-to-vibrational energy transfer from electronically-excited bromine atoms, Br* to CO₂ molecules has been observed to produce stimulated CO₂ emission at 4.3, 10.6, and 14.1 μm .⁶ This energy transfer process has also resulted in stimulated emission from HCN at 3.85, 7.25, and 8.48 μm , from C₂H₂ in the 7–8 μm region, and H₂O and N₂O at their respective laser frequencies.⁶ Recently, Pastel and others published research results supporting an efficient Br* laser which they feel can be operated in a closed-cycle configuration; an important operational advantage.¹⁰

Considerable research has been performed investigating I* energy transfer mechanisms, primarily due to the Chemical Oxygen Iodine Laser (COIL); less work has been done for Br*. This dissertation research expands the Br* E \rightarrow V energy transfer database. This database is needed to assess the potential of the proposed infrared laser.

B. Problem Statement

Evaluation of the potential of using excited bromine as a gas-phase, chemical-laser electronic-to-vibrational energy transfer agent requires understanding two distinct sets of issues. This first set involves exciting the bromine atom to the ²P_{1/2} state and efficiently transferring the atom's electronic energy to a laser candidate's ro-vibrational levels. Enough energy must be transferred to the acceptor species to support lasing, without much loss through undesired collisional and radiative mechanisms. The second set

is the acceptor species' lasing characteristics. This dissertation research provides some answers to these questions in two experimental phases.

In the first phase, discussed in Chapter III, the excitation and quenching of atomic bromine is examined via pulsed photolysis techniques which determine the absolute Br^* deactivation rates. Steady-state photolysis techniques are also used to obtain Br^* quenching rates for selected molecular species. The buffer gas quenching rate coefficients are determined relative to the now well-determined Br_2 self-quenching rate. Additional studies are performed to determine the various contributors to the observed Br^* quenching rate. Finally, temperature studies are performed to help determine which of several $\text{E} \rightarrow \text{V}$ energy transfer mechanisms is responsible for the energy transfer.

In the second phase, discussed in Chapter IV, the demonstration of molecular transfer lasers based on Br^* , CO_2 , and NO is presented. Analysis is performed to address the lasers' characteristics and efficiency.

C. Presentation

Chapter II reviews the kinetic and spectroscopic theory of atomic and molecular bromine which is common to both experimental sections. Chapter III discusses the current knowledge, theory, experimental procedure, and results from the bromine photolysis and quenching research. Chapter IV provides similar information for the laser demonstration experiments. Chapter V provides the overall research conclusions and makes recommendations for future work.

II. Background Theory

A. Introduction

This chapter presents atomic and molecular bromine spectroscopic theory, photolysis theory, and a summary of current knowledge pertinent to this dissertation research. The spectroscopy section discusses bromine atomic and molecular theory, including a brief description of the bromine molecular states. The section on photolysis gives an overview of how laser photolysis yields the desired electronically excited and ground state bromine atoms. Finally, the current knowledge section describes some of the more important excited bromine quenching work performed, lists known bromine quenching rate coefficients, and discusses previous laser experiments that used $E \rightarrow V$ energy transfer from Br^* .

B. Spectroscopic Theory

1. Bromine Molecular Theory

Bromine (Br), a group VIIA element, is a halogen. Bromine has a melting point of -7 degrees C, a boiling point of 59 degrees C, and forms a diatomic molecule (Br_2) in its elemental molecular state.¹¹ The bromine ground electronic configuration is $4p^5$ neglecting filled sublevels, which is one electron short of filling the p sublevel. This configuration results in spin-orbit split term symbols $\text{Br}(^2P_{3/2})$ and $\text{Br}(^2P_{1/2})$, with $\text{Br}(^2P_{3/2})$ having the lower energy following Hund's energy ordering rules.¹² This separation in

spin-orbit split states is called the fine structure, and the $\text{Br}(^2\text{P}_{1/2})$ electronically excited state is 0.456 electron-volts (eV) or 3685 cm^{-1} above the $\text{Br}(^2\text{P}_{3/2})$ ground state. The various values of total angular momentum, including nuclear spin, result in six hyperfine energy levels. The hyperfine line spectrum is 0.5 cm^{-1} or 15 GHz wide, consisting of two groups with three spectral lines each. There are two naturally-occurring bromine isotopes of nearly equal abundance (^{79}Br : 0.505, ^{81}Br : 0.495). The hyperfine energy separations vary with bromine isotope, but are on the order of 0.35 cm^{-1} for the $\text{Br}(^2\text{P}_{1/2})$ energy level and 0.07 cm^{-1} for the $\text{Br}(^2\text{P}_{3/2})$ energy level.¹³ The bromine fine structure and hyperfine structure energy levels are shown in Figure 2.1.

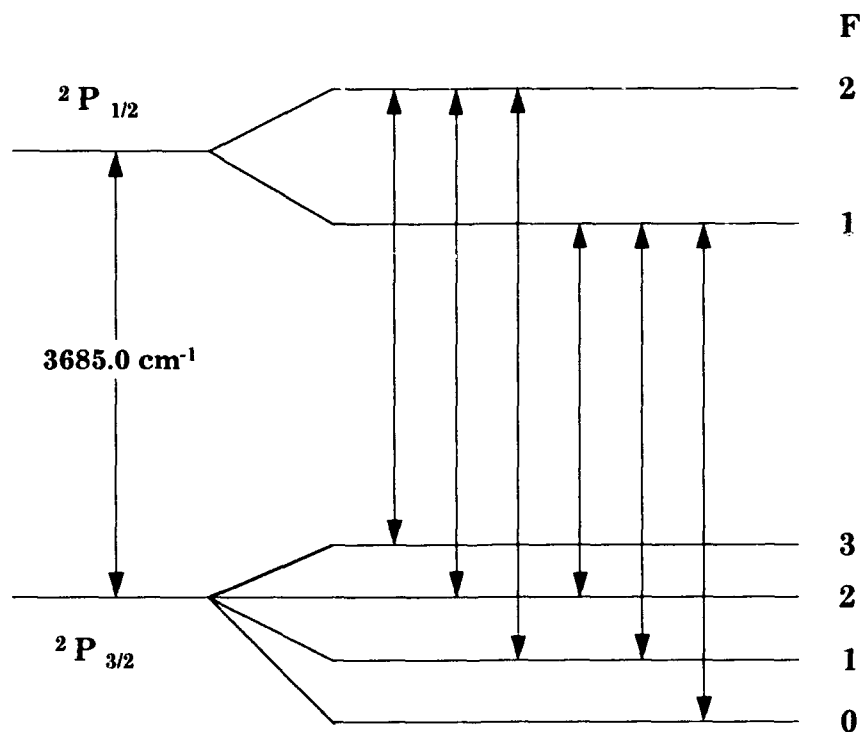


Figure 2.1. Bromine atom energy level diagram showing the spin-orbit split fine and hyperfine energy levels (not shown to scale). The arrows indicate allowed transitions between hyperfine states.

This figure depicts the energy difference between the fine structure states and the allowed transitions between the hyperfine states, $\Delta F = 0, \pm 1$.¹³ This energy difference between the $^2P_{1/2}$ and the $^2P_{3/2}$ corresponds to a transition wavelength of 2.71 μm .

The spontaneous emission probability, Einstein A coefficient, for the $^2P_{1/2} \rightarrow ^2P_{3/2}$ transition is 0.898 sec^{-1} .¹³ This coefficient corresponds to a bromine radiative lifetime of 1.12 seconds. This metastable radiative lifetime is long because the electric dipole transition for the $^2P_{1/2} \rightarrow ^2P_{3/2}$ transition is strongly forbidden, $\Delta L \neq 0$ for a single electron transition.¹⁴ The fluorescence is weak, but infrared emission-detection techniques can be used to monitor the $\text{Br}(^2P_{1/2})$ concentration.^{15, 16} In this experiment, the hyperfine structures of the $^2P_{1/2} \rightarrow ^2P_{3/2}$ transition are not resolved because of the 2.71 μm filter bandwidth of approximately 0.01 μm or 13.6 cm^{-1} . The 300 K Doppler width is approximately $5.1 \times 10^{-3} \text{ cm}^{-1}$ or 150 MHz. The shift for individual hyperfine transitions due to the two bromine isotopes is comparable to the Doppler width.¹³

When two *p*-orbital atoms are brought together, as in the formation of Br_2 , one method of determining the molecular orbital configurations is the MO-LCAO or Molecular Orbital-Linear Combination of Atomic Orbitals approximation.¹² This model predicts that atoms with partially-filled *p*-orbitals will form σ_g , π_u , π_g , and σ_u molecular orbitals.¹⁷ The ground state electronic configuration $(\sigma_g)^2(\pi_u)^4(\pi_g)^4(\sigma_u)^0$ denoted 2440, yields the term symbol $X \ ^1\Sigma_g^+$, and is shown in Figure 2.2. Excited electronic molecular configurations are formed by promoting electrons to higher energy levels, such as the 2431, 2341, and 2422 configurations.

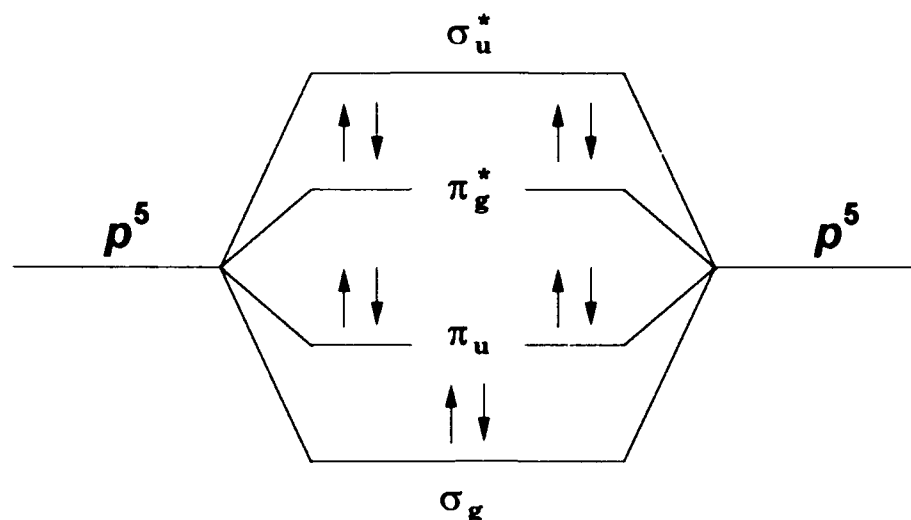


Figure 2.2. Ground state diatomic halogen molecular orbital diagram showing the resulting molecular orbital configuration when combining two partially-filled p -orbital atoms.

Hund's coupling cases (a) and (c) are applicable for diatomic halogens, and are used to model angular momentum coupling. In case (a), the total electron spin and orbital angular momenta are weakly coupled to each other, but are strongly coupled to the internuclear axis. In this case, analogous to the Russell-Saunders coupling model for atoms, the total electronic orbital angular momentum $\Lambda = \sum_i \lambda_i$, the total electronic spin angular momentum $S = \sum_i s_i$, and the total axial angular momentum $\Omega = \Lambda + \Sigma$, where Σ is the z -component of S . The total angular momentum, J , is found from coupling Ω to the molecular angular momentum, N , which is perpendicular to the internuclear axis. J can take on values of $\Omega + N$, where N is a non-negative integer. This coupling case results in $^1\Sigma$, $^{1,3}\Pi_u$, and $^{1,3}\Pi_g$ term symbols for the 2440, 2431, and 2341 configurations, respectively. Although considered as weak, the spin-orbit interaction further splits the triplet $^3\Pi$ state into the

$^3\Pi(0)$, $^3\Pi(1)$, and $^3\Pi(2)$ states depending on their total angular momentum. The $\Omega = 0$ state is further split due to reflection symmetry. When combined, these interactions yield states $^3\Pi_{u,g}(2, 1, 0^+, 0^-)$, $^1\Pi_{u,g}(1)$, and $^1\Sigma(0^+)$.

In Hund's case (c), the spin-orbit interaction cannot be uncoupled, therefore Ω is the only good quantum number. Mulliken developed a series of coupling rules for coupling homonuclear diatomic molecules.¹⁷ For the case of bromine, a diatomic halogen, the addition of two $^2P_{3/2}$ states yield $(3_u, 2_u, 2_g, 1_u, 1_u, 1_g, 0_u^-, 0_u^-, 0_g^+, 0_g^+)$ states, and adding a $^2P_{3/2}$ and a $^2P_{1/2}$ state yield $(2_u, 2_g, 1_u, 1_u, 1_g, 1_g, 0_u^+, 0_u^-, 0_g^+, 0_g^-)$ states.

Actual molecules neither follow Hund's case (a) or (c) completely. The cases are actually two limits that blend smoothly from one to the other depending on the atoms being modeled. The connection between the two limiting approximate cases is known as a correlation diagram. A diatomic halogen correlation diagram is shown in Figure 2.3. For the halogens and interhalogens, atomic spin-orbit coupling is still partially effective at typical equilibrium bond lengths. Hund's case (c) gives the best description of this coupling at intermediate and large internuclear distances.¹⁷ The absence of Q -branch transitions in the interhalogens, which are allowed only in case (a), also indicates a tendency toward case (c).

Other than the ground state, the most deeply bound states correlate to the $2431\ ^3\Pi_u$ configuration and are denoted by the term symbols B $^3\Pi(0_u^+)$, A $^3\Pi(1_u)$, and A $^3\Pi(2_u)$.¹⁸

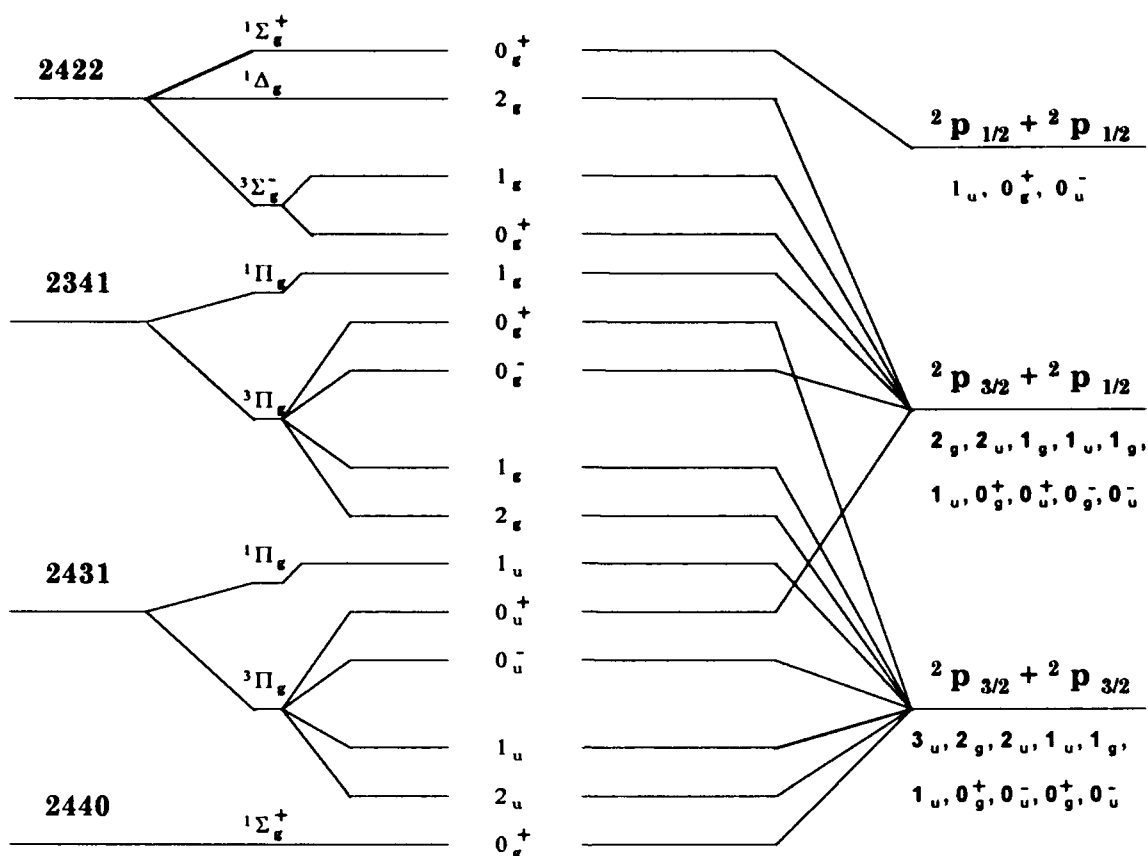


Figure 2.3. Diatomic halogen correlation diagram showing the connection between Hund's cases (a) and (c).

Figure 2.4 shows a molecular bromine potential energy diagram. The ordinate is energy in eV, and the abscissa is the internuclear distance between the nuclei in angstroms (\AA). The bound molecular states are shown by solid lines, and the unbound or repulsive states are represented by dashed lines. Clearly shown are the bound X $1\Sigma_g^+$ ground state, and the A $3\Pi(1_u)$ and B $3\Pi(0_u^+)$ excited states. Also shown is the repulsive $1\Pi(1_u)$ state. Not shown in Figure 2.4 are the vibrational and rotational levels within each electronic energy level.

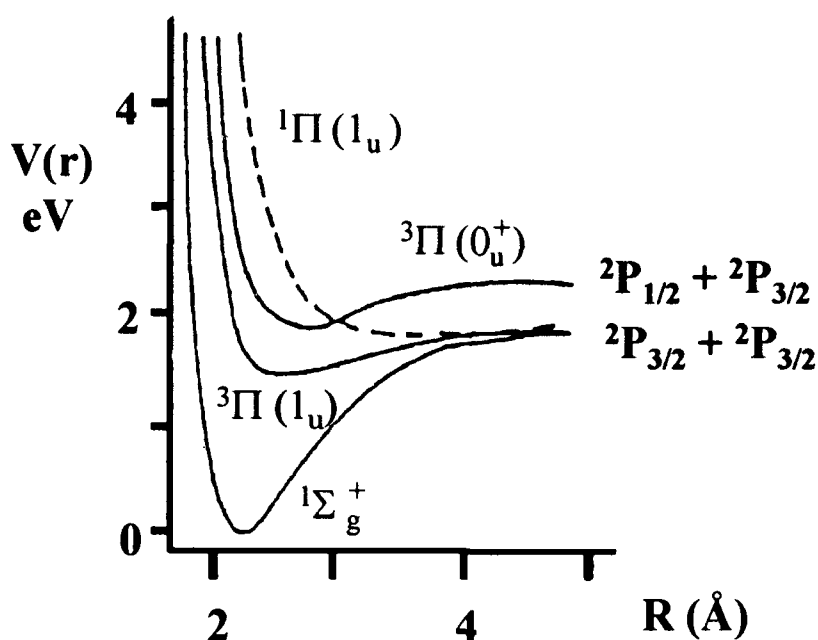


Figure 2.4. Br_2 potential energy diagram showing the bound $X\ ^1\Sigma_g^+$ ground state, and the $A\ ^3\Pi(1_u)$ and $B\ ^3\Pi(0_u^+)$ excited states shown in solid lines and the repulsive $1\Pi(1_u)$ state shown as a dashed line.¹⁵

Figure 2.4 also shows that if adequate energy is absorbed by the bromine molecule, molecular dissociation can occur which results in the formation of either $\text{Br}(^2P_{1/2}) + \text{Br}(^2P_{3/2})$ atoms or $\text{Br}(^2P_{3/2}) + \text{Br}(^2P_{3/2})$ atoms. Table 2.1 below lists vibrational and rotational constants for bromine X, A, and B electronic states. The next section discusses molecular bromine photodissociation, or one method of producing excited bromine atoms.

Table 2.1

Molecular Bromine Spectroscopic Constants ^{19, 20}

STATE	T_e (cm ⁻¹)	ω_e (cm ⁻¹)	$\omega_e x_e$ (cm ⁻¹)	B_e (cm ⁻¹)	α_e (cm ⁻¹)	r_e (Å)
B $^3\Pi(0_u^+)$	15902.47	166.57	1.616	0.0589	0.0004801	2.678
A $^3\Pi(1_u)$	13814	170.7	3.69			
X $^1\Sigma_g^+$	0	323.31	1.06	0.0811	0.0003129	2.281

2. *Bromine Photolysis*

Photochemical reactions are sometimes initiated when a molecule or atom absorbs a quantum of light. The incident light induces a transition from the ground state to a quantized rotational and vibrational level within an excited electronic level or to a repulsive electronic state.¹⁵

Photodissociation can occur when the molecule is raised to an excited state that has more than enough energy to break the weakest molecular bond. This dissociation energy ranges from about 1 eV in O₃ to more than 11 eV for CO. These energies correspond to light from below 1130 to around 12,400 Å. Absorbed microwave and infrared radiation may cause changes in rotational and vibrational energies, but usually does not cause single-step dissociation.¹⁵

Figure 2.5 graphically depicts the Br₂ absorption coefficients for wavelengths from 2000 to 6000 Å. The absorption coefficient, ϵ , is in units of liter mol⁻¹ cm⁻¹, base 10 at room temperature. The $^1\Pi(1_u)$, A $^3\Pi(1_u)$, and

$B^3\Pi(0_u^+)$ electronic states of Br_2 are involved in the absorption and the eventual Br^* excitation process.

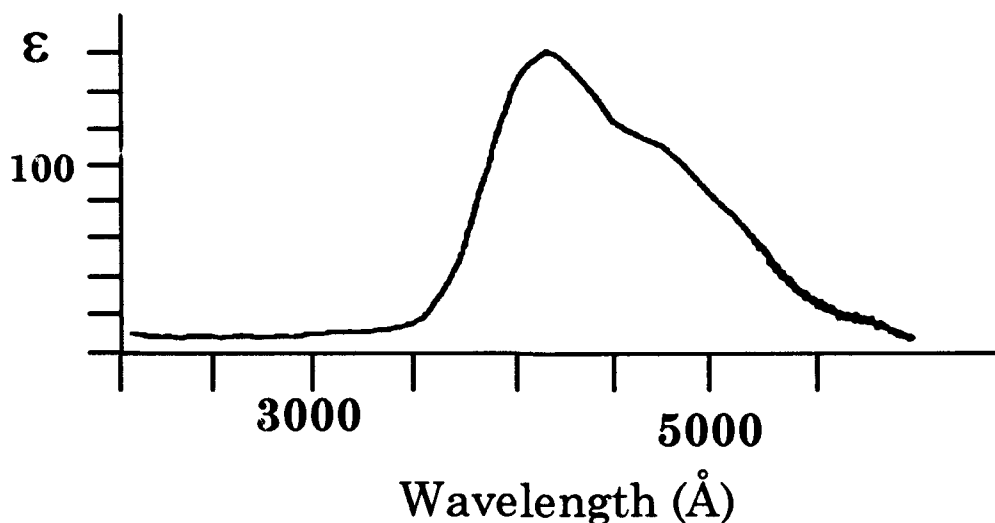
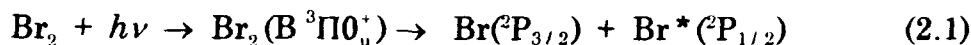


Figure 2.5. Br_2 absorption coefficients as a function of incident light wavelength in angstroms.¹⁵

The absorption spectrum shown in Figure 2.5 shows a discrete or banded structure from about 5110 to 6000 Å, followed by a continuum from 2000 to 5110 Å. The discrete structure results from incident radiation accessing resonant transitions between vibrational levels within the $X^1\Sigma_g^+$ and $B^3\Pi(0_u^+)$ electronic states.

For wavelengths between 4300 and 5106 Å, the repulsive limb of the $B^3\Pi(0_u^+)$ state is accessed which results in nearly equal proportions of $Br(^2P_{3/2})$ and $Br(^2P_{1/2})$ atoms being formed. It is this unique correlation between the $B^3\Pi(0_u^+)$ electronic state of molecular bromine with the $Br(^2P_{1/2})$ atom that results in the formation of the excited bromine atom.

Equation (2.1) shows the two-step process of first accessing the bromine $B^3\Pi(0_u^+)$ state and then forming the excited and ground state bromine atoms for incident wavelengths, $5106 > \lambda > 4300 \text{ \AA}$:



If the incident wavelength is less than approximately 4300 \AA , only the $^1\Pi(1_u)$ unbound state is accessed, which results in the formation of two ground state atoms. For wavelengths above 6300 \AA , the incident photon does not have sufficient energy to break the bond of bromine molecules in the lowest vibrational and rotational levels in the ground state.

Photodissociation for incident wavelengths above 6300 \AA can occur only if the light-absorbing molecules are originally in high vibrational and rotational levels in the ground state.

Figure 2.6 shows the connection between the bromine potential energy curves and the absorption coefficients associated with the visible absorption spectrum of Br_2 . The bromine absorption curve is actually composed of two constituent curves which represent incident radiation accessing the desired $B^3\Pi(0_u^+)$ state and the unbound $^1\Pi(1_u)$ state. Access to the $B^3\Pi(0_u^+)$ state occurs for incident wavelengths from 4300 and 5106 \AA as shown above, which results in the lower dotted peak in the absorption curve. The upper dotted peak results from accessing the $^1\Pi(1_u)$ state, and actually begins at incident wavelengths less than 4880 \AA . The total bromine absorption curve represents a blending of state transitions rather than a sharp transition from one electronic state to another.

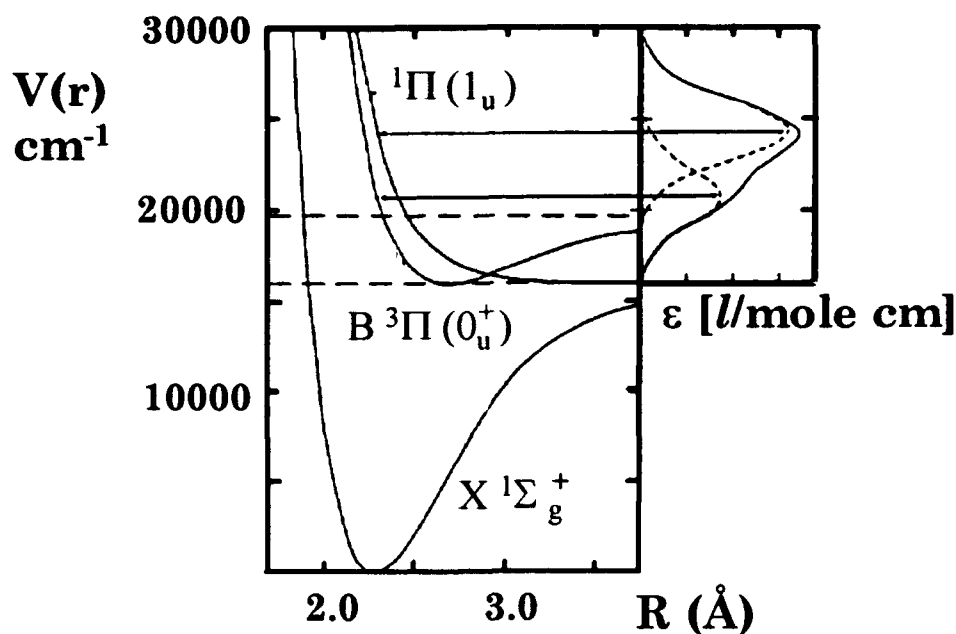


Figure 2.6. Molecular bromine absorption spectrum and potential energy curves.²¹

Molecular bromine excited to the $A\ ^3\Pi(1_u)$ state may dissociate to two ground state $\text{Br}(^2P_{3/2})$ atoms directly, and crossing to the $B\ ^3\Pi(0_u^+)$ or $^1\Pi(1_u)$ electronic states appears to not be significant.²² Br_2 excited to the $B\ ^3\Pi(0_u^+)$ cannot cross to the $A\ ^3\Pi(1_u)$ state but can cross to the $^1\Pi(1_u)$ where it again dissociates into two $\text{Br}(^2P_{3/2})$ atoms. It is also possible, but not likely, for Br_2 excited to the $^1\Pi(1_u)$ state to cross to the $B\ ^3\Pi(0_u^+)$ state and dissociate into one $\text{Br}(^2P_{3/2})$ and one $\text{Br}(^2P_{1/2})$ atom.²²

Haugen and others used a two-laser, pulse-and-probe technique to study Br_2 photofragmentation over the wavelength range 450–530 nm.²³ They found the peak quantum yield for Br_2 photofragmentation to be 87 percent at 500 nm and a quantum yield of approximately 84 percent at 488 nm. Figure 2.7 shows the Br^* quantum yield as a function of incident

laser wavelength. These percentages are of the maximum possible number of Br^* atoms produced, which for this reaction is one Br^* atom (and one ground state atom) for every incident photon. As previously stated, not every incident photon accesses the $\text{B } ^3\Pi(0_v^-)$ state and results in the creation of a Br^* atom.

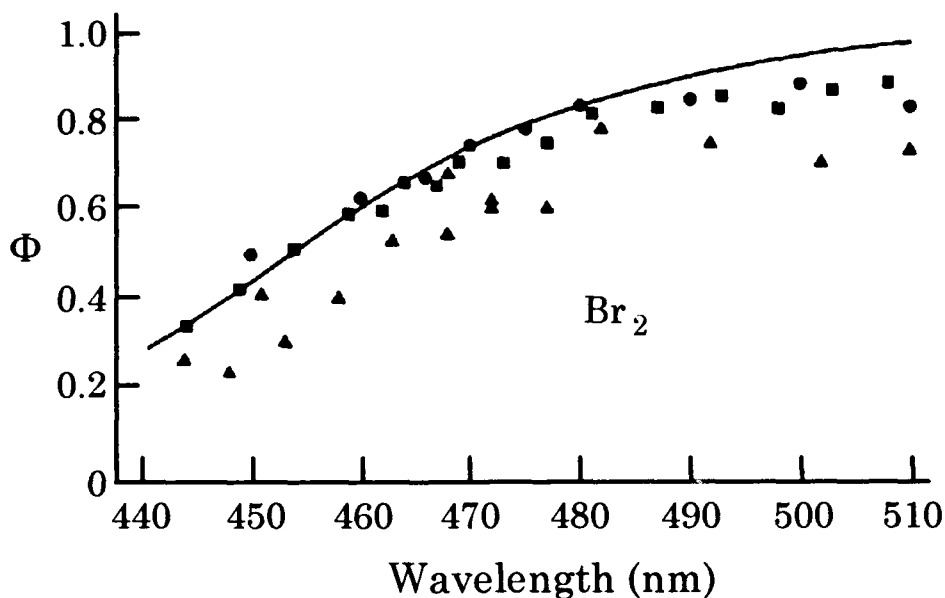


Figure 2.7. Quantum yields of $\text{Br}(^2\text{P}_{1/2})$ production from Br_2 photolysis as a function of wavelength where ●, ■, and ▲ are experimental data, and the solid curve represents a theoretical calculation.²³

Smedley and others precisely measured Br^* quantum yields from 510–550 nm. These researchers found the Br^* yields varied from 85 percent at 510 nm to 12 percent at 550 nm.²⁴ These results make it necessary to use another precursor to Br^* besides molecular bromine at dissociating laser wavelengths above 515 nm.

Since the laser available for the $\text{E} \rightarrow \text{V}$ energy transfer laser experiment operates at 532 nm, iodine monobromide (IBr) is used in place of

Br₂ as the precursor for Br*. A frequency-doubled Nd:YAG laser operating at 532 nm is used to photodissociate IBr. The IBr quantum yield at 532 nm is approximately 68 percent.^{22, 23} An IBr potential energy diagram is shown in Figure 2.8. IBr is primarily photodissociated into the B ³Π(0⁺) state, which can undergo diabatic dissociation into I(²P_{3/2}) + Br(²P_{1/2}) or dissociate adiabatically to form I(²P_{3/2}) + Br(²P_{3/2}). The diabatic channel dominates, and creates a population inversion between Br* and Br. IBr selectively reacts with ground state Br versus Br* to make the inversion more stable.¹⁰

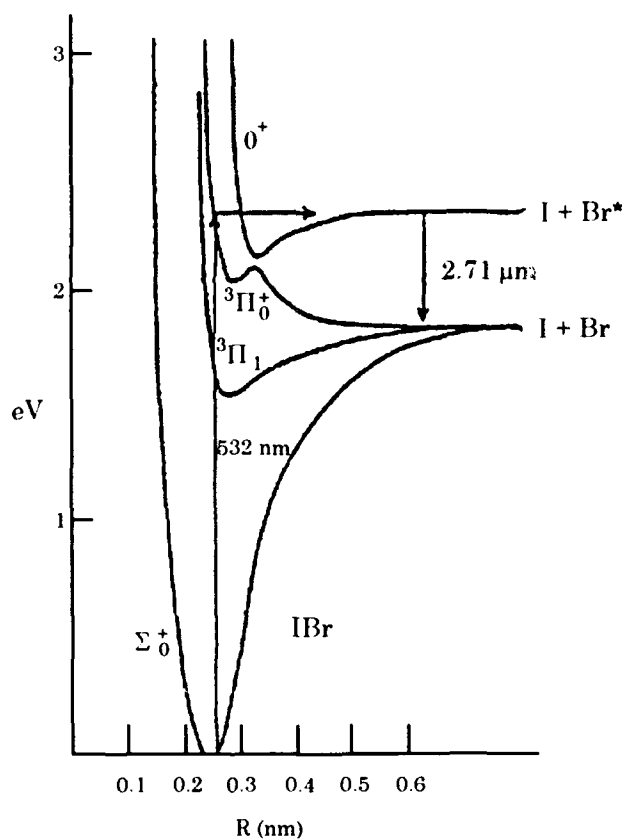


Figure 2.8. IBr potential energy diagram showing the potential curves relevant to the creation of Br*.¹⁰

3. *Electronic-to-Vibrational Energy Transfer*

Understanding electronic-to-vibrational energy transfer is necessary for the design and development of laser systems employing this excitation scheme. A theoretical model of the $E \rightarrow V$ energy transfer aids in the prediction of the direction and efficiency of photochemical reactions.

When considering the transfer of energy from the excited bromine atom to an acceptor molecule, A , the total rate coefficient, k^E , with which molecule A quenches Br^* is desired. If molecule A has only one vibrational mode, the total rate coefficient is the sum of the rate coefficients of the individual vibrational levels in molecule A , that is, $k^E = \sum k_i$ where the summation is from $i = 0$ to $i = v_{\max}$, and k_i is the rate coefficient for the process $Br^* + A(v = 0) \rightarrow Br + A(v = i)$. The maximum vibrational level is determined by conservation of total energy from the bromine atom to molecule A . Although it is desired to obtain the individual values k_i and their temperature dependencies, it is usually only possible to experimentally determine the total quenching rate $k^E = \sum k_i$ and its temperature dependence.

When considering the transfer of energy from Br^* to an acceptor molecule, there are several competing mechanisms taking place. The energy may be transferred to the highest allowed vibrational level and all vibrational levels below it. The energy may be quenched by its molecular precursor, Br_2 . There may also be $V \rightarrow V$, R , T mechanisms by which molecule A may lose its vibrational excitation. Finally, there may be slower radiative decay and wall deactivation effects that depopulate the desired levels. Although these aforementioned competing effects make rate determination difficult, they may also make population inversion and therefore laser operation inefficient or impossible. For these reasons it is

important to have a good understanding of the kinetics pertaining to the desired goal.

The next section provides a summary of the results of the previous photolysis and electronic-to-vibrational energy transfer laser studies.

C. Current Knowledge

1. Quenching Rate Studies

In 1970, Donovan and others made the first direct observation of electronic-to-vibrational energy transfer by the quenching of electronically excited halogen molecules in the $^2P_{1/2}$ state in collisions with molecular species.⁹

Donovan and Husain noted that collisional deactivation of halogen atoms in the $^2P_{1/2}$ state by diatomic molecules is at least two orders of magnitude more efficient than for the noble gas atoms.¹ They went on to note that CO and N₂ both possess expected low quenching rates due to the low electronic energy transfer involving a multivibrational transition in diatomic molecules. They believed that both NO and O₂ had exceptionally high quenching rates possibly due to an inhomogeneous magnetic field present during collision which increases the energy transfer probability. These rate coefficients and the coefficients for other known molecules are listed in Table 2.2, as originally compiled by Tate.²⁵ As noted in the tables, the quenching rate coefficients for many buffer gases vary over several orders of magnitude. More recently measured quenching rate data tend to be more repeatable. One of the goals of this research is to determine a set of Br*

quenching rate coefficients measured by the same experimental technique thereby reducing rate coefficient variation caused by systematic error.

In 1973, Leone and Wodarczyk were the first researchers to make direct measurements of $E \rightarrow V$ energy transfer.⁴ The researchers used 1 mJ pulses of 4730 Å, 500 ns light from a frequency-doubled Nd³⁺:YAG laser to create Br* and Br atoms. Then, by detecting the time-resolved infrared emission from Br*, HCl, and HBr, they were able to evaluate the absolute rate coefficient, k_1 for the $E \rightarrow V$ process $[Br^* + HX(v = 0) \rightarrow Br + HX(v = 1)]$. Rate coefficients for the other quenching mechanisms, $k_0 [Br^* + HX(v = 0) \rightarrow Br + HX(v = 0)]$ and $k_2 [Br^* + Br_2 \rightarrow Br + Br_2]$ were also determined.

The Br* emission followed a simple exponential decay on quenching predominately from Br₂ and HX such that $[Br^*]_t \propto \exp[-(k_0 + k_1)[HX] + k_2 [Br_2])t]$. The quenching rate coefficients were determined by plotting the overall quenching rate, $1/(P_{HX} + P_{Br_2})\tau$, versus the mole fraction of HX, X_{HX} . The total quenching rate coefficient, $(k_0 + k_1)$, for Br* + HX and the quenching coefficient k_2 for Br₂ were evaluated as X_{HX} went to 1 and 0, respectively. The $E \rightarrow V$ rate coefficient, k_1 , was calculated, and Leone and Wodarczyk found that at least 50 percent of the HX quenching of Br* was due to $E \rightarrow V$ transfer.

Table 2.2

Br($^2P_{1/2}$) Spin-Orbit Relaxation Rate Coefficients

Quenching Gas	Quenching Rate Coefficient (10^{-12} cm ³ /molec-s)	Ground State ω_e^{20} or Vibrational Frequencies ²⁶ (cm ⁻¹)	Quenching Rate Reference
Ar	< 0.0002		1
Br ₂	19.0 1.2 \pm 0.3 0.99 \pm 0.09 0.48 \pm 0.05 0.47 \pm 0.04	323.2	1 2 3 4 5
BrCl	0.029 \pm 0.014	430.0	5
CF ₃ Br	0.05		1
CF ₄	0.21		1
CH ₄	4.2		1
Cl ₂	0.022 \pm 0.014	564.9	5
CO	0.0073 0.01081 \pm 0.00056	2170.21	1 27
CO ₂	15 \pm 1	ν_1 = 1388.17 ν_2 = 667.40 ν_3 = 2349.16	7 9 28
COS	1.4 \pm 0.1	ν_1 = 2062.22 ν_2 = 520.4 ν_3 = 858.9	9
CS ₂	1.1 \pm 0.1	ν_1 = 657.98 ν_2 = 396.7 ν_3 = 1532.5	9
D ₂	5.7 0.68	2297	1 27
D ₂ O	9.6 2.2 \pm 0.4		1 28
H ₂	4.7 2.7	4395.2	1 27
H ₂ O	32 62 51 \pm 3	ν_1 = 3657.0 ν_3 = 1594.7 ν_3 = 3755.7	1 16 28

Br(²P_{1/2}) Spin-Orbit Relaxation Rate Coefficients, Continued

HBr	1.1 1.4 0.84 ± 0.11	2649.67	1 16 4
HCl	8.6 5.2 ± 0.4	2989.74	16 4
HCN	20 ± 2	$\nu_2 = 423$ $\nu_3 = 1475$	2
HD	6.4	3817.09	27
HDO	19 ± 4		28
HF	34 ± 6	4138.52	8
I ₂	1.86 ± 0.37	214.57	5
IBr	3 1.0 ± 0.14	268.4	1 5
ICl	0.9 ± 0.4	384.18	5
N ₂	0.0025	2359.61	1
N ₂ O	2.6 ± 0.8 3.1 ± 0.9	$\nu_1 = 2223.76$ $\nu_2 = 588.78$ $\nu_3 = 1284.9$	7 3
NO	47 2.0 5.3	1904.03	1 16 29
O ₂	34 0.0015 ^{+ 0.0004} _{- 0.0015}	1580.361	1 23

Wodarczyk and Sackett performed similar quenching rate measurements for Br^* and HF, but improved on Leone's apparatus.⁸ These researchers added monitors for the incident and transmitted laser intensity. They found the logarithm of the intensity ratio to be linearly proportional to the Br_2 pressure. In this way, they were able to continuously measure the mole fraction of Br_2 present in the reaction cell. Again using procedures similar to Leone, the researchers found values for the same three rate coefficients. Wodarczyk and Sackett determined the rate for Br_2 self-quenching to be $1.03 \pm 0.2 \times 10^{-12} \text{ cm}^3/\text{molecule-s}$, and they found HF quenching of Br^* to be $3.4 \pm 0.6 \times 10^{-11} \text{ cm}^3/\text{molecule-s}$. By analyzing the rate coefficients, the atom quenching was found to be nearly 100 percent $\text{E} \rightarrow \text{V}$ transfer. Virtually all of the HF molecules have ro-vibrational transitions which are within $3/2 \text{ kT}$ of energy resonance with the Br^* at room temperature, and the researchers believe this resonance results in the rapid HF quenching rate coefficient.

Hariri and others studied Br^* quenching by HCN,² CO_2 , COS, and CS_2 .⁹ In their experiments, a pulsed dye laser was used to photodissociate the Br_2 , and the rate coefficients were calculated by monitoring the time-resolved fluorescence from the quenching molecule. The researchers determined the Br_2 parent-molecule quenching rate on Br^* to be $1.2 \pm 0.3 \times 10^{-12} \text{ cm}^3/\text{molecule-s}$, which is equal within experimental error to the rate determined by Wodarczyk and Sackett.

In the case of HCN, although a large number of quenching channels are available, the efficient excitation of the ν_3 mode, or (001) state, results in Equation (2.2) being the major quenching route.²



In fact, the researchers determined that 88 percent of the quenching collisions resulted in excitation of the HCN ν_3 mode, and thus concluded that Br^* quenching by HCN results in the production of (001) rather than a combination state like (011). They cited the excitation of HCN(001) by energy transfer from Br^* as an example of a fast, specific $E \rightarrow V$ rate process.

The researchers found that CO_2 was an order of magnitude more efficient quencher than were COS or CS_2 . Additionally, the fraction of energy transferred from Br^* to available ν_3 excitation was also larger for CO_2 than for COS or CS_2 , which may indicate the importance of energy resonance, as well as the number of quanta exchanged, in the energy transfer process.⁹

The fraction of Br^* quenching collisions that result in the excitation of one ν_3 quantum per molecule was found to be approximately 40 percent for CO_2 and CS_2 and 20 percent for COS. While the $\text{CO}_2(101)$ state was identified as the major product channel for Br^* quenching, the product energy states for COS and CS_2 were not determined. The $E \rightarrow V$ transfer from Br^* must either involve a molecular state composed of more than two vibrational quanta if the process is resonant, or a large energy defect if only two quanta are to be exchanged. Hariri and Wittig found that "...when a

molecule is an efficient quencher of Br^* , the main quenching channel is likely to be $\text{E} \rightarrow \text{V}$ transfer".⁹

Hofmann and Leone then investigated the collisional deactivation of Br^* atoms with halogen and interhalogen molecules. They determined the Br^* quenching rate coefficients for Br_2 , IBr , ICl , BrCl , and Cl_2 , but found that the rate coefficients varied over two orders of magnitude. These differences caused them to state that, "The relatively small vibrational quanta associated with the halogen and interhalogen molecules. . .do not support the idea of an effective $\text{E} \rightarrow \text{V}$ transfer mechanism".⁵

In 1978, Grimley and Houston indirectly monitored the $\text{E} \rightarrow \text{V}$ energy transfer from Br^* to H_2 , HD , and D_2 by observing subsequent vibrational-to-vibrational energy transfer from excited hydrogen to CO .²⁷ The researchers used this indirect method because experimental observation of vibrational excitation in H_2 is difficult due to the lack of a dipole moment.

Their results showed a high fraction of Br^* energy being transferred to H_2 and HD vibrations while a low fraction was transferred to the D_2 vibration. Their measured rate coefficients were not noteworthy except for the low fraction of energy transfer to D_2 and that quenching of Br^* by D_2 is not dominated by an $\text{E} \rightarrow \text{V}$ channel.

Kushawaha measured the quenching rate coefficients of Br^* by N_2O using time-resolved fluorescence.³ A flashlamp-pumped dye laser operating at 485 nm was used to produce Br^* atoms. An LN_2 -cooled InSb detector was used to observe fluorescence signals from Br^* and $\text{N}_2\text{O}(001)$. By analysis of the Br^* data, the parent-molecule Br_2 quenching rate was determined to be $0.99 \pm 0.09 \times 10^{-12} \text{ cm}^3/\text{molecule-s}$, in good agreement with the results from both the Wodarczyk and Hariri research groups. Rates of deactivation of

$\text{N}_2\text{O}(001)$ by ground state N_2O and Br_2 and inert gases were also calculated. By comparing the intensities of Br^* and $\text{N}_2\text{O}(001)$ emissions, the rate of $\text{E} \rightarrow \text{V}$ transfer from Br^* to N_2O was determined to be 24.5 ± 4 percent of the total quenching rate.

Wight investigated Br^* quenching by nitric oxide (NO) trying to resolve discrepancies in previously reported values.²⁹ Bromine atoms were generated by photolysis of CF_3Br by an ArF excimer laser producing 20 to 40 mJ of energy per pulse at 193 nm. The $\text{NO}(\nu=2)$ level is 3724 cm^{-1} above the ground state, which is close to the electronic energy of Br^* , 3685 cm^{-1} . As mentioned above, Donovan and Husain had previously reported the NO quenching rate on Br^* to be $4.7 \times 10^{-11} \text{ cm}^3/\text{molecule-s}$; an apparently large rate suspected to be due to the paramagnetic nature of NO. Wight suggests that resonance effects are more important than the paramagnetic nature of the quenching molecule in determining the magnitude of quenching rate coefficients. Because Br_2 reacts with NO at room temperature under certain conditions to form nitrosyl bromide, BrNO , CF_3Br is used as a Br^* precursor. In an investigation of Br^* and BrNO collisional quenching, Wight found that $\text{E} \rightarrow \text{V}$ transfer from Br^* produces an emission from vibrationally excited BrNO near $5.4 \text{ }\mu\text{m}$.

Wight found that the energy transfer from Br^* was insufficient to excite NO levels above $\nu = 2$. The observed fluorescence near $5.4 \text{ }\mu\text{m}$ is attributed only to the NO (2-1) and (1-0) vibrational transitions. The transition moment for the 2-1 transition is approximately twice that of the 1-0 transition, which means the emission intensity is proportional to the total number of vibrational quanta excited in the NO molecules, and is virtually independent of the vibrational state distribution.

Through the use of a cold gas filter to distinguish between emission from molecules in the $v = 2$ and the $v = 1$ state, Wight concluded that approximately 84 percent of the $E \rightarrow V$ transfer collisions result in the formation of the $\text{NO}(v = 2)$ state and 14 percent for the $\text{NO}(v = 1)$ state. The fraction of collisions which leave NO molecules in the $v = 0$ state is negligible at 2 percent. These results are important to the NO laser development in this research.

Relaxation from the $\text{NO}(v = 2)$ state is dominated by collisions with ground state NO molecules forming two $\text{NO}(v = 1)$ molecules. Wight determined the rate coefficient for this reaction to be $1.2 \pm 0.4 \times 10^{-12} \text{ cm}^3/\text{molecule-s}$ which is in good agreement with previous researchers.

In follow-on research, Sedlacek and Wight performed an investigation of $E \rightarrow V$ energy transfer from Br^* to nitrosyl bromide.³⁰ The Br^* atoms are formed by the photodissociation of Br_2 at 500 nm with an excimer pumped dye laser. Emission was detected from the $2 - 1$ and $1 - 0$ transitions of BrNO excited by the $E \rightarrow V$ transfer from Br^* . Isolation of the $\text{BrNO}(2 - 1)$ emission is accomplished by using a cold gas filter to block the $1 - 0$ transition. In the limit of a harmonic approximation, the spontaneous emission ratio of the $2 - 1$ band is twice that of the $1 - 0$ band, and from the ratio of the two emission intensities, the vibrational distributions are calculated.

Initially, the similarity of the stretching frequencies of NO (1875 cm^{-1}) and BrNO (1800 cm^{-1}) led Wight to believe that $E \rightarrow V$ transfer from Br^* to BrNO could be highly selective in populating two quanta of the v_1 vibrational mode. But the results of the cold gas filter indicated that more than six times as many BrNO molecules are formed with one quantum of the N-O

stretching mode as are formed with two quanta. This fact is very important to the $\text{Br}^*\text{-NO}$ laser demonstration discussed later in this document. About 50 percent of the quenching collisions take place by $\text{E} \rightarrow \text{V}$ energy transfer, and the remaining 50 percent via energy transfer mechanisms not involving the ν_1 vibrational mode or by reactive quenching to form Br_2 and NO .

Taatjes, Leone, and others described their research of O_2 , H_2O , D_2O , and HDO quenching of Br^* using a two-laser, pump-probe method.²⁸ The relative rates for the water species, H_2O , D_2O , and HDO , could be explained by existing $\text{E} \rightarrow \text{V}$ models based on dipole-quadrupole coupling, but the quenching of Br^* by O_2 was found to be slower by four orders of magnitude than previously reported values. Approximately 35 percent of the measured rate for oxygen could be attributed to possible water and CO_2 impurities in the sample. For this reason, the quoted rate is an upper limit on the true quenching rate.

Sedlacek and Weston used high resolution, time-resolved, diode laser spectroscopy to investigate the $\text{E} \rightarrow \text{V}$ energy transfer from Br^* to CO_2 .³¹ Their study was the first confirmation by direct observation that $\text{CO}_2(101)$ is the primary Br^* quenching channel. Of more importance is the fact that $\text{CO}_2(101)$ is the sole recipient of the Br^* energy. The Fermi resonant (021) state receives only a negligible amount of the spin-orbit excited bromine energy, probably due to the fact that dipole-quadrupole long-range forces are very sensitive to the energy mismatch in the $\text{E} \rightarrow \text{V}$ transfer step. The researchers determined that 66 percent of the Br^* energy appeared as energy in the (101) vibration. They also determined $\text{E} \rightarrow \text{V}$ and $\text{V} \rightarrow \text{V}$ rate coefficients which agreed favorably with previously-determined values.

a) Quenching Rate Temperature Dependence Studies

Several mechanisms, such as long-range multipolar interactions, short-range repulsive interactions, and nonadiabatic curve crossings have been suggested as being responsible for the $E \rightarrow V$ transfer from Br^* to small molecules.³² In those systems where $E \rightarrow V$ transfer has been identified as a major quenching channel, rate coefficient temperature dependence may help distinguish between these various energy transfer mechanisms as in the case of vibrational-to-vibrational energy transfer.

It is observed that when the number of vibrational quanta excited is small and a near-resonant channel is available, the transfer process is often fast, efficient, and mode specific.³³ This fact has been exploited to build molecular lasers based on the transfer of energy from Br^* .

The temperature dependence of the quenching of I^* by a number of collision partners has been previously reported. Cline and Leone measured the temperature dependence of the bimolecular quenching rate of I^* by I_2 from 300 to 800 K. The rate was found to be nearly independent of temperature due to the stability of an I_3 intermediate species.³⁴

Reisler and Wittig used laser induced fluorescence to measure the temperature-dependent quenching of Br^* by HCl and CO_2 .³² The fluorescence cell was housed in a temperature controlled furnace using nichrome wire as the heat source. Br^* was created using a flashlamp-pumped dye laser (1–4 mJ) operating near 490 nm. Time-resolved fluorescence from the molecular species was collected using an InSb detector for cell temperatures from 296 to 608 K. Br^* collisional lifetimes were measured at seven temperatures within the range. The quenching species mole fraction was varied and quenching rate coefficients for Br_2 and the

molecular species were calculated. A portion of the sample was directed to a second cell maintained at room temperature, where the rate coefficient was measured concomitantly to determine the room temperature quenching rate.

Reisler and Wittig pointed out that the change in the gas temperature causes a change in the average velocity, \bar{v} , of the molecules and therefore a corresponding change in the collision frequency.³² It is thus useful to convert the measured rate coefficients into average cross sections ($\sigma = k/\bar{v}$). The quenching rate coefficient's increase purely due to the increased number of collisions is corrected for by the increase in the average velocity in the denominator.

The researchers found that the quenching cross section for CO₂ exhibited a negative temperature dependence, a trend expected for a long-range interaction near resonance.³² HCl($v = 1$) was expected to have a positive temperature dependence since it has an energy defect of 789 cm⁻¹ with Br*. Instead, the researchers found the HCl deactivation cross sections to be nearly independent of temperature in the range 300–600 K. The large cross sections cannot be accounted for by long-range multipolar interaction since the energy transfer is quite far from resonance. It was proposed that the E → V transfer takes place by nonadiabatic transitions between curve crossing potential surfaces.

Reisler and Wittig also researched the temperature-dependent quenching cross sections for the collisional deactivation of Br* by ¹²CO₂ and ¹³CO₂.³³ The experimental arrangement was the same used in the aforementioned study. The ¹²CO₂ deactivation rate was found to be approximately twice as fast as the ¹³CO₂ rate. The CO₂ quenching cross sections were both found to decrease with increasing temperature in the

range 296–600 K, which indicated that near-resonant channels dominate the quenching processes in both molecules. Although the statistical uncertainties varied from $\pm 5\%$ at room temperature to $\pm 15\%$ at the highest temperature, the trend for decreasing cross section with increasing temperature was reproducible in every experiment.³³ They also found that the quenching cross sections of Br^* by Br_2 are only weakly dependent on temperature in the range 300–600 K.

Reisler and Wittig pointed out that even though the total quenching rate coefficient of Br^* by $^{13}\text{CO}_2$ is smaller than that by $^{12}\text{CO}_2$, the fraction of the quenching collisions going into the ν_3 state is nearly equal. This implies the mode specificity of the quenching process is maintained. In general, these experimental results indicate that in near-resonant $E \rightarrow V$ energy transfer processes involving halogen atoms in the $^2\text{P}_{1/2}$ state, long-range multipolar interactions are of major importance.³³

2. *Laser Demonstrations*

Research has been performed since 1970 to determine new lasing gases using $E \rightarrow V$ energy transfer from $^2\text{P}_{1/2}$ excited bromine atoms. In 1975, Peterson and others were able to obtain considerable population inversions and stimulated emission by using excited bromine atoms to selectively excite the polyatomic species CO_2 , N_2O , HCN , and C_2H_2 .⁷

The experimenters used flash photolysis to prepare the Br^* atoms in the presence of the polyatomic molecule. The resulting $E \rightarrow V$ transfer process selectively pumps the polyatomic molecule into specific energy states. The CO_2 data indicated that nearly 40 percent of the quenching collisions resulted in excitation of vibrational modes containing the ν_3 asymmetric

stretch mode. The N_2O data indicated that the N_2O quenching rate is six times slower than the CO_2 rate. Also of interest is the fact that for N_2O , a considerable amount of energy appears to be in the ν_1 as well as the ν_3 mode.

Stimulated emission from HCN and C_2H_2 was observed under similar experimental conditions. Of interest is that both the CO_2 and HCN processes initiated by photolysis appeared to be reversible, and a single gas fill could be used repeatedly. This fact has strong implications for fielding such a vibration-rotation laser based on the $\text{E} \rightarrow \text{V}$ energy transfer process.

For the energy transfer to take place, there must be a transition from the potential surface involving Br^* to the surface for Br. These potential surfaces are sensitive to which part of the polyatomic molecule interacts with the bromine atom. Since the potential curves for systems they examined are all repulsive, the requirement for resonant energy transfer, as in the $\text{V} \rightarrow \text{V}$ case, is slightly relaxed as some of the energy defect is made up by recoil of the products. It is precisely this fact that may account for why some quenching gases with large energy defects have quenching rates greater than the rates for some gases with smaller energy defects.

In follow-on research, Peterson and Wittig reported early in 1976 that a pulsed CO_2 laser operating at 4.3, 10.6, and 14.1 μm had been developed. The laser produced pulse energies of 112 mJ at 10.6 μm by flash photolyzing 80 Torr of a 1 : 1 mixture of Br_2 and CO_2 .⁶

By observing 4.3 and 14.1 μm laser transitions, the researchers determined the (101) and (021) states, shown in Figure 2.9, receive the largest amount of Br^* excitation energy. Gas mixtures of 4 Torr Br_2 , and 50 mTorr CO_2 produced approximately 0.1 mJ of energy at 4.3 μm . The

2304 cm^{-1} of energy was assigned to the *P*-branch of either the (101)–(100) or (021)–(020) band.

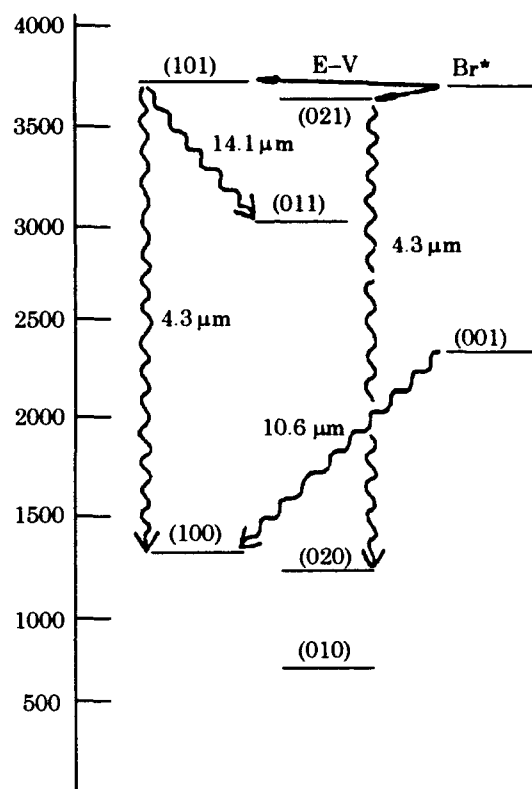
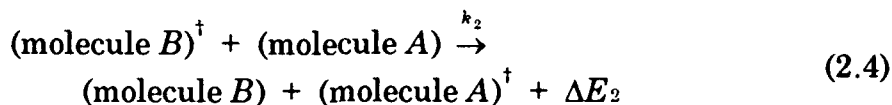
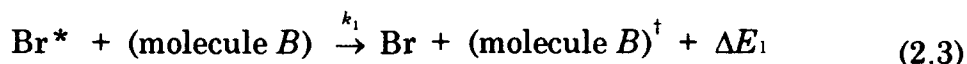


Figure 2.9. Partial energy-level diagram of the Br^* – CO_2 system showing electronic-to-vibrational energy transfer and observed laser transitions⁶

The researchers felt that their results suggested a number of device applications. Since photolysis light requires several passes through the gas to be absorbed, a flashlamp concentric with the laser medium should be considered. Since the Br atoms recombine to form Br_2 and the CO_2 is chemically inert in this application, a sealed-off laser system seems feasible.

Finally, the data suggests that operation at ≥ 1 atmosphere should be possible. The aforementioned facts made this system suitable for study in this research.

In a second follow-on research effort, Peterson, Braverman, and Wittig obtained stimulated emission from H_2O , NO , and N_2O .³⁵ A distinction is made between direct and indirect $\text{E} \rightarrow \text{V}$ energy transfer. When *direct* $\text{E} \rightarrow \text{V}$ excitation is not possible as in the cases of H_2O and NO , an *indirect* excitation involving sequential $\text{E} \rightarrow \text{V}$ and $\text{V} \rightarrow \text{V}$ transfers with an intermediate molecule produce population inversion. The two-step excitation process is shown in Equations (2.3) and (2.4):



This indirect excitation is necessary when the Br^* quenching rate coefficient for molecule A is not large enough to allow vibrational excitation to occur in a mode-specific manner thus allowing population inversion. Peterson applied this indirect approach to the N_2O laser; using either HCl or CO_2 for molecule B . The indirect excitation produced N_2O laser pulses of several mJ on the P -branch of the (001)–(100) band near $10.9 \mu\text{m}$; the direct method did not produce laser oscillation.

The H_2O laser operated at many transitions in the $7\text{--}8 \mu\text{m}$ region of the (020)–(010) vibrational band and one unassigned transition at $16.9 \mu\text{m}$.

The combined energy of the five strongest transitions is estimated to be 100–500 μJ .

Following flash photolysis of a mixture of 50 percent Br_2 , 45 percent He, and 5 percent NO, lasing occurs near 1817 cm^{-1} , which corresponds to the center of the *P*-branch of the NO(2, 1) band. The transition frequency varied from pulse to pulse, which made precise frequency measurement difficult. The research team estimated the gain of the device at 5 percent per pass with output energies somewhat less than the $\text{Br}^*-\text{H}_2\text{O}$ system.

When NO and Br_2 are combined, they may react to form NOBr when allowed to come to equilibrium in the presence of room light. In the absence of an external light source, NO and Br_2 remain stable for several hours. The research team found that when the system was exposed to room light, it did not lase until the second pulse. They attributed this behavior to the reaction of Br and NOBr to form NO plus Br_2 . That is, the first flash regenerates enough NO to allow subsequent flashes to excite NO lasing. In the absence of room light, the Br_2 and NO formed a stable mixture, and lased on the first and subsequent flashes.

In order to establish $\text{E} \rightarrow \text{V}$ energy transfer as the NO excitation process, Peterson showed that when photolysis light is restricted to $\lambda > 300\text{ nm}$, very little NOBr photolysis and no vibrational excitation occurs, and the photodissociation of NOBr is unimportant in the production of vibrationally-excited NO. Since NO($v = 3$) lies nearly 1900 cm^{-1} above Br^* , $\text{E} \rightarrow \text{V}$ excitation of NO is only significant for $v \leq 2$. For these and other reasons, Peterson's team concluded that the observed NO lasing occurred on the (2, 1) band.

Recently, Pastel and others reported successful demonstration of a Br^{*} pulsed laser operating at 2.71 μm using photodissociation of IBr at 532 nm from a frequency-doubled Nd:YAG pump laser.¹⁰ Pulsed energies up to 3 mJ at 10 Hz were reported with operation stable for hours with a single gas fill. A quantum efficiency of 8 percent was calculated using the maximum pump energy conversion efficiency of 1.5 percent determined from the ratio of Br^{*} to YAG pulse energies.

The researchers also reported lasing on ro-vibrational transitions of CO₂ at 4.3 μm and HCN at 3.9 μm by E \rightarrow V transfer from the photolytically generated Br^{*}. In the case of CO₂, the 4.3 μm lasing occurs from the energy transferred to the (101) vibrational level emitting to the (100) vibrational level. The researchers measured 0.1 mJ of laser output energy in a 200 ns pulse occurring 350 ns after the pump pulse. The CO₂ laser operated for CO₂ pressures from 0.25 to 1 Torr; the upper pressure limit is due to rapid excited CO₂ quenching by ground state CO₂.

HCN lasing was seen from the (100) vibrational mode to the (010) vibrational mode at power levels too low to accurately measure. The lasing pulse started about 200 ns after the lasing pulse and was 100 ns long.

III. Atomic Bromine Excitation and Quenching Experiments

A. Introduction

One of the primary goals of this research is to determine the quenching rates for selected gases on the spin-orbit excited state of atomic bromine, $\text{Br}(^2\text{P}_{1/2})$. There were discrepancies reported from previous research between parent-molecule quenching rates, that is, the Br_2 on Br^* rate.²⁵ Pulsed lifetime photolysis studies are used to determine the absolute Br_2 and CO_2 room-temperature quenching rates. Steady state photolysis methods are then used as a novel approach to more rapidly determine the relative quenching rates for 23 additional gases.

Quenching rate temperature dependence is examined for selected gases and analyzed on the basis of previous results. Diffusion and three body effects are examined to determine the slowest steady-state quenching rate measurable from this experimental technique.

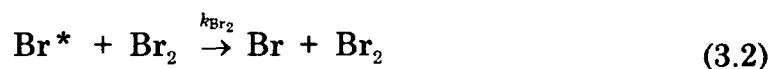
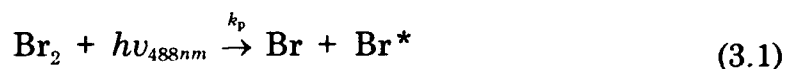
This chapter begins with a section on background theory pertinent to the photolysis experiment, which includes pulsed and steady-state kinetics and master rate equation development. Next, a section on the pulsed and steady-state experimental setup and operation is given. The final two sections cover the experimental results and a discussion of the implications of this portion of the research.

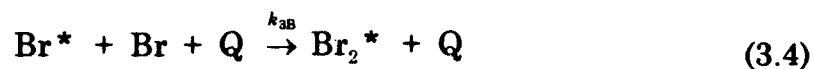
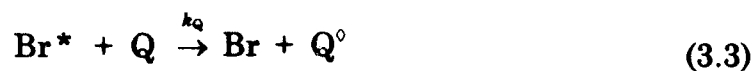
B. Theory of Photolysis

1. $Br(^2P_{1/2})$ Excitation and Quenching Kinetics

The spin-orbit relaxation of the $Br(^2P_{1/2})$ excited state to the $Br(^2P_{3/2})$ ground state may occur from collisionless and collisional energy transfer processes. Additionally, the transitions may be either radiative or non-radiative, while collisionless processes involve spontaneous emission. Collisional processes include electronic-to-vibrational energy transfer, reactive processes, and three body recombination. For Br^* , non-radiative rates are much greater than the slower radiative rate which is not significant in determining the Br^* lifetime.

By combining the various effects discussed above, the equations below are developed to describe the principal mechanisms for $Br(^2P_{1/2})$ production and quenching. Equation (3.1) describes the photodissociation of the bromine molecule into the ground state and excited state atoms. Equation (3.2) characterizes the spin-orbit relaxation brought about by interaction with a bromine molecule. If an added quenching species, Q, is present, Equation (3.3) describes that quenching interaction. Equation (3.4) models three body recombination with an arbitrary species, Q, which yields an excited bromine molecule. Equation (3.5) considers the effect of excited bromine wall deactivation. Finally, Equation (3.6) models spontaneous emission at 2.71 μm :





The rate equation representing the above reactions can be written as

$$\begin{aligned} \frac{d[\text{Br}^*]}{dt} = & k_p I_p [\text{Br}_2] - k_{\text{Br}_2} [\text{Br}^*] [\text{Br}_2] - k_Q [\text{Br}^*] [\text{Q}] \\ & - k_{3B} [\text{Br}^*] [\text{Br}] [\text{Q}] - k_{\text{wall}} [\text{Br}^*] - k_r [\text{Br}^*] \end{aligned} \quad (3.7)$$

where

$$[\text{Br}_2] = \text{Br}_2 \text{ concentration (molec cm}^{-3}\text{)}$$

$$[\text{Br}^*] = \text{Br}^* \text{ concentration (atoms cm}^{-3}\text{)}$$

$$[\text{Br}] = \text{Br concentration (atoms cm}^{-3}\text{)}$$

$$[\text{Q}] = \text{quenching species concentration (molec cm}^{-3}\text{)}$$

$$k_p = \text{pump rate coefficient (cm}^2 \text{ watt}^{-1} \text{ sec}^{-1}\text{)}$$

and where

I_p = pump laser intensity (watts cm^{-2})

k_Q = quenching rate coefficient ($\text{cm}^3 \text{ molec}^{-1} \text{ sec}^{-1}$)

k_{3B} = 3 - body rate coefficient ($\text{cm}^6 \text{ molec}^{-2} \text{ sec}^{-1}$)

k_{wall} = wall rate coefficient (sec^{-1})

k_r = radiative rate (sec^{-1})

2. Steady-State Analysis

Under steady state conditions, such as CW excitation, the excited bromine time derivative equals zero, yielding

$$\begin{aligned} k_p I_p [\text{Br}_2] - k_{\text{Br}_2} [\text{Br}^*] [\text{Br}_2] - k_Q [\text{Br}^*] [\text{Q}] - k_{3B} [\text{Br}^*] [\text{Br}] [\text{Q}] \\ - k_{\text{wall}} [\text{Br}^*] - k_r [\text{Br}^*] = 0 \end{aligned} \quad (3.8)$$

Combining the non-pressure dependent terms, k_{wall} and k_r , into k_o , assuming the three body rate is small (an assumption that is later experimentally verified), and solving the resulting equation for $[\text{Br}^*]$ yields

$$[\text{Br}^*] = \frac{k_p I_p [\text{Br}_2]}{k_{\text{Br}_2} [\text{Br}_2] + k_Q [\text{Q}] + k_o} \quad (3.9)$$

Within a constant of proportionality, K , which includes the spontaneous emission rate, absolute radiometry factors, and detector sensitivity, the intensity of the Br^* emission at $\lambda = 2.71 \mu\text{m}$ is

$$I_{2.71\mu} = K \frac{k_p I_p [\text{Br}_2]}{k_{\text{Br}_2} [\text{Br}_2] + k_Q [\text{Q}] + k_O} \quad (3.10)$$

Figure 3.1 shows Equation (3.10) for the case of no quenching gases, $[\text{Q}] = 0$. The figure shows an initial rapid increase in emission intensity as the dissociating laser produces more Br^* due to the Br_2 pressure increase; the non-pressure dependent term, k_O , being the dominant Br^* deactivation mechanism. As the pressure continues to increase, the emission intensity starts to increase at a slower rate due to the increased deactivation from the bromine self-quenching term, $k_{\text{Br}_2} [\text{Br}_2]$. Finally, as the bromine pressure increases above a few Torr, $k_{\text{Br}_2} [\text{Br}_2] \gg k_O$, and the emission intensity approaches its asymptotic value of

$$I_{2.71\mu} \approx K \frac{k_p I_p}{k_{\text{Br}_2}} \quad (3.11)$$

The parameters used with the abscissa in units of Torr are $k_p I_p = 26 \text{ sec}^{-1}$, $k_{\text{Br}_2} = 4 \times 10^4 (\text{sec-Torr})^{-1}$, and $k_O = 1.2 \times 10^4 \text{ sec}^{-1}$. These parameters are chosen to make the predicted intensity represent previously-reported emission intensity plots.²⁵

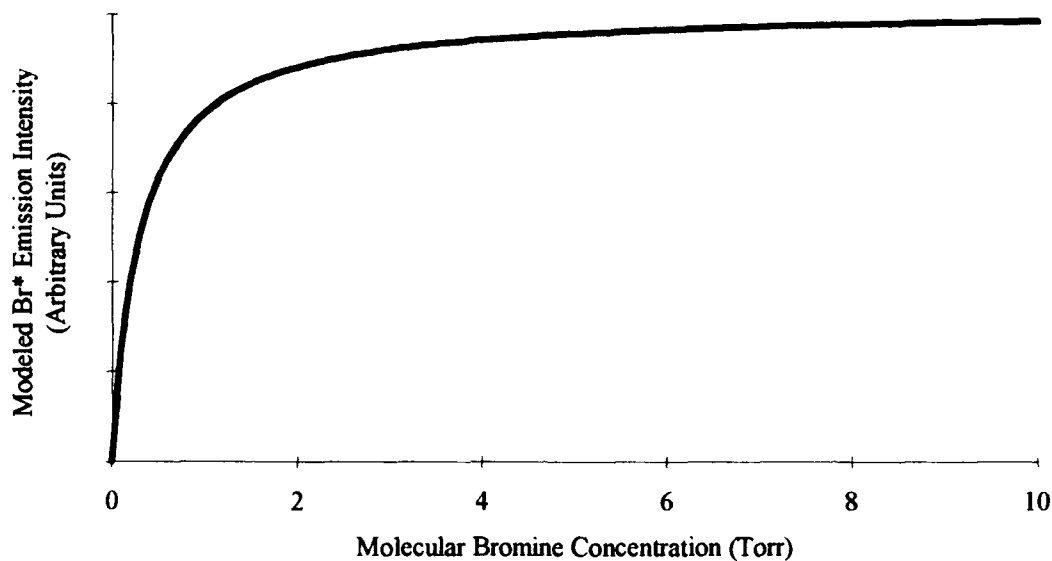


Figure 3.1. Predicted Br* emission intensity versus molecular bromine concentration from Equation (3.10) with $[Q] = 0$.

With no quenching gas present, the Br* emission intensity can be represented as a Stern-Volmer plot by plotting Br₂ concentration divided by Br* intensity as a function of Br₂ concentration, as shown below:

$$\frac{[\text{Br}_2]}{I} = \frac{k_o + k_{\text{Br}_2} [\text{Br}_2]}{K k_p I_p [\text{Br}_2]} * [\text{Br}_2] \quad (3.12)$$

Equation (3.12) is of the form $y = mx + b$ which yields a slope and intercept given in Equation (3.13):

$$\begin{aligned}
y &= \frac{[\text{Br}_2]}{I} \\
m &= \frac{k_{\text{Br}_2}}{K k_p I_p} \\
b &= \frac{k_o}{K k_p I_p}
\end{aligned} \tag{3.13}$$

The slope-to-intercept ratio yields

$$\frac{m}{b} = \frac{k_{\text{Br}_2}}{k_o} \tag{3.14}$$

By expressing the Br* emission data in this way, data analysis yields the slope-to-intercept ratio, and by knowing k_{Br_2} , the value of k_o can be determined. Since k_o represents non-pressure dependent terms k_{wall} and k_r , this experimental method provides a way of determining these values.

Equation (3.10), which gives the 2.71 μm Br* intensity, is written in the form of Equation (3.15) below, and the effect of the quenching gas on the quiescent Br* signal can be assessed:

$$\frac{I [Q=0]}{I [Q \neq 0]} = \frac{k_Q [Q]}{k_{\text{Br}_2} [\text{Br}_2] + k_o} + 1 \tag{3.15}$$

Equation (3.15) can also be expressed as a linear equation in buffer gas concentration to yield a slope, m , and intercept, b , given as

$$m = \frac{k_Q}{k_{Br_2} [Br_2] + k_O} \quad (3.16)$$

$$b = 1$$

By collecting the Br^* emission intensity as a function of added buffer gas concentration, the buffer gas quenching rate coefficient can be calculated relative to the Br_2 quenching rate. Once the slope of Equation (3.16) is known from the emission intensity data, k_Q can be determined since k_O and $[Br_2]$ are known.

3. Pulsed Lifetime Analysis

Factoring out $[Br^*]$ in Equation (3.7), and setting the coefficient of $[Br^*]$ equal to Γ , an equivalent rate coefficient, yields Equation (3.17):

$$\begin{aligned} \frac{d [Br^*]}{dt} &= - (k_{Br_2} [Br_2] + k_Q [Q] + k_{wall} + k_r) [Br^*] \\ &= - \Gamma [Br^*] \end{aligned} \quad (3.17)$$

For pulsed photolysis, the Br^* creation is instantaneous on the time scale of interest. The source laser pulse is nanoseconds in duration while the Br^* lifetime is measured in microseconds. Rearranging terms and solving for the excited bromine concentration as a function of time gives

$$[\text{Br}^*] = [\text{Br}^*]_{t=0} \exp(-\Gamma t) \quad (3.18)$$

In this experiment, the data are adequately represented by a single exponential decay:

$$I(t) = I(0) \exp(-\Gamma t) \quad (3.19)$$

and the decay rates, Γ , depend linearly on the Br_2 concentration; this linear data presentation is called a Stern-Volmer plot. The slope of the Stern-Volmer data is the quenching rate coefficient. The intercept of the Stern-Volmer plot is the non-pressure dependent inverse lifetime.

4. *Effect of Diffusion and Three Body Recombination*

As shown in Equation (3.7), the wall and three body rate coefficients, k_{wall} and $k_{3\text{B}}$, respectively, may contribute to the overall excited bromine deactivation rate. The measured deactivation rate, especially for gases with very small quenching rate coefficients, can be affected by these terms. This section addresses the theory behind the experiments performed to determine the relative effects of these terms.

As previously stated, when molecular bromine is photodissociated by 488 nm light, ground and excited state bromine are formed in nearly equal proportions. When the molecular bromine is photolysed, the overall cell

pressure increases as there are more bodies in the cell after photolysis. This increase in pressure is caused by both ground and excited state atomic bromine, or by an increase in the total atomic bromine concentration. This increase in pressure is balanced by atomic bromine recombination processes primarily at the cell wall.

The combined effects of wall deactivation and diffusion have recently been analyzed.³⁶ The results of this analysis show that under certain kinetic conditions, radial concentration gradients cannot be neglected.

The observed deactivation rate, k_{obs} , is actually composed of two terms; k_w , and a second term, $k_{\text{diff}}(P)$, which describes the pressure-dependent diffusion process to the wall. For the case of cylindrical geometry, the relationship between these rates is shown in Equation (3.20):

$$\frac{1}{k_{\text{obs}}} = \frac{1}{k_w} + \frac{1}{k_{\text{diff}}(P)} \quad (3.20)$$

where

$$k_{\text{obs}} = \text{observed deactivation rate}$$

The terms k_w and $k_{\text{diff}}(P)$ are defined in Equations (3.21) and (3.22):

$$k_w = \left(\frac{\hat{\mu}}{2} \right) \frac{\gamma}{r} \quad (3.21)$$

where

$\hat{\mu}$ = average thermal velocity

γ = probability of deactivation at surface

r = wall radius in cm

and

$$k_{\text{diff}}(P) = \frac{\Phi D(P)}{r^2} \quad (3.22)$$

and where

Φ = diffusive parameter

$$D(P) = 0.0026280 \frac{\sqrt{T^3}}{P \sigma^2} \left(\text{Fick's diffusion coefficient, } \frac{\text{cm}^2}{\text{s}} \right)$$

with

T = temperature in K

M = mass in AMU

P = pressure in atmospheres

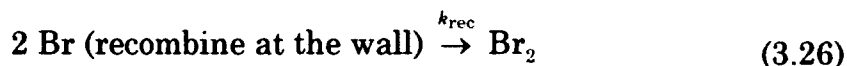
σ = molecular diameter in angstroms

Considering only processes that affect pressure changes, Equations (3.1) and (3.4) are written as





A postulated mechanism for bromine recombination at the wall is shown in the following two equations. First the bromine atoms attach to the cell wall as shown in Equation (3.25). As the atomic bromine concentration on the wall increases, eventually a bromine molecule is formed as shown in Equation (3.26):



Solving for the rate equation for the total atomic bromine concentration, $[\text{Br}]_{\text{T}} = [\text{Br}] + [\text{Br}^*]$, under steady-state conditions

$$\frac{d [\text{Br}]_{\text{T}}}{dt} = 2 k_p I_p [\text{Br}_2] - 2 k_{3B} [\text{Br}]_{\text{T}}^2 [\text{Br}_2] - k_{\text{obs}} [\text{Br}]_{\text{T}} = 0 \quad (3.27)$$

Solving for the atomic bromine concentration yields

$$[\text{Br}]_{\text{T}} = \frac{2 k_p I_p [\text{Br}_2]}{2 k_{3B} [\text{Br}]_{\text{T}} [\text{Br}_2] + k_{\text{obs}}} \quad (3.28)$$

When the dissociating laser is turned on, the total concentration of bodies in the cell, $[n]$, can be expressed as the sum of molecular and atomic bromine:

$$[n] = [\text{Br}_2] + [\text{Br}]_{\text{T}} \quad (3.29)$$

where the molecular bromine concentration equals the initial bromine concentration, $[\text{Br}_2]^0$ (before the laser is turned on), minus that lost to the dissociation process, as

$$[\text{Br}_2] = [\text{Br}_2]^0 - \frac{1}{2} [\text{Br}]_{\text{T}} \quad (3.30)$$

The total concentration is then given as

$$\begin{aligned} [n] &= [\text{Br}_2]^0 - \frac{1}{2} [\text{Br}]_{\text{T}} + [\text{Br}]_{\text{T}} \\ &= [\text{Br}_2]^0 + \frac{1}{2} [\text{Br}]_{\text{T}} \end{aligned} \quad (3.31)$$

The change in cell pressure that occurs when the dissociating laser is turned on is proportional to the total atomic bromine concentration, and is given in Equation (3.32):

$$\Delta P \propto \frac{1}{2} [\text{Br}]_{\text{T}} \quad (3.32)$$

By cycling the dissociating laser on and off through the bromine cell for various bromine pressures, the change in pressure can be used to determine the atomic bromine concentration.

C. Experiment

This section provides a detailed description of the steady-state and pulsed photolysis experimental apparatus. Issues and procedures critical to the experiment are also discussed. A detailed description of the steady-state and pulsed experimental procedures are provided in Appendix A.

1. Steady-State Experiment Equipment

The CW laser photolysis research utilizes an experimental apparatus shown in Figure 3.2, which is similar to that described by Tate.²⁵ The steady-state experimental apparatus is divided into four systems: the gas-handling system, the argon-ion laser, the absorption measurement and diagnostic system, and the detection and data collection system.

a) Gas Handling System

The gas-handling system consists of the bromine source, the mixing manifold, the reaction cell and temperature control unit, and the vacuum assembly. These subsystems are interconnected using 1/2 inch outside diameter (OD) in-line glass Teflon valves and 1/2 inch OD stainless steel flexible tube. The components are joined with 1/2 inch Cajon Ultra-Torr fittings. Each subsystem is described in the following paragraphs.

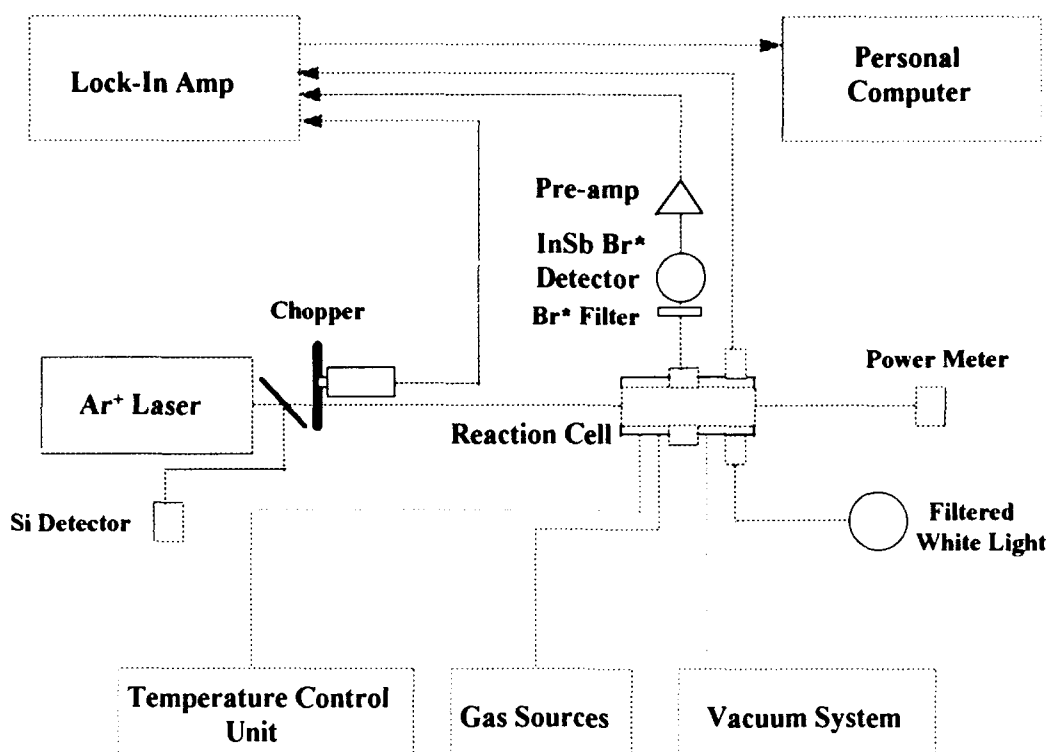


Figure 3.2. Schematic diagram of the steady-state photolysis experimental apparatus.

The bromine source consists of two glass bulbs, 2.75 inch OD and approximately 15 inches long, connected with Ultra-Torr fittings to a valve assembly. The two-bulb combination allows vacuum distillation and purification of the bromine. The molecular bromine (Spectrum 99.5%) is distilled using repeated freeze-thaw cycles with liquid nitrogen and liquid nitrogen/acetone slurries to remove impurities which may interfere with the $2.71 \mu\text{m}$ Br^* emission. CO_2 emissions near $2.71 \mu\text{m}$ have previously been observed in similar studies.^{5, 9} The distillation and purification procedure is described in Appendix B. The valve assembly facilitates the transfer of

bromine vapor to the mixing manifold, the vacuum assembly, or between the two bulbs.

The mixing manifold is designed to allow the controlled mixing of up to three gases in the reaction cell. The manifold is constructed of 1/4 inch OD stainless steel flex-tube joined with Swagelock fittings. There are three inlet lines and one outlet line which connects directly to the reaction cell via a 1/4 inch OD flex-tube and Ultra-Torr fittings. Each inlet has a Nupro 1/4 inch ball valve for positive cutoff and a Nupro 1/4 inch needle valve for precise gas flow control. Typical flow rates for bromine self-quenching experiments are 80 to 100 mTorr per minute. Buffer gas flow rates depend on the gas being used, and vary from 5 to 50 mTorr per minute for gases with rapid to moderate quenching rates and up to 150 mTorr per minute for gases with very slow quenching rates. The rates are adjusted to insure complete mixing of the buffer gas with the heavy bromine. The limit on the buffer gas flow rate is determined by the system leak plus outgasing rate which is less than 3 mTorr per hour. The system ultimate vacuum is 10^{-5} Torr using an oil diffusion pump.

The ball valve and needle valve are positioned very close to the reaction cell to eliminate molecular bromine from filling the buffer gas flex-tube. If the positive cutoff valve is not placed near the reaction cell, a *plug* of bromine is pushed into the reaction cell as the buffer gas is added to the cell. This increase in bromine pressure is seen as a momentary increase in Br^* emission intensity followed by a decrease in signal as the buffer gas enters the reaction cell. Such effects are monitored by the absorption diagnostic discussed below. Also, during quenching experiments, the buffer gas pressure at the mixing manifold is kept much higher than the Br_2 reaction

cell pressure. In this way, the loss of Br_2 into the buffer gas flex-tube is minimized.

The reaction cell is a 15 cm long, 7 cm diameter Pyrex cylinder with 5 cm diameter Pyrex windows on the ends to transmit the Ar^+ laser and with a 2.5 cm calcium fluoride (CaF_2) window (Oriel model 43371) on the side to monitor the $2.71 \mu\text{m}$ Br^* emission. The CaF_2 window provides approximately 90 percent transmission from 150 nm to $9 \mu\text{m}$.

For the nitric oxide and hydrogen chloride quenching studies, Spectra Physics single channel model 6410 gas detectors are mounted near the reaction cell for safety.

For the purpose of studying the temperature dependence of the buffer gas quenching rates, an outer cell jacket encircles the reaction cell cylinder to allow an oil bath to surround the cell. ILI Boss, 510 silicon fluid is used in the jacket, and 1/2 inch heat tape connected to a variable AC power supply is wrapped around the cell jacket. The silicon oil permits a more even temperature distribution within the reaction cell, and helps reduce temperature gradients in the gas. The internal cell gas temperature is monitored using a type K thermocouple attached to an Omega model DP41-TC temperature indicator. A programmable 0 to 10 volt DC output from the temperature indicator supplies a voltage to the data collection equipment proportional to the internal cell temperature.

The vacuum assembly consists of a liquid nitrogen (LN_2) cooled cold trap followed by a mechanical vacuum and 2-inch oil diffusion pump (Varian model SD 200 pump station). An ultimate vacuum of 10^{-4} Torr is achieved using only the mechanical vacuum pump, and the diffusion pump is not used in the experiments. As mentioned, the system leak plus outgassing rate was

less than 3 mTorr per hour. All system gases exit the reaction cell via the cold trap which is used to prevent gas vapor from reaching the pump oil, and the cold trap also increases the system vacuum. In-line glass Teflon valves are placed at each end of the cold trap to allow cold trap replacement without turning off the vacuum pump. The vacuum pump outlet is connected to an exhaust duct.

Both an MKS model 390H, 10 Torr, and a model 221A, 100 Torr capacitance manometers (Baratrons) are attached to the reaction cell for the purpose of monitoring the total gas pressure within the cell. Two pressure ranges are used and are determined by the desired experiment. The 0 to 10 volt outputs of the Baratrons are a linear representation of the measured pressure, and are applied to the data collection equipment for storage and analysis.

b) Argon-Ion Laser

A Spectra Physics model 164 Ar⁺ laser providing 900 mW of power at 488 nm is used to photodissociate the molecular bromine. Approximately 10 percent of the incident laser power is split-off and directed into an EG&G model SGD-100A photodiode to provide a relative indication of laser power and a means of correcting the atomic bromine fluorescence signal for variations in excitation rate. A 488 nm bandpass filter with a bandwidth of 1 nm FWHM is placed in front of the detector to facilitate tuning the laser for the maximum 488 nm power. The photodiode output is applied to the data collection equipment for storage and analysis.

The 1.2 mm laser beam is chopped (Stanford Research Systems model SR540) at 210 Hz to allow for synchronous detection which increases the Br^{*}

signal-to-noise (S/N) ratio. The chopped beam then propagates through the reaction cell and into a Coherent model 210 power meter.

An FND-100 photodiode is used to detect a portion of the transmitted Ar^+ power. This transmitted laser intensity is used to monitor the molecular bromine absorption at 488 nm. This procedure facilitates a real-time measurement of the on-axis molecular bromine absorption. A second absorption diagnostic using 409 nm light to monitor the molecular bromine concentration is described below.

c) Absorption Diagnostic System

The absorption measurement and diagnostic system is shown in Figure 3.3 below. The system consists of a white light source, fiber optic bundles, wavelength filters, and silicon detectors.

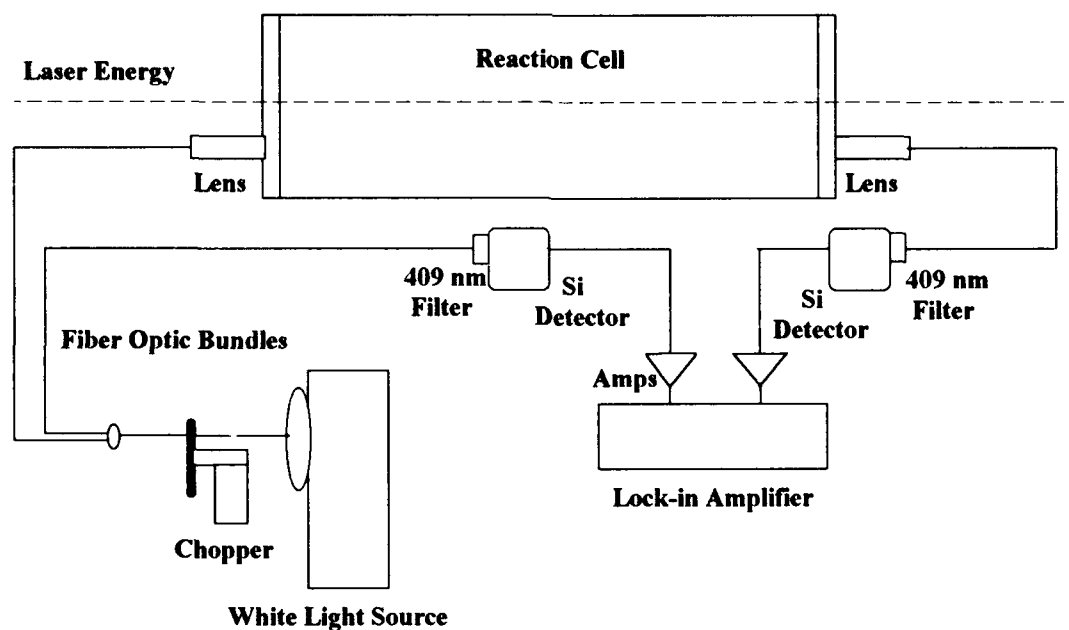


Figure 3.3. Absorption measurement and diagnostic system.

The white light source, an Oriel high intensity halogen lamp, is chopped at 200 Hz. A bifurcated fiber optic bundle divides the chopped light into two bundles. One source, I_t , is passed through the reaction cell and is subsequently filtered by a 409 nm filter and detected by a Hamamatsu model S2281 photodiode. After amplification, the signal is then directed to the lock-in amplifier (Stanford Research Systems model SR510) and finally to the data collection equipment for storage and analysis. The remaining source, I_{ref} , is applied directly to the silicon detector, and is used to correct the absorption for any deviations in lamp intensity.

The absorption equipment is used for two purposes; measuring bromine cross section for absorption as a function of molecular bromine concentration and as an absorption diagnostic used to monitor the absolute bromine concentration when adding buffer gases. This diagnostic is employed to insure complete mixing of the heavy bromine with added buffer gases and to assess the effects of adsorption of the bromine onto the cell walls.⁹ Changes in molecular bromine concentrations as low as 3 mTorr are observable.

The transmitted light intensity with the cell empty, I_o , and the transmitted intensity during the experiment, I_t , are measured by the detectors. The ratio of the intensities with and without Br_2 in the cell follows the Beer-Lambert law shown in Equation (3.33). As mentioned above, the reference intensity is included to correct for any deviations in lamp intensity:

$$\frac{I_t}{I_{ref}} = \frac{I_o}{I_{ref}} \exp(-\sigma l [Br_2]) \quad (3.33)$$

This 409 nm and the aforementioned 488 nm laser absorption diagnostic provide a continuous measurement of the molecular bromine cell concentration. Through the use of these diagnostics, the buffer gas flow rate and data collection rate are adjusted to insure complete mixing. This diagnostic is used during all steady-state quenching rate measurements.

As suggested by Hariri and Wittig,⁹ before the buffer gas is added to the reaction cell, the cell is *seasoned* by exposure to Br₂ to avoid adsorption into the cell walls which causes the static cell pressure to decrease with time. After the molecular bromine is added to the empty cell, the pressure decreases and more bromine is added until the desired operating pressure is reached. This procedure is repeated until no decrease is noted in the bromine cell pressure. After adding a few torr of Br₂ to an empty cell, the initial reduction in cell pressure before adding more Br₂ is 100 to 200 mTorr. After Br₂ is added to the cell to bring the pressure back to the desired level, much smaller cell pressure reductions are seen. The process of adding bromine to the cell can last slightly more than an hour until no changes are seen in the static molecular bromine pressure.

d) Detection and Data Collection

Figure 3.4 below is a schematic diagram of the Br* detection system. The detection system is composed of the CaF₂ window and lenses and infrared detector. The excited bromine side fluorescence is collected by a system of two CaF₂ lenses: a 1 inch diameter, 50 mm focal length lens and a 2 inch diameter, 100 mm focal length lens. The small lens is located approximately 50 mm from the laser beam axis. The larger lens is placed approximately 100 mm from the detector element. The separation between

the two lenses is not critical; 75 to 150 mm allows a minimum amount of beam divergence between the two lenses. The large lens focuses the weak $2.71\text{ }\mu\text{m}$ fluorescence on the detector.

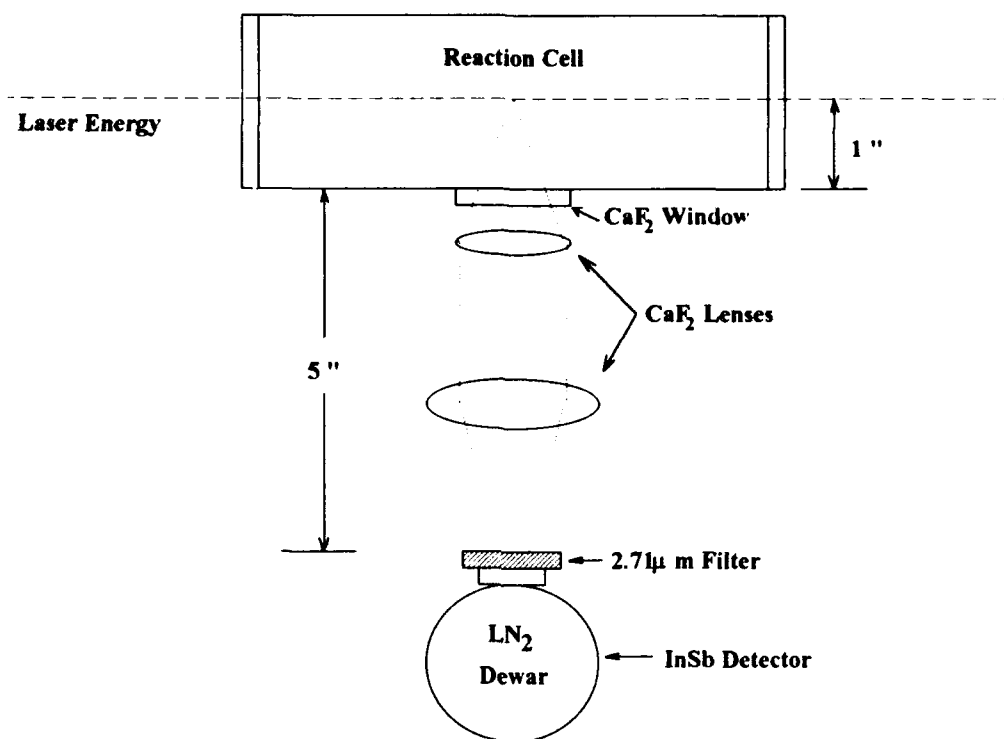


Figure 3.4. Br^* detection system.

The photovoltaic indium antimonide (InSb) detector (EG&G Judson model J10D-M204-R02M-60-SP35) is LN_2 cooled to 77 K, has a 2 mm diameter active area, and uses a sapphire window. The detector incorporates a $1.8 - 3.3\text{ }\mu\text{m}$ cold filter to attenuate out-of-band radiation. The detector dewar is mounted on an X - Y - Z translation stage to allow precise detector positioning. A matched EG&G Judson two-stage preamplifier further amplifies the fluorescence signal from the detector.

Because of the long Br* lifetime, even small amounts of molecular fluorescence can interfere with the excited bromine signal. An external bandpass interference filter centered at 2.71 μm with a FWHM bandwidth of 0.03 μm is placed before the InSb sapphire window to isolate the Br* emission from unwanted molecular emissions. Such emission near 2.7 μm had previously been observed in similar studies.^{5, 9}

In a previous AFIT study, Tate used a 2.71 μm interference filter with a 92.6 nm FWHM bandwidth.²⁵ This filter has a passband around 2.71 μm as specified, but also passes wavelengths from approximately 3.7 to 5.3 μm . Figure 3.5 below shows an infrared spectrophotometer scan of the filter from 1.5 to 4.5 μm .

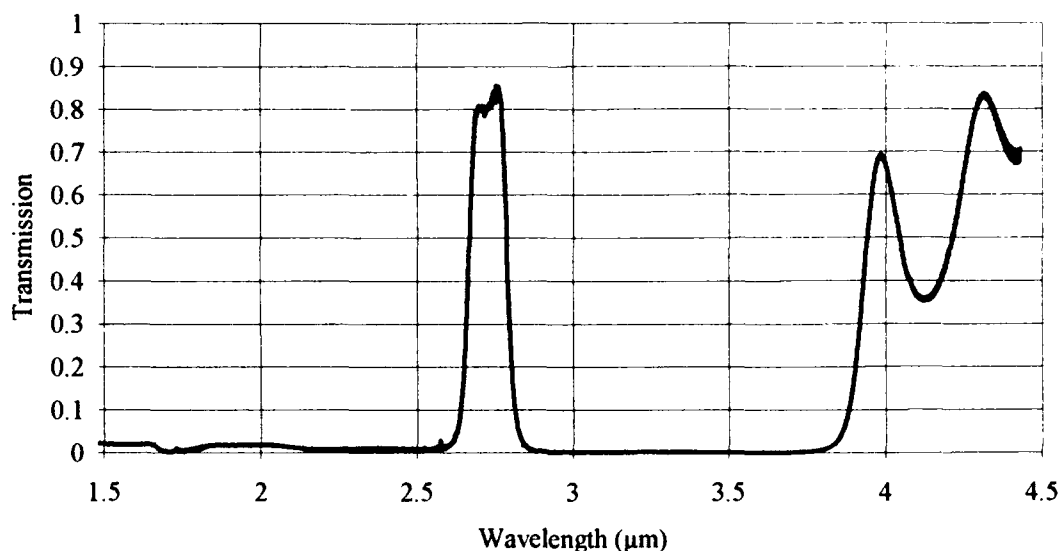


Figure 3.5. Broadband 2.71 μm filter transmission characteristics showing transmission at 4.3 μm .

When Tate performed the CO₂ quenching rate analysis, he was surprised to see an apparent increase in the Br* signal as he added CO₂.²⁵ Tate believed the cause for this signal increase was CO₂ emissions near 2.7 μm that were within the filter passband. Although there may have been some molecular emission near 2.7 μm, this research shows that the majority of the increase in detected intensity is due to 4.3 μm CO₂ emission that passes through the interference filter, nearly unattenuated. Tate had used an InSb detector without the cold filter which readily passed the 4.3 μm radiation.

In order to verify the operation of the narrowband 2.71 μm filter, an infrared spectrophotometer scan was made of the filter. The filter passband is 0.03 μm as specified, and CO₂ quenching studies show no increase in intensity when CO₂ is added. The passband of the narrowband filter was less than that used by Hariri and Wittig in similar Br*/CO₂ studies.⁹

The weak current signal from the detector is amplified by a matched EG&G Judson PA-9 two-stage preamplifier and applied to the input of a lock-in amplifier for signal phase detection of the excited bromine voltage signal against the chopper reference frequency. All functions of the lock-in amplifier are computer controlled via an RS-232 interface.

Data collection is performed by a 386 personal computer (PC) and an eight channel Quinn-Curtis, DAS-8 analog-to-digital (A/D) converter. Metrabyte *TLABLOG* software controlled the data collection which allows 0 to 10 volt analog samples to be collected at user-selected rates. Depending on the buffer gas mixing rate, data are collected at rates from 0.05 to 5 samples per second. The data are stored as ASCII arrays and are analyzed after data collection. Curve fits are performed using *TableCurve* curve fitting software.

During the various phases of the experiment, up to eight channels of analog data are collected: 10 and 100 Torr Baratron pressures, 2.71 μm detector voltage, cell temperature, relative incident laser power, relative 488 nm transmitted laser intensity, and incident and transmitted 409 nm filtered light.

2. Pulsed-Experiment Equipment

The pulsed experimental apparatus is shown in Figure 3.6. The apparatus uses the same reaction cell and gas-handling system as the steady-state experiment. The photolysis source is a Lambda Physik model FL3002E dye laser pumped by an EMG 101 MSC XeCl excimer laser. Coumarin 480 dye provided 7 mJ per pulse at a wavelength of 480 nm in a 25 ns pulse at 25 Hz.

After detection and amplification by the matched InSb detector and amplifier, the Br^* fluorescence waveforms are recorded on a LeCroy model 9450A, 300 MHz digital oscilloscope, and then sent to the personal computer for storage and subsequent analysis. The InSb detector has a one microsecond response time, which is suitable for measuring Br^* pulsed lifetimes.

Because of the weak Br^* fluorescence, the emission intensity observable at the output of the detector amplifier has a low signal-to-noise ratio. Additionally, the excimer laser produces a large electric noise component that further complicates data collection. The Br^* fluorescence signals are arithmetically averaged over 1000 to 3000 laser shots to increase the S/N ratio. To reduce the electrical noise component, an averaged signal with the reaction cell empty is stored in the oscilloscope's memory, and the

averaged data with bromine in the cell is then subtracted from the background signal stored in the oscilloscope memory. Pulsed lifetime fits are made using curve fitting software.

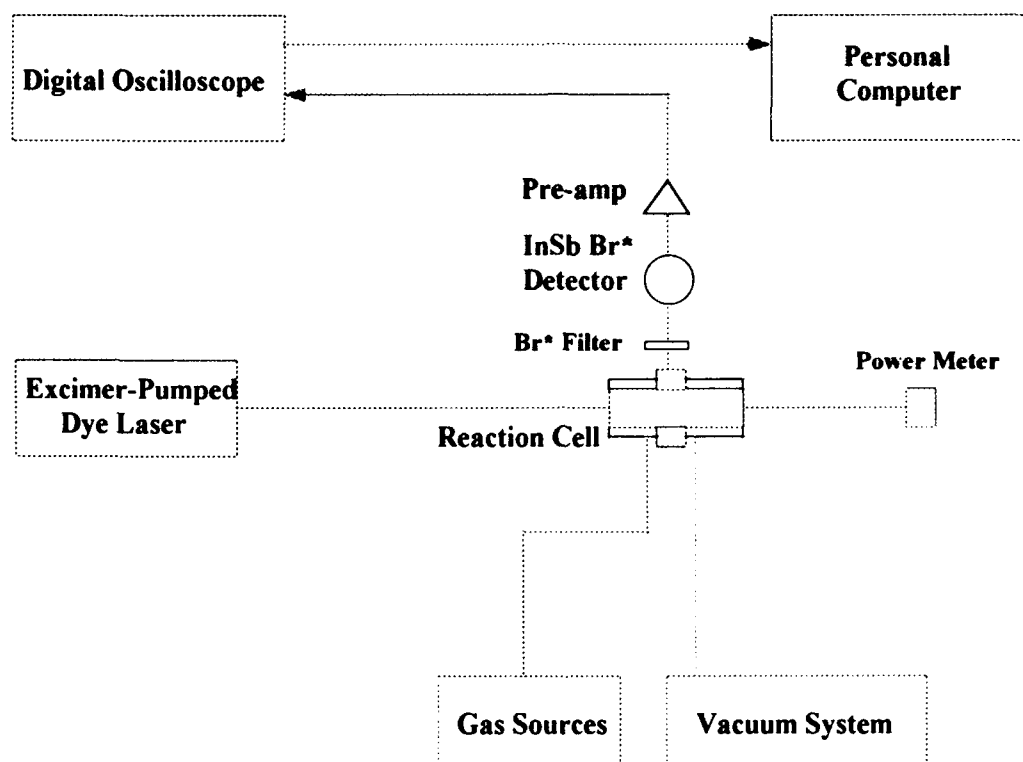


Figure 3.6. Schematic diagram of the pulsed photolysis experimental apparatus.

A typical decay waveform for the Br^* emission is shown in Figure 3.7. The residual noise seen in the waveform is electrical noise and does not average out as more samples are taken. No extreme measures, such as a screen room, were taken to eliminate this electrical noise, and lifetime curve fits are acceptable with the noise present. Typical S/N ratios for the pulsed

fluorescence data are from 10 to 20, compared to S/N ratios of 30 to 70 for the steady-state data.

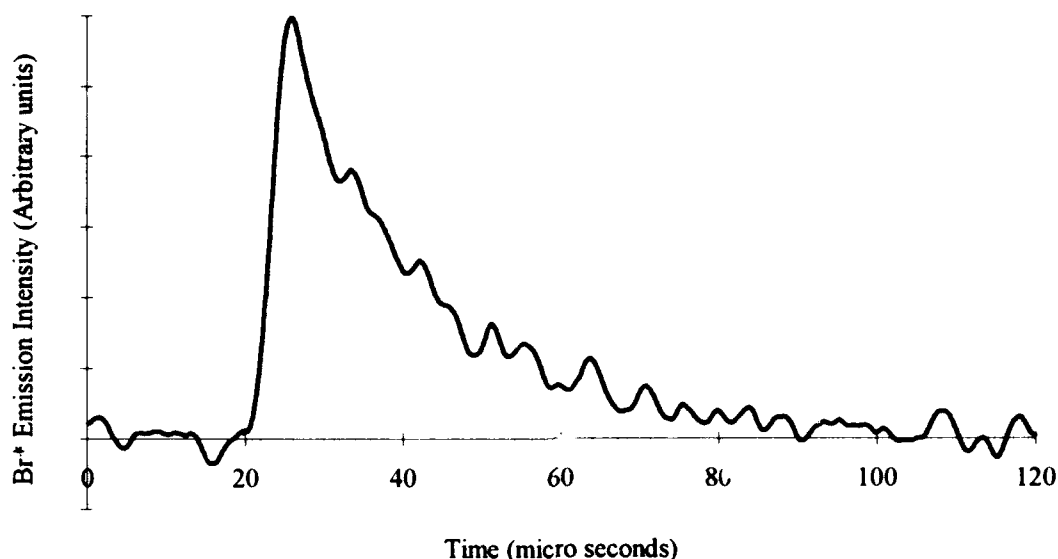


Figure 3.7. Example Br* pulsed fluorescence lifetime data.

3. Cell Pressure-Change Measurement Equipment

The apparatus used to measure changes in cell pressure is similar to the steady-state experimental apparatus. The reaction cell is replaced with one of two glass tubes: cell 1; a 49 cm long, 13/32 inch inner diameter tube and cell 2; a 39 cm long 0.95 inch inner diameter tube.

The cell pressure increases when the molecular bromine is dissociated by the Ar⁺ laser. This change in pressure is small for low bromine concentrations, and results in small voltage changes from the Baratron. The pressure change is also small because only a fraction of the tube volume is excited by the laser. To observe these small pressure changes, the

differential amplifier circuit shown in Figure 3.8 is used to amplify these small changes in voltage.

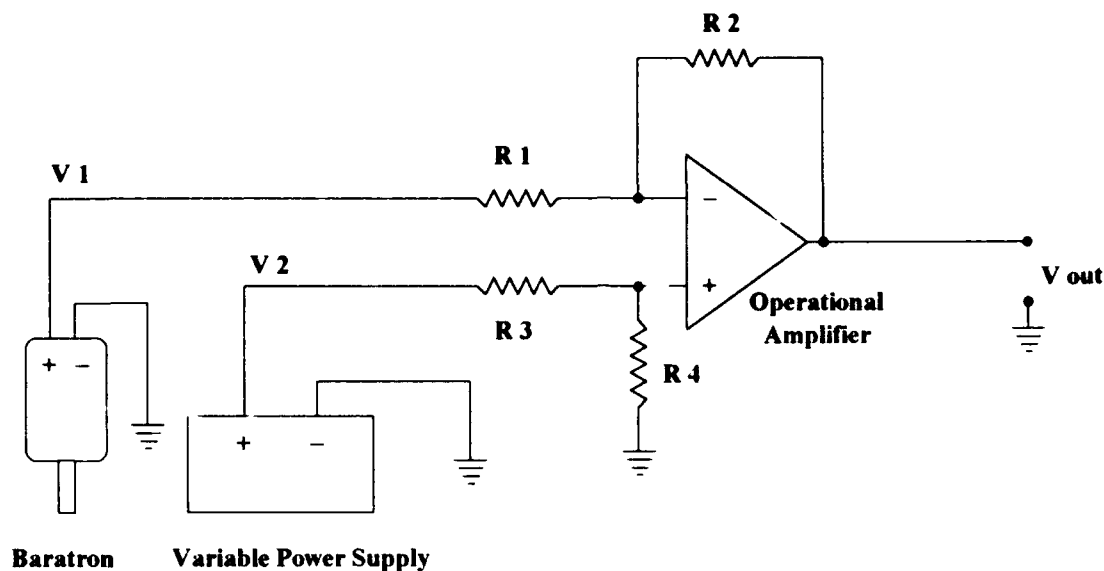


Figure 3.8. Differential amplifier circuit used in pressure change measurement experiments.

The differential amplifier amplifies the difference between the negative and positive inputs of the operational amplifier. To form a differential amplifier, resistor ratios are chosen so that $R2 / R1 = R4 / R3$. With these ratios chosen, the output voltage is

$$V_{out} = \frac{R2}{R1} (V2 - V1) \quad (3.34)$$

For this application, $R2 = R4 = 470 \text{ K}\Omega$, and $R1 = R3 = 47 \text{ K}\Omega$, and the output voltage is ten times the difference between the input voltages, $V1$ and $V2$. By adjusting the variable power supply to a voltage near the Baratron output voltage, pressure changes of 0.5 mTorr are measurable at the

differential amplifier output. By blocking and unblocking the Ar⁺ laser, pressure changes proportional to the atomic bromine concentration are recorded.

D. Results

1. Bromine Absorption Data

To establish a baseline for molecular bromine concentration and purity, 409 nm light is used to measure the bromine cross section for absorption. An example of the filtered white light bromine absorption data is shown in Figure 3.9. The average bromine cross section for absorption at $\lambda = 409$ nm is measured as $\sigma = 6.294 \pm 0.054 \times 10^{-19} \text{ cm}^2$, which agrees favorably with $\sigma = 6.247 \times 10^{-19} \text{ cm}^2$ measured by Seery and Britton.³⁷ The data are very repeatable, and the quoted absorption cross section error is one standard deviation; the cell length is 14.2 ± 0.1 cm. The linearity of the 409 nm absorption data indicates that the bromine purity and Baratron pressure measurements are within acceptable limits.

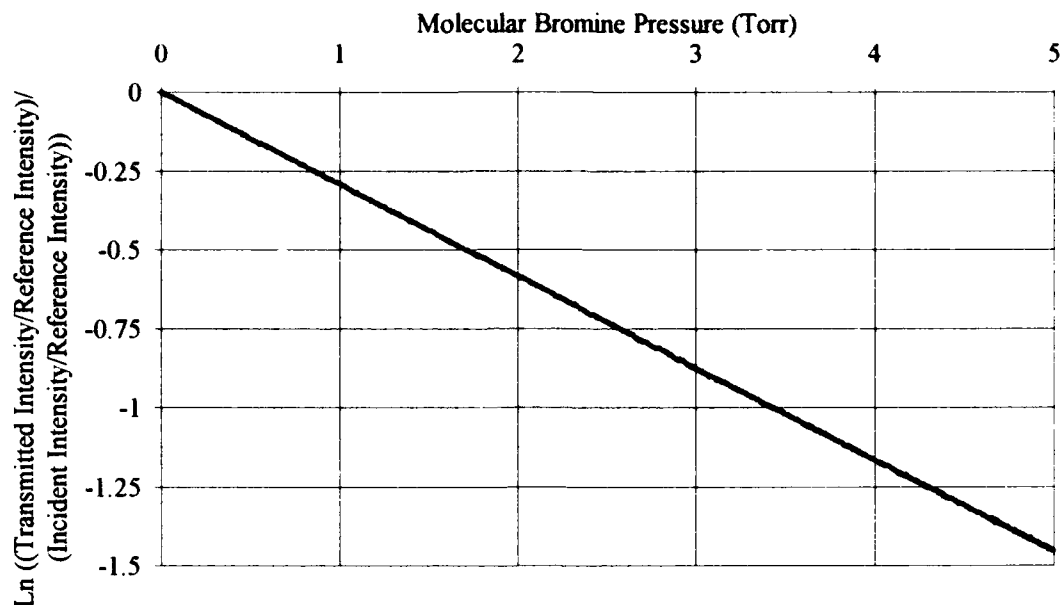


Figure 3.9. Molecular bromine absorption at 409 nm for 0 to 5 Torr bromine and a 14.22 cm path length.

2. Pulsed Lifetime Studies

As is shown in Equation (3.18), the decay rates of the single-exponential pulsed decay waveform, Γ , depend linearly on the Br_2 and buffer gas concentration. With no quenching or buffer gas present, the slope of the Stern-Volmer plot is the quenching rate of molecular bromine on excited atomic bromine, k_{Br_2} .

When calculating the quenching rate for a buffer gas, a fixed amount of bromine is held in the reaction cell, and the buffer gas is added. In this case, the plot abscissa is the buffer gas concentration, and the ordinate remains the Br^* inverse lifetime. With a buffer gas present, the slope of the Stern-Volmer plot is the quenching rate of that gas on excited atomic bromine, k_Q .

The steady-state photolysis experiments provide the buffer gas quenching rate relative to the parent-molecule or Br₂ quenching rate, k_{Br_2} . The Br₂ quenching rate is previously determined to be between 0.47 and $19.0 \times 10^{-12} \text{ cm}^3/\text{molecule-s}$,¹⁻⁵ but the CO₂ deactivation rate is well known; $15.0 \pm 1 \times 10^{-12} \text{ cm}^3/\text{molecule-s}$.^{7, 9, 28}

The goal of the pulsed photolysis experiment is to establish an absolute time base for the steady-state experiments, and since all of the buffer gas quenching rates depend on the value of k_{Br_2} , the Br₂ quenching rate must be well established. If the CO₂ rate is reproducible with this apparatus, then the pulsed experiment can be used to determine the absolute Br₂ rate.

Figure 3.10 provides a Stern-Volmer plot of CO₂ quenching rates for 2 Torr of molecular bromine and 0 to 600 mTorr of CO₂. Each data point represents an exponential fit to the decay of the Br* fluorescence signal. The Br* lifetime decreases as the CO₂ buffer gas concentration, and therefore the associated quenching, is increased. The error bars on the data are one standard deviation for the exponential fit.

Three CO₂ data sets are collected, and the quenching rate coefficients for these sets are shown in Table 3.1. These data yield an average CO₂ quenching rate coefficient of $1.48 \pm 0.18 \times 10^{-11} \text{ cm}^3/\text{molecule-s}$, where the quoted error is one standard deviation. This value is within the error margin of the aforementioned value of $1.5 \pm 0.1 \times 10^{-11} \text{ cm}^3/\text{molecule-s}$. With this well-established value reproduced in this experiment, the Br₂ rate is then determined via the same procedure.

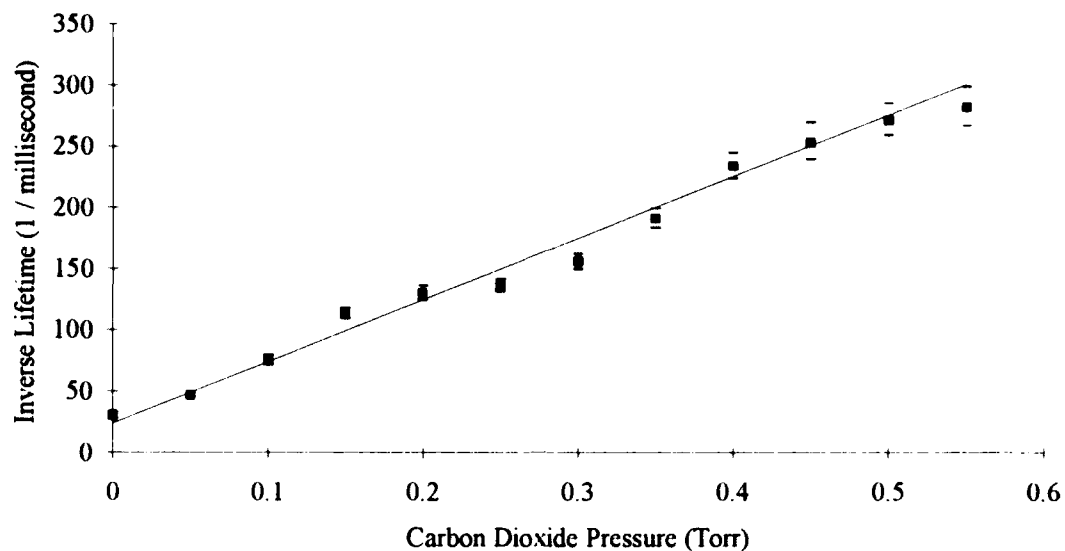


Figure 3.10. Example carbon dioxide quenching of Br* pulsed fluorescence Stern-Volmer plot for 2 Torr bromine and 0 to 600 mTorr CO₂.

Table 3.1

CO₂ Pulsed Quenching Rate Coefficients

CO ₂ Pulsed Data Set	Quenching Rate Coefficient 10 ⁻¹¹ cm ³ /molecule-s
CO ₂ Data Set 1	1.53 ± 0.11
CO ₂ Data Set 2	1.57 ± 0.21
CO ₂ Data Set 3	1.33 ± 0.61

Figure 3.11 below is a Stern-Volmer plot of Br₂ self-quenching rates for 0 to 5 Torr of molecular bromine.

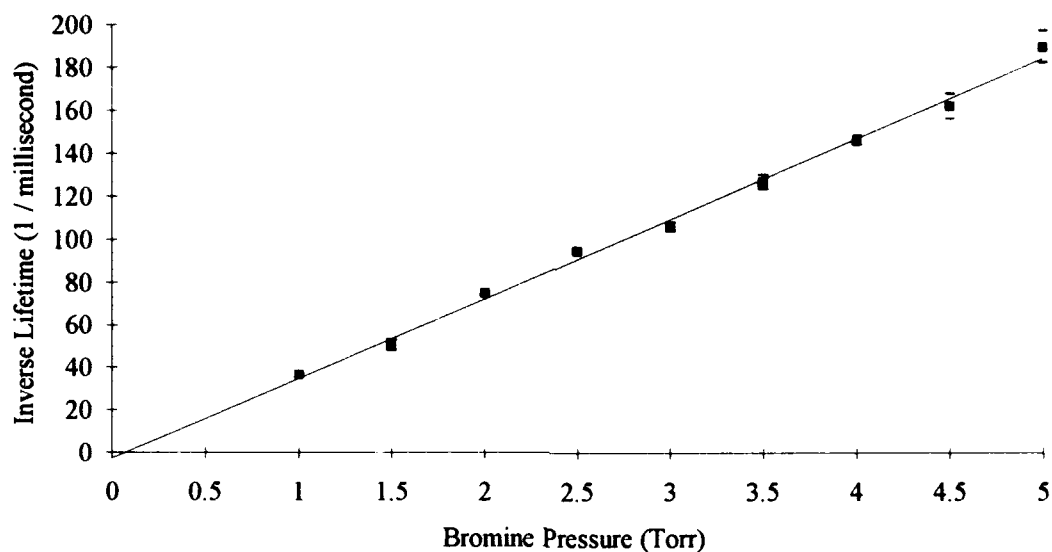


Figure 3.11. Example bromine self-quenching Stern-Volmer plot for 0 to 5 Torr bromine.

Five data sets are taken, and the self-quenching rates for these data are given in Table 3.2.

This Bromine self-quenching data yields an average Br₂ quenching rate coefficient, k_{Br_2} , of $1.24 \pm 0.08 \times 10^{-12} \text{ cm}^3/\text{molecule}\cdot\text{s}$. This value is within experimental error of the value obtained by Hariri, Peterson, and Wittig of $1.20 \pm 0.3 \times 10^{-12} \text{ cm}^3/\text{molecule}\cdot\text{s}$.²

Table 3.2

Br₂ Pulsed Self-Quenching Rate Coefficients

Br* Pulsed Data Set	Quenching Rate Coefficient 10 ⁻¹² cm ³ /molec-s
Br* Data Set 1	1.14 ± 0.07
Br* Data Set 2	1.11 ± 0.14
Br* Data Set 3	1.29 ± 0.08
Br* Data Set 4	1.29 ± 0.11
Br* Data Set 5	1.38 ± 0.10

Now that the bromine self-quenching rate is established, the steady-state photolysis method is used to determine the Br* deactivation rate for 23 additional gases.

3. Steady-State Photolysis Studies

The intensity, I_p , in Equation (3.10) evaluated at the detector viewing volume is reduced through prior absorption by Br₂. The intensity is corrected for this Beer's law absorption by defining an intensity, I_p , reduced from its initial value, I_p^0 , by the exponential absorption term:

$$I_p = I_p^0 \exp(-\sigma l [\text{Br}_2]) \quad (3.35)$$

where

σ = bromine cross section for absorption (cm^2)

l = cell path length traveled by the pump laser prior
to reaching the detector viewing volume (cm)

The absorption coefficient, ϵ , shown in Figure 2.5, is in units of liter $\text{mol}^{-1} \text{cm}^{-1}$, base 10 at room temperature. Equation (3.36) relates the absorption coefficient, ϵ , to the cross section, σ , used in Equation (3.35):

$$\sigma = \frac{\epsilon \ln(10) 10^3}{6.022 \times 10^{23}} \quad (3.36)$$

Figure 3.12 shows the atomic bromine emission intensity both uncorrected and corrected for the molecular bromine absorption. The uncorrected curve shows the decrease in emission intensity at higher bromine pressures due to laser absorption. This laser absorption is accounted for in the corrected curve by multiplying the detected emission by a positive exponential absorption term. The corrected emission signal levels off at pressures above a couple Torr as the increased Br^* production from Br_2 photolysis is balanced by collisional deactivation.

With 7 mJ per pulse at a 25 Hz pulse repetition rate, the pulsed laser produces approximately 175 mW of average power. The Ar^+ CW laser nominally operates at 650 mW of average power. The pulsed waveform signal-to-noise ratios range from 10 to 20, as is shown in Figure 3.7. The steady-state emission signal-to-noise ratios typically range from 30 to 70. The increase in average power over the pulsed system is partially responsible for the improved steady-state signal-to-noise ratios.

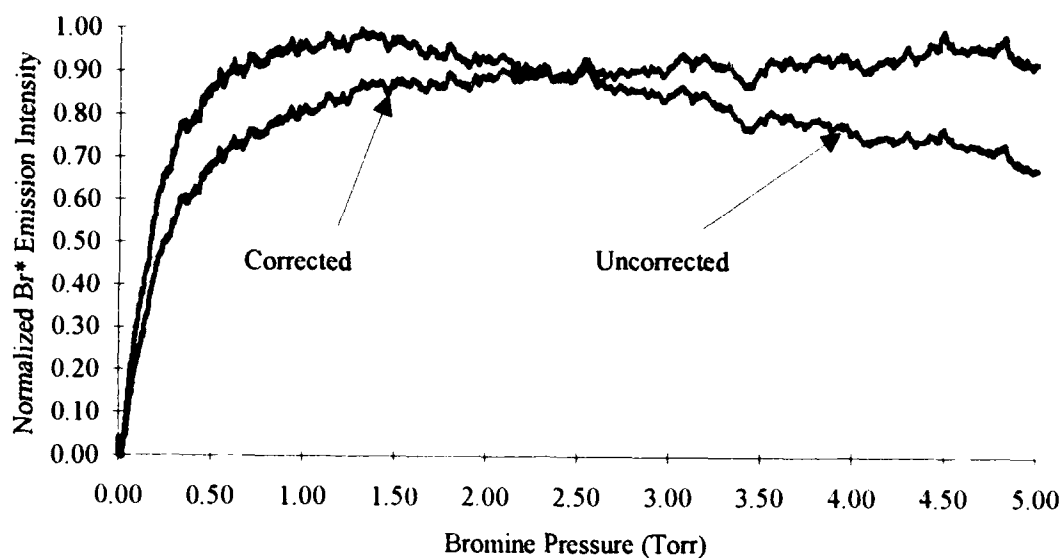


Figure 3.12. Example Br* fluorescence intensity versus molecular bromine pressures from 0 to 5 Torr.

To determine the quenching rate for an added buffer gas, Q, it is necessary to know the value of k_0 , the non-pressure dependent Br* deactivation rate. As shown in Equation (3.37), knowing the bromine self-quenching rate coefficient and the slope-to-intercept ratio determines the value of k_0 :

$$k_0 = \frac{k_{\text{Br}_2}}{\left(\frac{m}{b}\right)} \quad (3.37)$$

The linearity of Figure 3.13 supports the kinetic mechanism of Equation (3.12) and establishes the ratio $k_{\text{Br}_2}/k_0 = 3.33 \pm 0.076$. The value of the ratio is established by making 20 measurements over several different days. The ratio is found to be very repeatable indicating the stability of k_0 .

Using the k_{Br_2} value obtained from the pulsed experiments provides

$$k_0 = 1.20 \pm 0.10 \times 10^4 \text{ second}^{-1}.$$

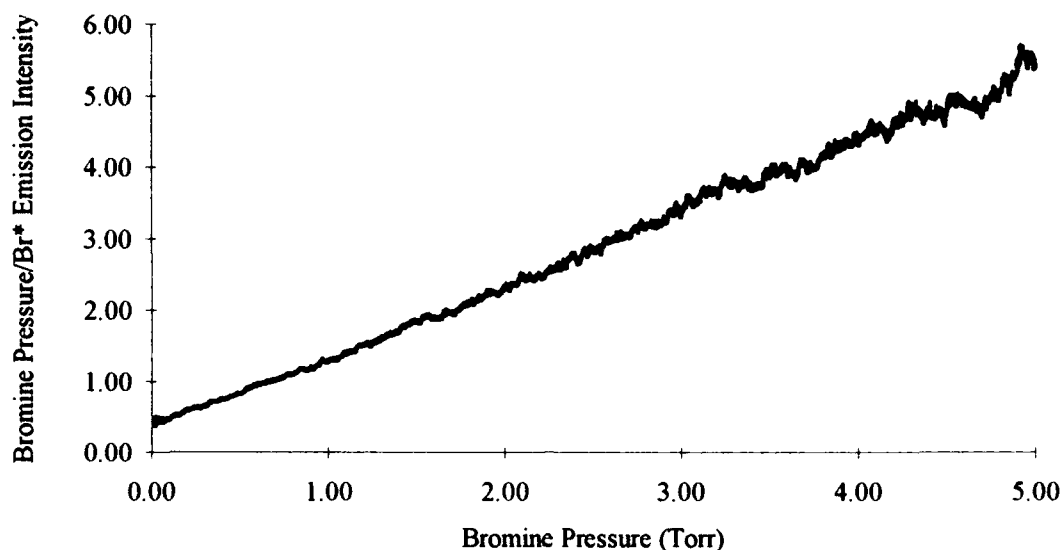


Figure 3.13. Example bromine steady-state self-quenching Stern-Volmer plot for 0 to 5 Torr bromine.

To further validate the steady-state photolysis experimental procedure, CO_2 was added to two Torr of molecular bromine. The average CO_2 quenching rate obtained from five experiments was $13.16 \pm 0.245 \times 10^{-12} \text{ cm}^3/\text{molecule}\cdot\text{s}$. This rate is within the tolerance of previous values, and the steady-state photolysis method is used to determine the spin-orbit relaxation rate for the additional gases.

A typical plot for Br^* quenching by CF_4 is shown in Figure 3.14. The slope of the curve establishes the buffer gas quenching rate relative to the Br_2 quenching rate. Typically, the Br_2 concentration is chosen to be about two Torr, so that the results are relatively insensitive to the value of k_0 . The

quenching rate coefficients, using $k_{\text{Br}_2} = 1.24 \pm 0.08 \times 10^{-12} \text{ cm}^3/\text{molecule}\cdot\text{s}$ are presented in Table 3.3. The absorption diagnostics are used in all experiments to insure the molecular bromine is completely mixed with the buffer gas and that no pre-reaction takes place between the buffer gas and the bromine.

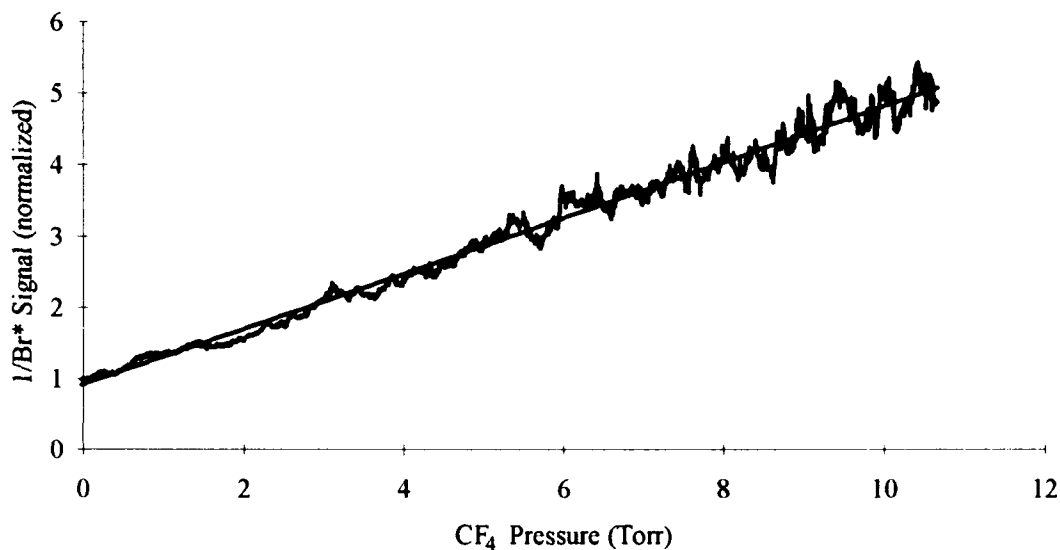


Figure 3.14. Example $\text{CF}_4\text{-Br}^*$ steady-state quenching data showing linear regression fit to CF_4 quenching results.

Table 3.3

Steady-State Experimental Rate Coefficients

Quenching Gas	Quenching Rate 10 ⁻¹² cm ³ /molec-s	Previous Rate 10 ⁻¹² cm ³ /molec-s	References
Ar	0.00595 ± 0.00043	< 0.0002	1
Br ₂	1.24 ± 0.08	19 1.2 ± 0.3 0.99 ± 0.09 0.48 ± 0.05 0.47 ± 0.04	1 2 3 4 5
CF ₄	0.6216 ± 0.0056	0.21	1
CH ₄	2.392 ± 0.047	4.2	1
CO	0.01245 ± 0.00116	0.0073 0.01081 ± 0.00056	1 27
CO ₂	13.16 ± 0.245	15 ± 1	7, 9, 28
COS	1.594 ± 0.051	1.4 ± 0.1	9
D ₂	0.9719 ± 0.0566	5.7 0.68	1 27
H ₂	2.353 ± 0.223	4.7 2.7	1 27
H ₂ S	7.979 ± 1.100		
He	0.01589 ± 0.00275		
HBr	3.475 ± 0.188	1.1 1.4 0.84 ± 0.11	1 16 4
HCl	17.09 ± 0.19	8.6 5.2 ± 0.4	16 4
HI	8.992 ± 0.539		
Kr	0.005864 ± 0.002079		
N ₂	0.01380 ± 0.00650	0.0025	1
Ne	0.01092 ± 0.00291		
NO	2.392 ± 0.100	47 2.0 5.3	1 16 29
NO ₂	0.5289 ± 0.2664		
N ₂ O	2.794 ± 0.213	2.6 ± 0.8 3.1 ± 0.9	7 3
O ₂	0.00332 ± 0.00142	34 0.0015 ^{+ 0.0004} _{- 0.0015}	1 28
SF ₆	0.09043 ± 0.04774		
SO ₂	0.3577 ± 0.0423		
Xe	0.007536 ± 0.00529		

4. Quenching Rate Temperature Dependence

Steady-state temperature experiments were performed to differentiate between the several proposed $E \rightarrow V$ transfer mechanisms: long-range multipolar interactions, short-range repulsive interactions, and nonadiabatic curve crossings. The on-axis molecular bromine absorption cross section for the temperature range 300–425 K is shown in Figure 3.15. The cross section was derived from the Ar^+ laser intensity transmitted through the cell. The data shows no trend with increasing temperature within the data error bounds.

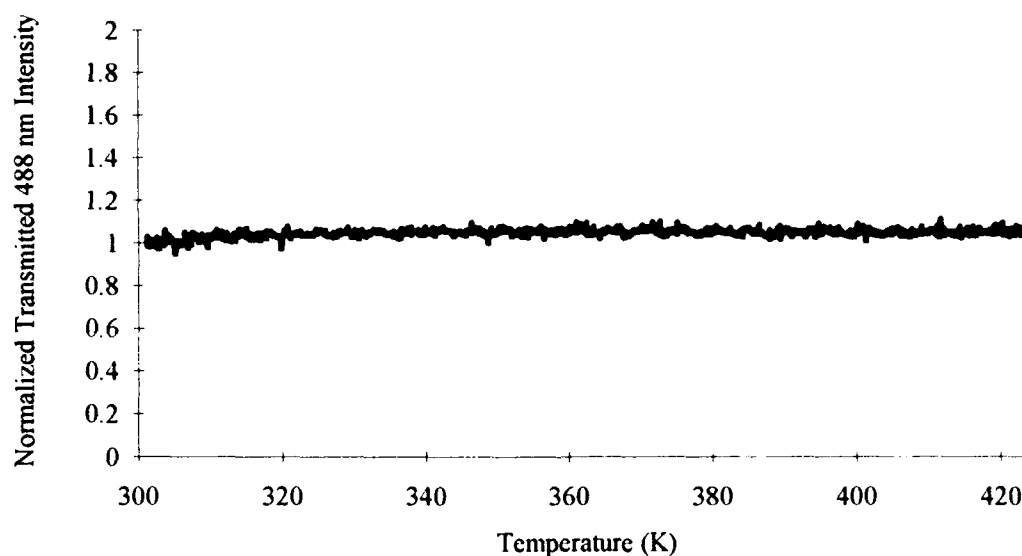


Figure 3.15. Normalized transmitted 488 nm laser intensity for the temperature range 300–425 K showing a near-constant molecular bromine absorption cross section.

Figure 3.16 shows the Br_2 average quenching cross section derived from the $2.71 \mu\text{m}$ Br^* emission intensity for the temperature range 300–420 K which is normalized to the 300 K temperature signal. All

temperature data presented in the present study are converted to average quenching cross sections ($\sigma = k/\bar{v}$) as indicated by Reisler and Wittig to remove the effect of temperature on the molecules' average velocity and therefore the collision frequency.³² Since the molecular bromine absorption is generally unaffected by temperature in this range as shown in Figure 3.15, the Br* creation rate is nearly constant. The Br* emission appears unaffected in this temperature range, and as previously indicated, was found to be only weakly dependent on temperature in the range 300–600 K.³³ This fact makes steady-state buffer gas quenching rate determination possible with this procedure.

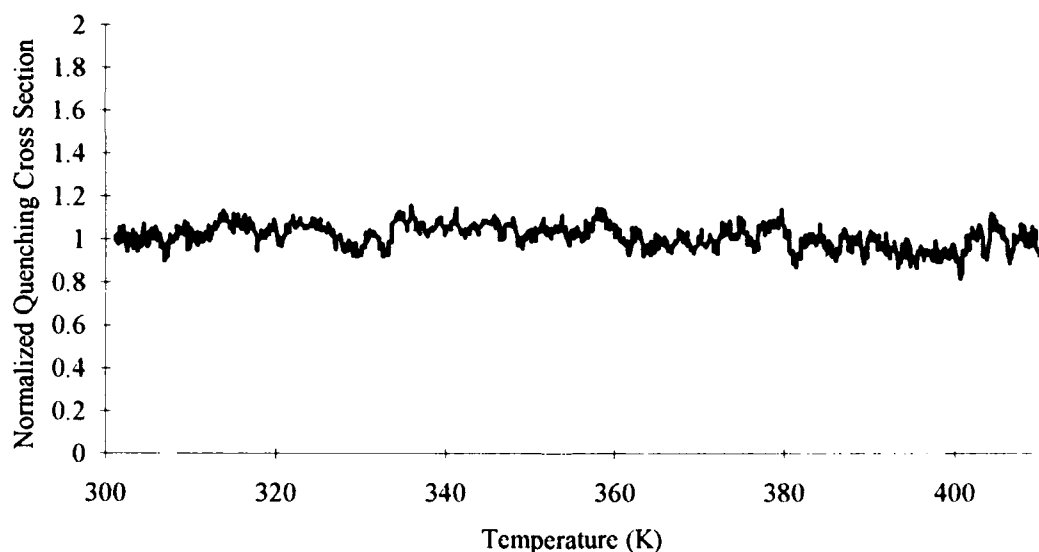


Figure 3.16. Normalized steady-state Br₂ average quenching cross section for the temperature range 300–420 K showing a near constant Br₂ cross section with increasing temperature.

Since much analysis is reported for the CO₂ temperature-dependent quenching rate on Br*, CO₂ is selected as the first quenching species.

Figure 3.17 shows the average quenching cross section for 2 Torr of Br₂ and 550 mTorr of CO₂ for the temperature range 300–410 K. The initial amount of buffer gas added depends on the gas quenching rate, but was chosen so as to be sufficient to reduce the Br* emission to at least one third of initial value. The 488 nm transmitted laser intensity is monitored during the experiment to detect any change in the molecular bromine absorption; none was detected. The data, which represent the average CO₂ quenching cross section, show a decrease in the cross section with increasing temperature. Reisler and Wittig found the CO₂ cross section for deactivating Br* to change from approximately 3.3 to 2.2 Å² as the temperature changed from 300 to 600 K. The change in cross section found in the present analysis is more rapid than that reported by Reisler and Wittig, but the trend is the same.³³ The cross section decreased by approximately 40 percent, while the temperature increased by 37 percent. The decrease in the CO₂ quenching cross section, along with the near resonant energy transfer to the (101) vibrational mode of CO₂, lend support for the long-range attractive quadrupole-dipole term of the interaction potential as a strong candidate for the primary E → V energy transfer mechanism

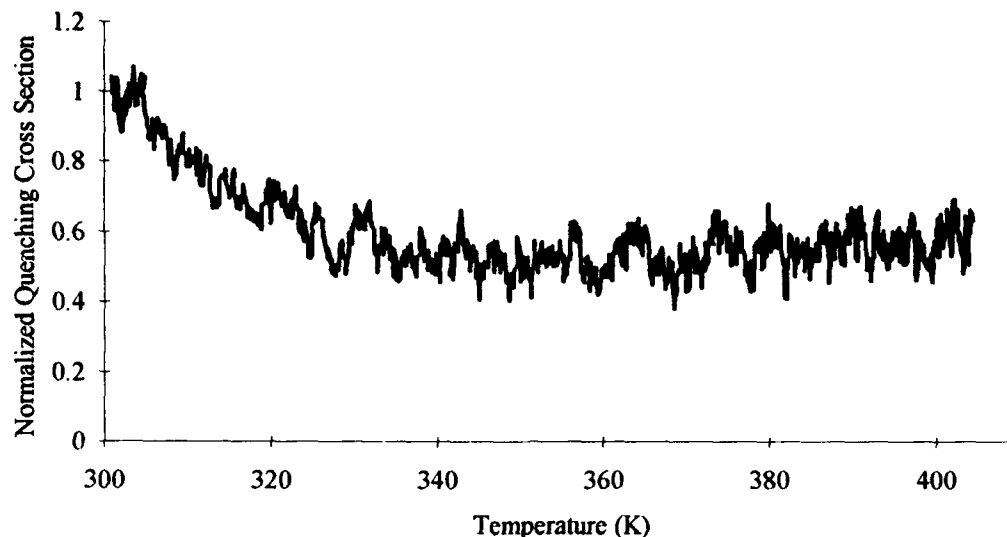


Figure 3.17. Normalized steady-state CO_2 average quenching cross section for the temperature range 300–410 K showing a decrease in the CO_2 cross section with increasing temperature.

The temperature dependence of the steady-state N_2O and HCl quenching cross sections are shown in Figures 3.18 and 3.19 respectively. In both cases, the Br^* emission intensity and hence the cross sections are nearly constant for the temperature range 300–420 K. In previous research, the HCl quenching rate on Br^* was shown to be essentially insensitive to temperature for the range 300–600 K.³² The researchers expected to see a positive temperature dependence based on comparing the $\text{E} \rightarrow \text{V}$ energy transfer process to $\text{V} \rightarrow \text{V}$ energy transfer processes with similar energy defects. It is proposed that for $\text{X}^* + \text{HY}$ systems (where X, Y are halogens), that $\text{E} \rightarrow \text{V}$ transfer proceeds via nonadiabatic transitions between potential surfaces.³² This energy transfer mechanism is also preferred over the long-range multipolar interaction model which does not explain the large HCl quenching rate where the energy transfer is far from resonance.

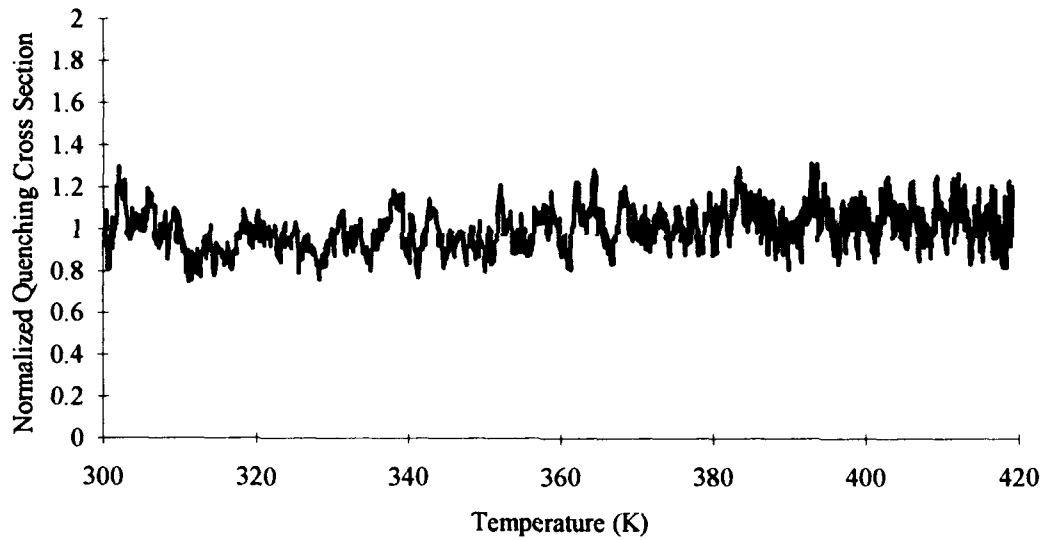


Figure 3.18. Normalized steady-state N_2O average quenching cross section for the temperature range 300–420 K showing a near constant N_2O cross section with increasing temperature.

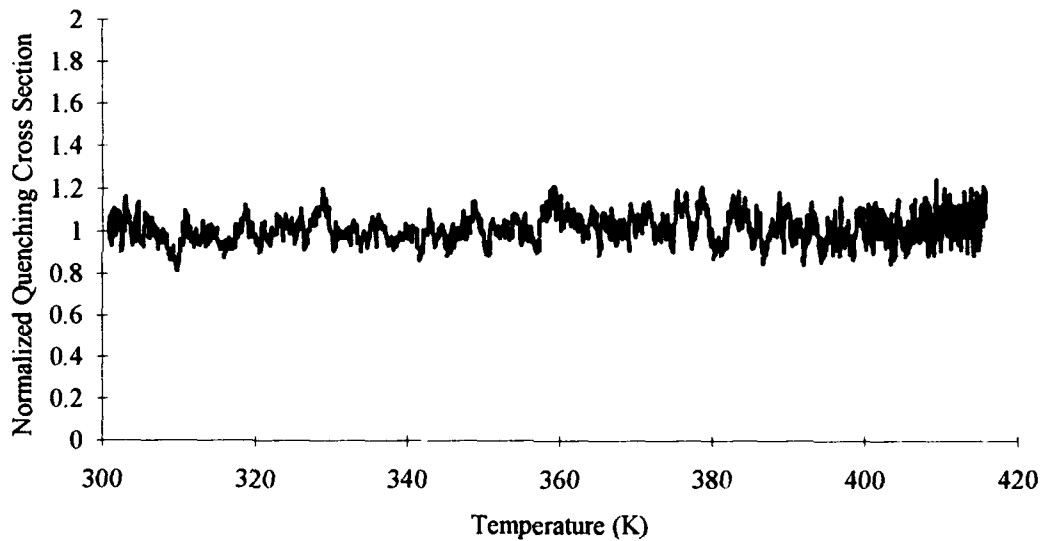


Figure 3.19. Normalized steady-state HCl average quenching cross section for the temperature range 300–420 K showing a near constant HCl cross section with increasing temperature.

The temperature dependence of the steady-state COS and NO quenching cross sections are shown in Figures 3.20 and 3.21 respectively. The COS data show a slight increase in the cross section for the 300–420 K temperature range. A linear fit to the COS temperature data yields a slope of $1.21 \pm 0.058 \times 10^{-3} \text{ K}^{-1}$, or a 0.121 percent change per K. The NO data shows virtually no temperature dependence, and the $E \rightarrow V$ transfer from Br^* to $\text{NO}(v = 2)$ is nearly energy resonant.

Finally, the quenching rate temperature dependence of NO_2 is shown in Figure 3.22. These data show a considerable increase in the NO_2 cross section for deactivation with increasing temperature. The slope of the data is $2.68 \pm 0.0074 \times 10^{-3} \text{ K}^{-1}$, or a 0.268 percent change per K. This slope of the NO_2 data corresponds to an approximate 32 percent increase in the NO_2 cross section as the temperature changes from 300–420 K.

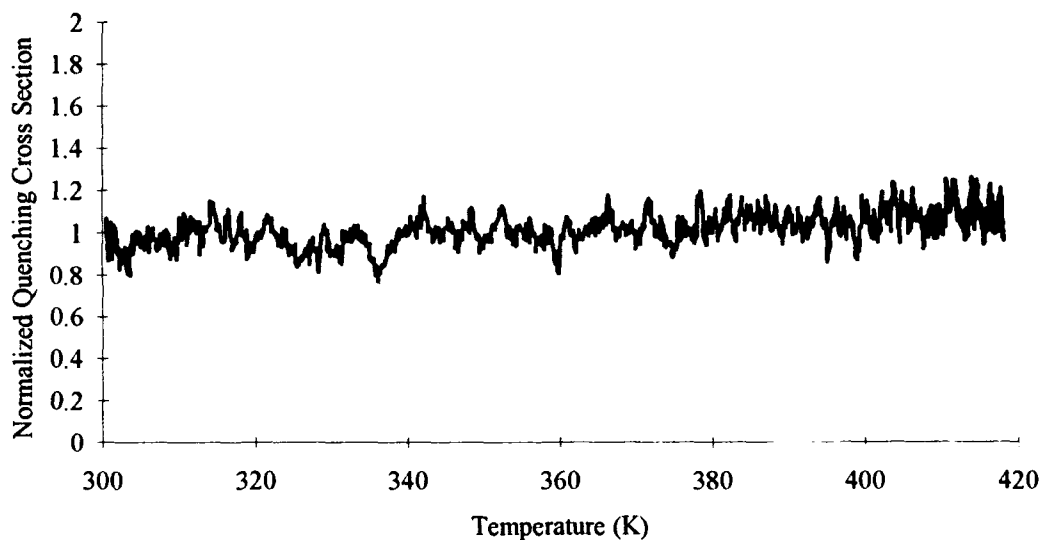


Figure 3.20. Normalized steady-state COS average quenching cross section for the temperature range 300–420 K showing a slight increase in the COS cross section with increasing temperature.

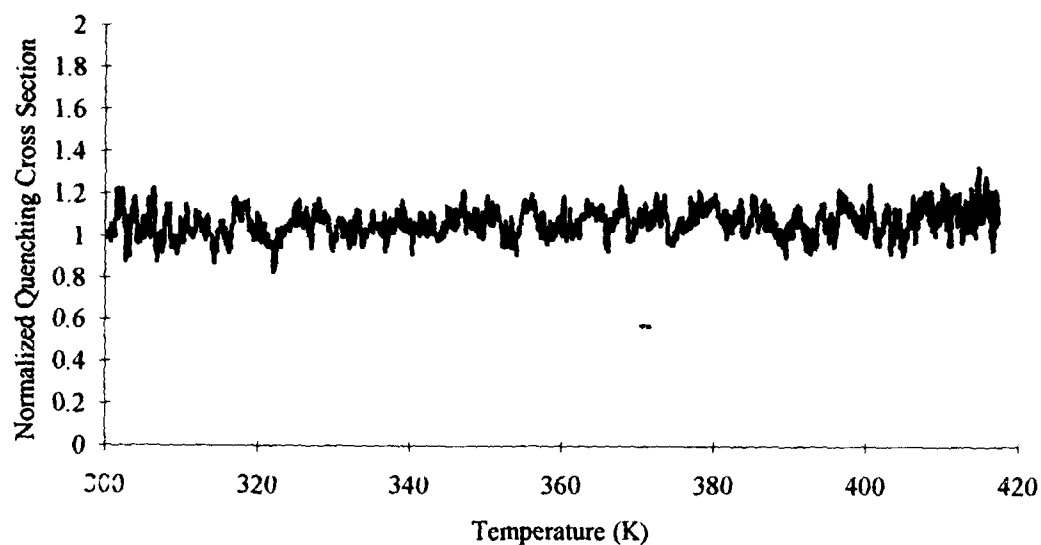


Figure 3.21. Normalized steady-state NO average quenching cross section for the temperature range 300–420 K showing a near constant NO cross section with increasing temperature.

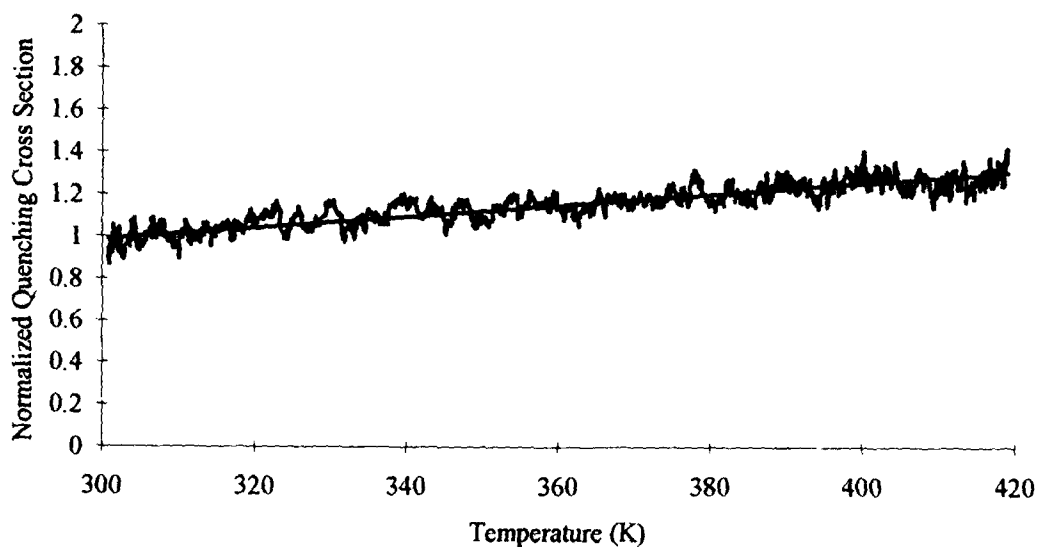


Figure 3.22. Normalized steady-state NO₂ average quenching cross section for the temperature range 300–420 K showing an increase in the NO₂ cross section with increasing temperature.

The following section discusses the results from experiments performed to measure the effects of diffusion, three body and wall rates on the observed quenching rates, and makes estimates of the absolute atomic and molecular bromine concentrations obtained during this research.

5. *Diffusion, Pressure Change, and Concentration Measurements*

a) Diffusion Measurements

To determine how diffusion affects the steady-state quenching rate measurements, 45 Torr of argon was added to 2 Torr of bromine while the Ar^+ laser is transmitted through the reaction cell. As the argon is added to the cell, the transmitted light intensity increases, indicating a decrease in the molecular bromine concentration on the laser axis. This decrease in Br_2 concentration results from a reduction in the wall recombination rate as the argon is added. The added argon interferes with the atomic bromine's ability to transit to the cell walls where recombination occurs, and results in a lower molecular bromine concentration on the laser axis. The results from the experiment are shown in Figure 3.23.

Beer's law is used to determine the reduction of Br_2 caused by the added argon. This Br_2 reduction results in a decrease in the Br^* emission intensity. Using Equation (3.10), the reduction in the Br_2 concentration is equated to an equivalent atomic bromine quenching rate. Five measurements are made and the resulting average decrease in bromine pressure is 3.86 mTorr per Torr of added argon. This reduction in bromine pressure results in a lower emission intensity in Equation (3.10). The amount of reduction depends on the initial molecular bromine concentration. The reduction in emission intensity for an initial two Torr of bromine is equal

to an equivalent atomic bromine quenching rate of $7.45 \pm 0.62 \times 10^{-16}$ $\text{cm}^3/\text{molecule}\cdot\text{s}$. This rate is higher than the previous value of $< 2.0 \times 10^{-16}$ for the argon- Br^* quenching rate.¹ This equivalent quenching rate sets a lower bound on the steady-state quenching rate obtainable from this technique, since the apparent quenching is caused by diffusion. Although small, this rate limit may have implications on the rates for the rare gases, nitrogen, and oxygen.

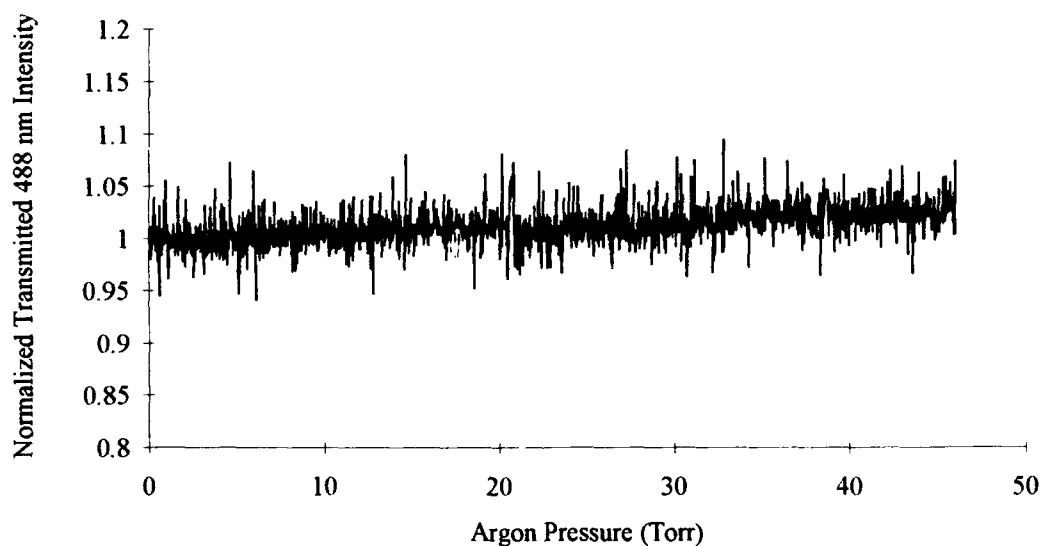


Figure 3.23. Transmitted steady-state 488 nm Ar^+ laser intensity for 45 Torr of argon added to 2 Torr of molecular bromine showing a slight increase in the transmitted 488 nm light which corresponds to a decrease in the molecular bromine concentration caused by diffusion effects.

Diffusion may also affect the Br^* emission intensity. In the absence of a collision partner, the Br^* atom travels approximately 3 mm before emitting. Therefore, some of the atoms may escape from the viewing volume before

emitting, which reduces the emission intensity collected by the detector. The average distance that the Br^* atom travels before a collision is the mean free path, λ . At molecular bromine pressures above about 60 mTorr, the mean free path is less than 1 mm, which constrains the Br^* atom to the viewing volume of the detector. At bromine pressures of 2 Torr, where most of the steady-state measurements are made, $\lambda = 0.03$ mm, strictly limiting the Br^* atom to the viewing volume.

b) Pressure Change Measurements

Diffusion and three body recombination affect the quenching rate measurement over different ranges of pressure. When a buffer gas, Q, is added to a fixed amount of bromine, Equation (3.28) is solved for the bromine concentration:

$$[\text{Br}] = \frac{2 k_p I_p [\text{Br}_2]}{2 k_{3B} [\text{Br}] [\text{Q}] + k_{\text{obs}}} \quad (3.38)$$

where

$$\frac{1}{k_{\text{obs}}} = \frac{1}{k_w} + \frac{[\text{Q}]}{k_{\text{diff}}} \quad (3.39)$$

The solution of Equation (3.38) is

$$[\text{Br}] = \frac{-k_{\text{obs}} \pm \sqrt{(k_{\text{obs}})^2 + 16 k_{3B} [\text{Q}] k_p I_p [\text{Br}_2]}}{4 k_{3B} [\text{Q}]} \quad (3.40)$$

By adding argon to a fixed amount of bromine and noting the pressure change as the laser is cycled on and off, the effects of diffusion and three body recombination can be determined. It is useful to consider three regions of argon concentration.

At low argon concentrations, the wall rate dominates, and the change in bromine concentration is essentially unaffected by the added argon:

$$[\text{Br}] \approx \frac{2 k_p I_p [\text{Br}_2]}{k_w} \quad (3.41)$$

At moderate argon pressures, the diffusive term begins to have an effect, and the bromine concentration curve begins to increase linearly with increasing argon concentration:

$$[\text{Br}] \approx \frac{2 k_p I_p [\text{Br}_2] (k_{\text{diff}} + k_w [\text{Q}])}{k_w k_{\text{diff}}} \quad (3.42)$$

At very high argon concentrations, the three body term dominates, and the bromine concentration curve begins to decrease with added argon:

$$[\text{Br}] \approx \sqrt{\frac{k_p I_p [\text{Br}_2]}{k_{3B} [\text{Q}]}} \quad (3.43)$$

As shown in Equation (3.32), when the laser is cycled on and off, the cell pressure increase is proportional to one-half the on-axis atomic bromine concentration. To determine how dominant the three body recombination mechanism is, 100 Torr of argon is added to 2 Torr of bromine. The resulting change in pressure, ΔP , shown in Figures 3.24 and 3.25, is nearly flat for very low pressures (< 3 Torr), indicating a wall-limited regime. At pressures above 10 Torr, the change in pressure is linear with increasing argon pressure, indicating a diffusion-limited regime. At argon pressures up to 100 Torr, the three body-limited region is not reached.

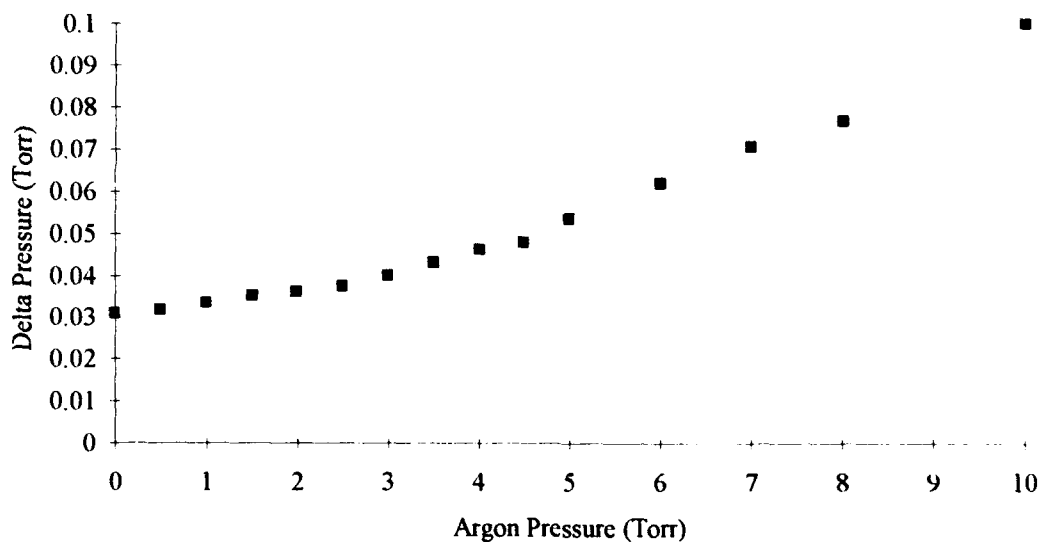


Figure 3.24. Change in cell pressure for 10 Torr of argon added to 2 Torr of molecular bromine.

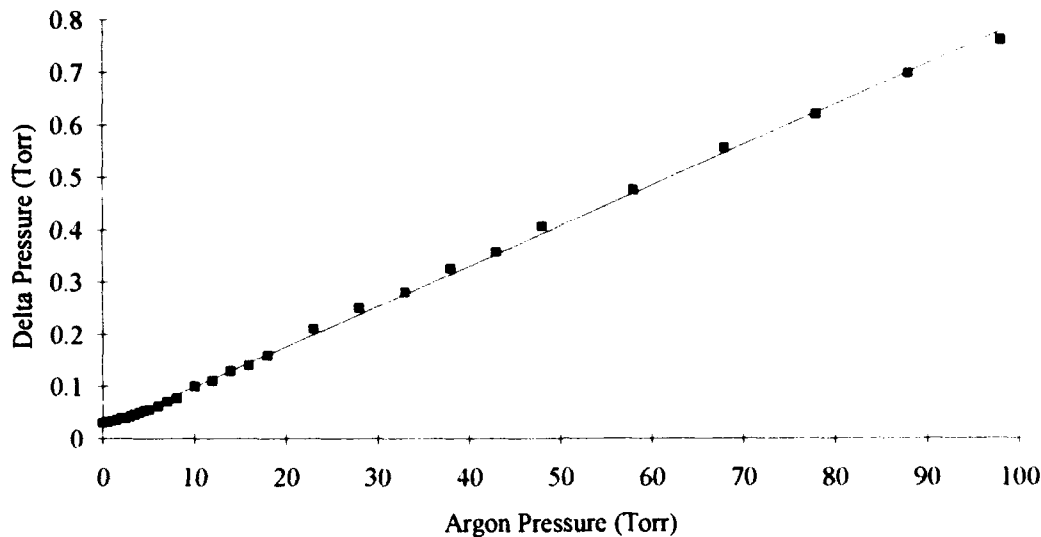


Figure 3.25. Change in cell pressure for 100 Torr of argon added to 2 Torr of molecular bromine.

The linearity of Figure 3.25 suggests the k_{3B} term is unessential to the rate mechanism. Neglecting the k_{3B} term, Equations (3.38) and (3.39) are rewritten to give the atomic bromine concentration:

$$[\text{Br}] = \frac{2 k_p I_p [\text{Br}_2]}{\left(\frac{1}{\frac{1}{k_w} + \frac{[\text{Q}]}{k_{\text{diff}}}} \right)} \quad (3.44)$$

The ΔP data are fit to Equation (3.44), which is expressed in Equation (3.45) as a linear equation in $[\text{Q}]$:

$$\Delta P = \left(\frac{A}{B} + \frac{A}{C} (X) \right) K \quad (3.45)$$

where

$$A = k_p I_p [\text{Br}_2]$$

$$B = k_w$$

$$C = k_{\text{diff}}$$

$$K = 1.65 \times 10^{-18} \text{ (cm}^3 \text{ Torr / molecule)}$$

$$= \frac{\text{ratio of laser beam - to - cell volumes} \left(\frac{0.12}{0.52} \right)^2}{3.22 \times 10^{16} \text{ molecules / cm}^3 \text{ - Torr}}$$

$$X = \text{argon pressure (Torr)}$$

The data in Figure 3.25 are fit to Equation (3.45) with $k_p I_p = 27.7 \text{ sec}^{-1}$ for a laser power of 700 mW. This fit results in $k_w = 131 \text{ sec}^{-1}$ and $k_{\text{diff}} = 382 \text{ Torr sec}^{-1}$. The wall rate coefficient results in a probability of deactivation at the wall, γ , of 3.4×10^{-3} . The probability of deactivation is an upper bound since the wall rate includes a small contribution from a bromine diffusion term. The diffusion rate coefficient results in a diffusion coefficient, D , of $11 \text{ cm}^2/\text{sec}$ at one Torr, for a diffusive parameter of 10. Fick's diffusion coefficient, $D(P)$, at one Torr, calculated from a rigid sphere kinetic theory model is $41 \text{ cm}^2/\text{sec}$, in good agreement with the experimentally-derived value.³⁸

Pressure change measurements are also made with only molecular bromine in the reaction cell. Equation (3.28) is re-written to show the atomic bromine concentration as a function of molecular bromine concentration:

$$[\text{Br}] = \frac{2 k_p I_p [\text{Br}_2]}{2 k_{3B} [\text{Br}] [\text{Br}_2] + k_{\text{obs}}} \quad (3.46)$$

where

$$\frac{1}{k_{\text{obs}}} = \frac{1}{k_w} + \frac{[\text{Br}_2]}{k_{\text{diff}}} \quad (3.47)$$

As in the case when adding argon, the solution to the resulting atomic bromine quadratic equation is given in Equation (3.48):

$$[\text{Br}] = \frac{-k_{\text{obs}} \pm \sqrt{(k_{\text{obs}})^2 + 16 k_{3B} [\text{Br}_2]^2 k_p I_p}}{4 k_{3B} [\text{Br}_2]} \quad (3.48)$$

When adding bromine, as in the case of argon, it is illustrative to consider three regions of molecular bromine concentration.

At low molecular bromine concentrations, the change in atomic bromine concentration is linear with the changing molecular bromine concentration:

$$[\text{Br}] \approx \frac{2 k_p I_p [\text{Br}_2]}{k_w} \quad (3.49)$$

At moderate bromine pressures, the diffusive term begins to have an effect as in the case of added argon, but in this case, the atomic bromine concentration curve increases quadratically with increasing Br_2 concentration:

$$[\text{Br}] \approx \frac{2 k_p I_p [\text{Br}_2]^2}{k_{\text{diff}}} + \frac{2 k_p I_p [\text{Br}_2]}{k_w} \quad (3.50)$$

At very high argon concentrations, again the three body term dominates, and the atomic bromine concentration curve is insensitive to additional added Br_2 :

$$[\text{Br}] \approx \sqrt{\frac{k_p I_p}{k_{3B}}} \quad (3.51)$$

When molecular bromine is added to cell 1, the small diameter cell, the laser intensity at any point along the laser axis is reduced as some light is absorbed on the path to that point. The actual change in pressure is lower than if the light intensity is not reduced. This reduction in intensity is corrected for by letting $I_p = I_0 \exp(-\sigma l [\text{Br}_2])$. Figure 3.26 shows the corrected change in pressure for three Ar^+ laser powers. The resulting changes in cell pressure scale linearly with incident laser power and overlay when normalized for power. This linear change in atomic bromine concentration with laser power further implies that the system is not operating in the high-pressure, three body-dominated region. Equation (3.51) shows that in the

three body-dominated region, the atomic bromine concentration changes with the square root of laser intensity. Figure 3.26 supports operation in the wall-limited regime as the change in pressure is approximately linear with added Br_2 as shown in Equation (3.49).

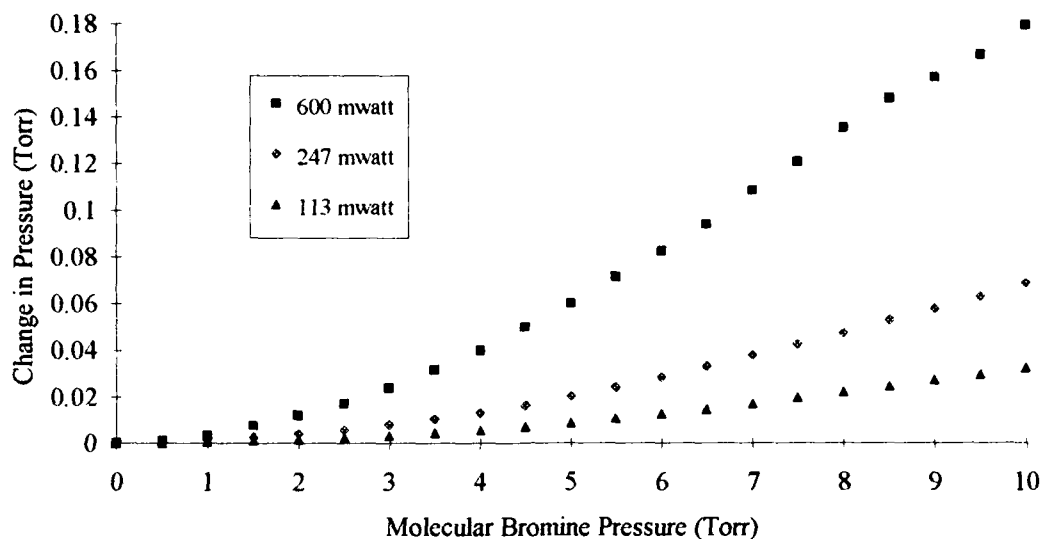


Figure 3.26. Change in cell pressure as measured on the Baratron indicating the atomic bromine concentration for three laser powers in the small radius cell.

Two cell diameters are used to determine how pressure changes and therefore how atomic bromine concentrations scale with cell radii.

Figure 3.27 shows the increased change in pressure for the large cell for an incident power of 600 mW indicating an increase in the atomic bromine concentration.

Exact calculations are not possible due to the cell geometry which tapers from 1/2 to 2 inch glass tubing over part of the cell, but the change in pressure in the large cell is approximately six times the pressure change of

the small cell. The cell radius between the two tubes increases by 4.64, from 0.52 cm to 2.41 cm. An increase in cell radius, r , reduces the wall rate coefficient by a factor of r and reduces the diffusive term by r^2 . This increase in radius causes the data in Figure 3.27 to increase more rapidly as the wall and diffusive terms are reduced thereby reducing the observed rate coefficient. The pressure increase dependent on $r^{1.2}$ shows the effect of the complicated geometry and that operation is in an intermediate regime between wall and diffusion limits.

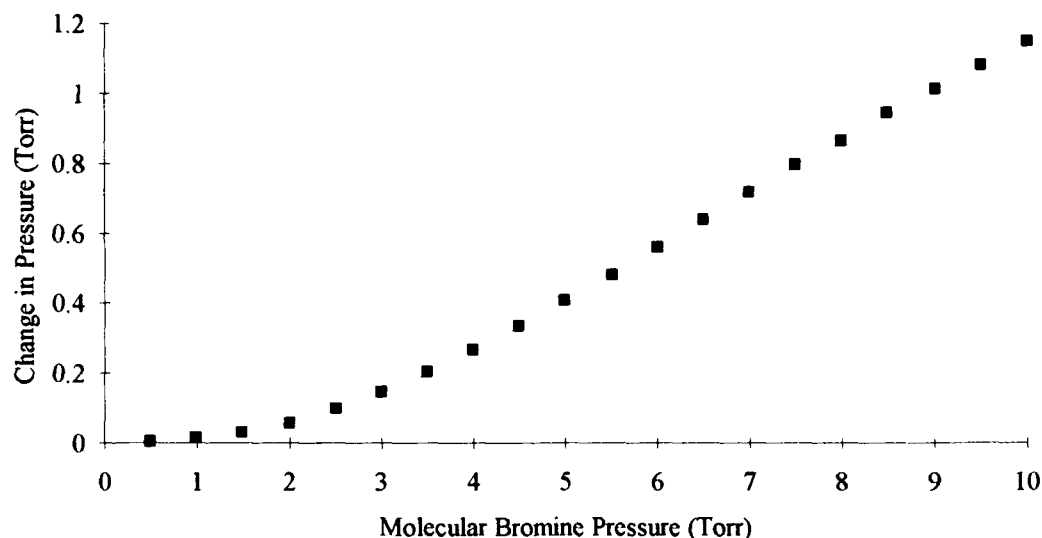


Figure 3.27. Change in atomic bromine concentration for large radius cell measured on the Baratron.

As previously shown, the change in pressure, $\Delta P \propto \frac{1}{2} [\text{Br}]$. By using the transmitted-to-incident power ratio, the absorbed power is calculated. The molecular bromine concentration is then determined from Beer's law. The equivalent pressure change corresponding to each molecular bromine

pressure is then determined. The change in pressure for incident laser powers of 300 and 150 mW are shown in Figure 3.28. These measurements are made in the reaction cell used for rate coefficient determinations. The slope of the pressure change curve is more linear in this figure than in Figures 3.26 or 3.27, which further supports wall-limited operation.

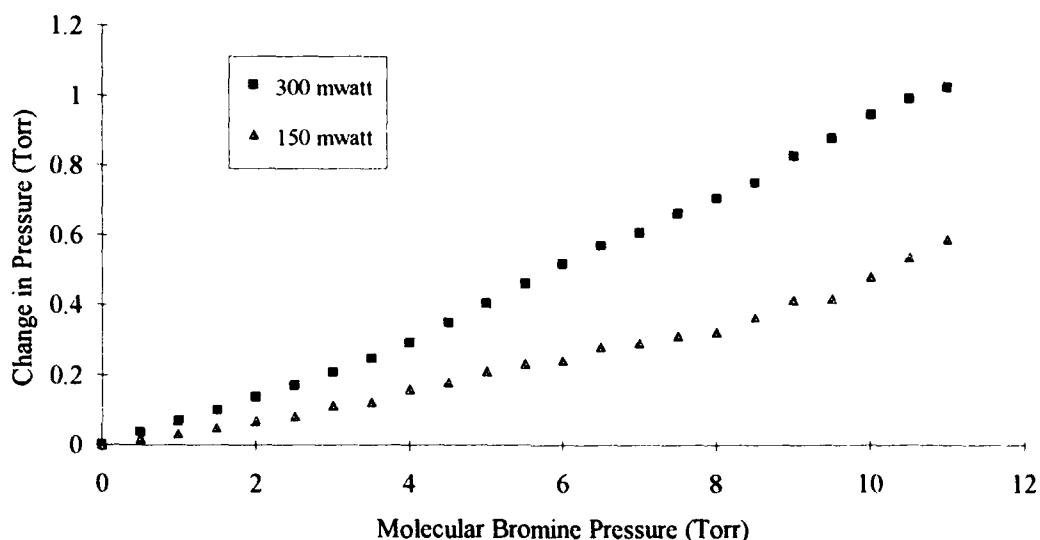


Figure 3.28. Change in atomic bromine concentration for two laser powers calculated from absorbed power.

Figure 3.29 is a curve fit to the 300 mW data shown in the above figure. The data are fit to Equation (3.46), and the fit results in $k_w = 345 \text{ sec}^{-1}$ and $k_{\text{diff}} = 9119 \text{ Torr sec}^{-1}$. The ratio of the diffusive rate to the wall rate is 26.4 at 1 Torr, indicating that the observed rate coefficient is wall limited. These values also indicate that operation is wall limited for molecular bromine pressures less than approximately 10 Torr. All quenching-rate experiments are performed in the wall-limited regime. This data also

explains why no nonlinearity was seen in the steady-state Stern-Volmer data.

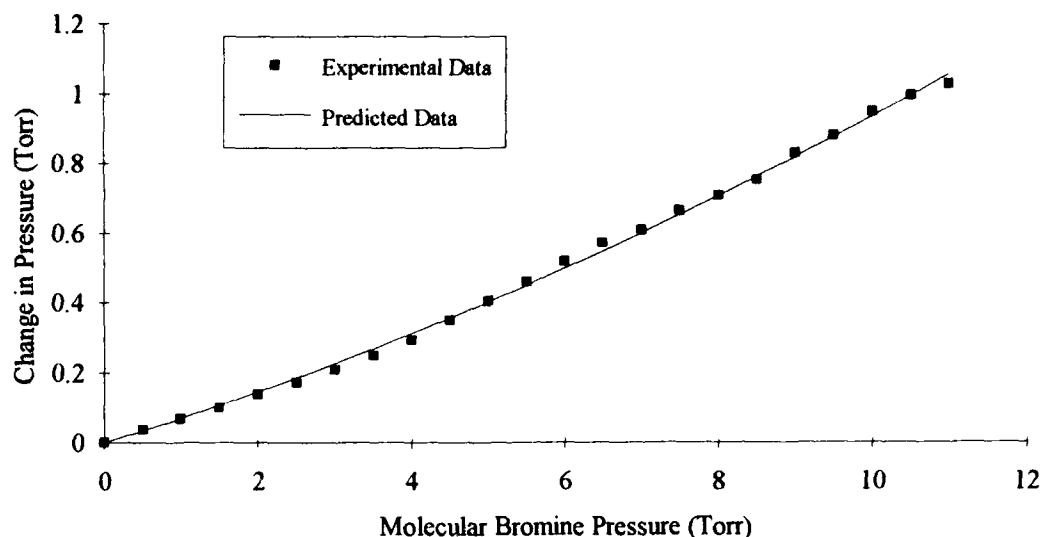


Figure 3.29. Curve fit to the change in atomic bromine concentration calculated from absorbed power showing operation in the wall-limited regime.

c) Atomic and Molecular Bromine Concentration Measurements

The pressure measurement diagnostic is also used to determine the on-axis molecular bromine concentration and hence the concentration of atomic bromine. From the atomic bromine concentration, estimates are made for the $\text{Br}(^2\text{P}_{1/2})$ and $\text{Br}(^2\text{P}_{3/2})$ concentrations.

The Ar^+ laser is propagated through the cell and collected after exiting the cell. The bromine pressure is varied from 0 to 10 Torr. The transmitted 488 nm light intensity is reduced as it is absorbed by the bromine on the

laser axis. Since the laser intensities, cell length, and bromine absorption cross section are known, the molecular bromine concentration can be determined. Figure 3.30 shows the straight-line plot of the natural logarithm of the ratio of transmitted to incident intensities from a data sample where the incident power is 750 mW.

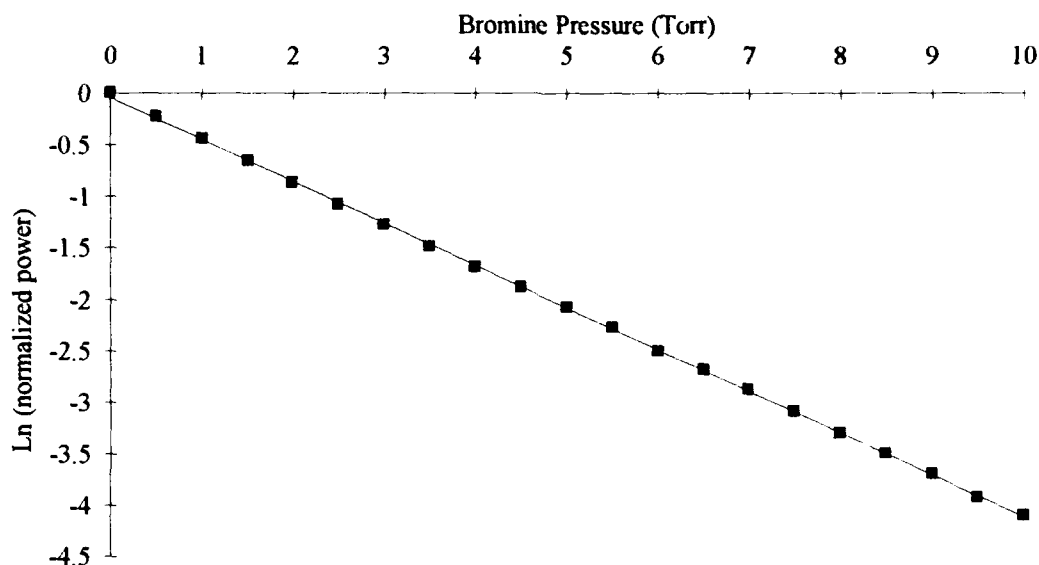


Figure 3.30. On-axis Ar^+ transmitted laser power as a function of molecular bromine pressure to determine the atomic and molecular bromine concentrations for an incident laser power of 750 mW.

A straight line is fit to the data whose slope determines the on-axis molecular bromine concentration which is 86 ± 2 percent of the cell pressure. Therefore the atomic bromine concentration is 14 ± 2 percent. From the ratio of the observed Br^* lifetime, which is $\approx 12 \mu\text{s}$, to the recombination lifetime, the approximate Br^* concentration on the laser axis is 0.4 percent of the cell pressure. The quenching rate determined from the steady-state experiments is not very sensitive to small changes in the molecular bromine

concentration. For these reasons, no corrections are made to the steady-state bromine quenching rate due to the reduction in the molecular bromine concentration.

The pressure measurement diagnostic can also be used in a different way to calculate the atomic bromine concentration. As above in the pressure calculation, from the absorbed power, Beer's law is used to calculate the amount of atomic bromine as a function of molecular bromine pressure. By dividing the atomic bromine concentration at each pressure by the molecular bromine concentration, the percent of atomic bromine as a function of molecular bromine pressure is found. The percent of atomic bromine is shown in Figure 3.31 for incident laser powers of 300 and 150 mW. The photodissociation of molecular bromine and the corresponding creation of atomic bromine also scale linearly with power as seen above.

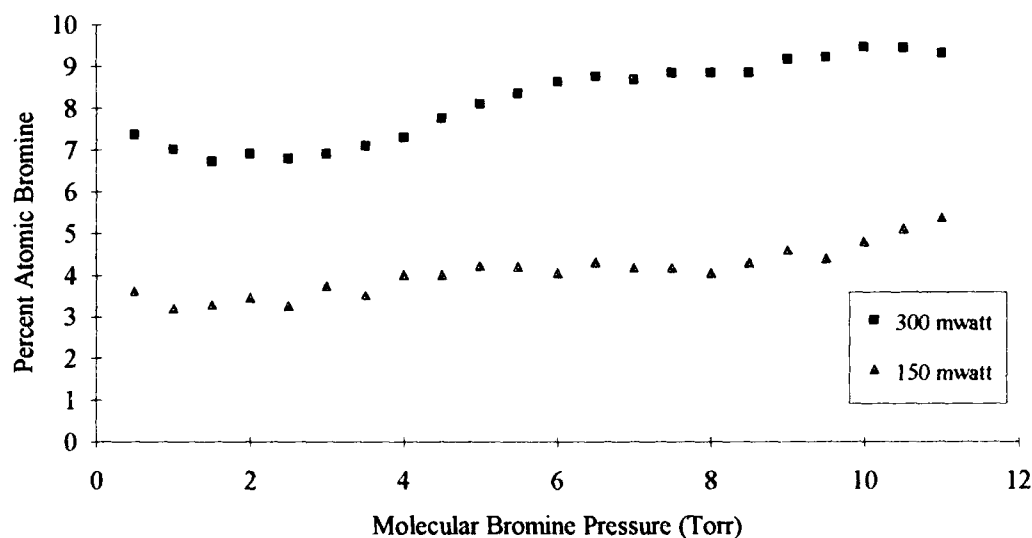


Figure 3.31. Percent of atomic bromine for 300 and 150 mW laser powers calculated from absorbed power.

E. Discussion

1. Overview

In general, the current results agree favorably with the most recently reported rate coefficients for atomic bromine quenching. The quenching rates for rare gas, nitrogen, and oxygen quenching partners are very low, and their measurement is limited by the diffusion rate. The current oxygen rate coefficient is consistent with the slow rate recently reported,²⁸ and apparently the faster rate for oxygen reported in the early 1970's is in error.¹

Several theoretical models have been proposed to understand the possible mechanisms responsible for $E \rightarrow V$ transfer from Br^* such as quantum-mechanical calculations, long-range attractive forces, and curve crossing mechanisms.¹⁶

The quantum-mechanical model seeks to understand $E \rightarrow V$ transfer by performing rigorous quantum-mechanical trajectory calculations on each system of interest. Such an approach seeks to obtain exact results for an assumed interaction potential, but collinear geometries and other approximations that must be made to solve the problems of interest reduce the accuracy of the results.

In general, the theory predicts that the magnitude of the quenching rate coefficient for a buffer gas is a sensitive function of energy defect, ΔE and change in vibrational quanta of the quenching species, ΔV .¹⁶ The energy defect is the difference between the 3685 cm^{-1} excited bromine energy and the energy of the nearest vibrational level of the quenching partner. This energy defect is the energy that must be taken up by rotation and translation during the deactivation. The change in vibrational quanta of the quenching

species also appears important to the magnitude of the quenching rate. Molecules in which the vibrational quantum numbers change by two consistently have lower quenching rates than those in which the vibrational quantum numbers change by only one. Because this theory does not contain any attractive contribution to the atom-molecule potential, it suggests that attractive forces do not greatly affect the value of the quenching rate coefficient.

The second model, long-range attractive forces, is based on the idea that long-range attractive forces couple the electronic and vibrational degrees of freedom; similar to the $V \rightarrow V$ transfer theory developed by Sharma and Brau.¹⁶ Perturbation theory is used to determine the probability of the $E \rightarrow V$ transfer. The theory, which uses quadrupole-quadrupole coupling, predicts an exponential falloff in the quenching rate with ΔE , and a rapid decrease in the rate with ΔV . Improvements in the initial theory developed by Ewing³⁹ show that the long-range attractive force approximation more correctly predicts the quenching rate coefficient when ΔE is small. That is, this theory does not work well for large deviations from resonance where it is believed that short-range coupling might be involved. It is of interest that the long-range attractive force mechanism predicts a quenching rate temperature dependence of $1/T$.

The third theoretical model is based on the idea that $E \rightarrow V$ transfer involves a curve crossing. It is believed that the energy transfer of the Br^* atom takes place when the repulsive part of the ground state curve cross the excited state curve, thereby deactivating the atom and exciting the quenching partner.¹⁶ This nonadiabatic transition can be calculated using the Landau-Zener curve-crossing formula. This theory also predicts that the

quenching rate decreases with the energy defect when ΔE is small and a rapid decrease in quenching rate with increases in ΔV . Finally, the theory predicts an approximate $T^{-1/2}$ quenching rate temperature dependence.

In summary, all three $E \rightarrow V$ transfer theories predict a strong dependence of the $E \rightarrow V$ quenching rate on ΔE and ΔV . The main difference is in the quantum-mechanical approach which includes no attractive forces and the long-range theory which is entirely based on the attractive potential. Appendix D provides more details of the three theoretical mechanisms.

2. *Data Correlation*

By plotting the buffer gas quenching rates from the present study versus the energy defect in Figure 3.32, a correlation is seen. The trend of decreasing quenching rate coefficient for increasing energy defect is clear.

The energy defect is calculated for energy transfer to $\text{CO}_2(101)$, $\text{H}_2\text{S}(110)$, $\text{NO}(v = 2)$, $\text{N}_2\text{O}(101)$, and $\text{NO}_2(210)$, which are the states most energy resonant with Br^* . Energy transfer from Br^* to CO_2 has been much studied. The measurement of the total quenching rate is very repeatable, and it has been shown that 40 percent of the energy transferred excites the v_3 symmetric stretching mode. Laser experiments confirm that the (101) vibrational level receives the most Br^* energy. The current experiments verify the previous data, with the negative quenching rate temperature dependence and small ΔE supporting the long-range forces $E \rightarrow V$ transfer mechanism.

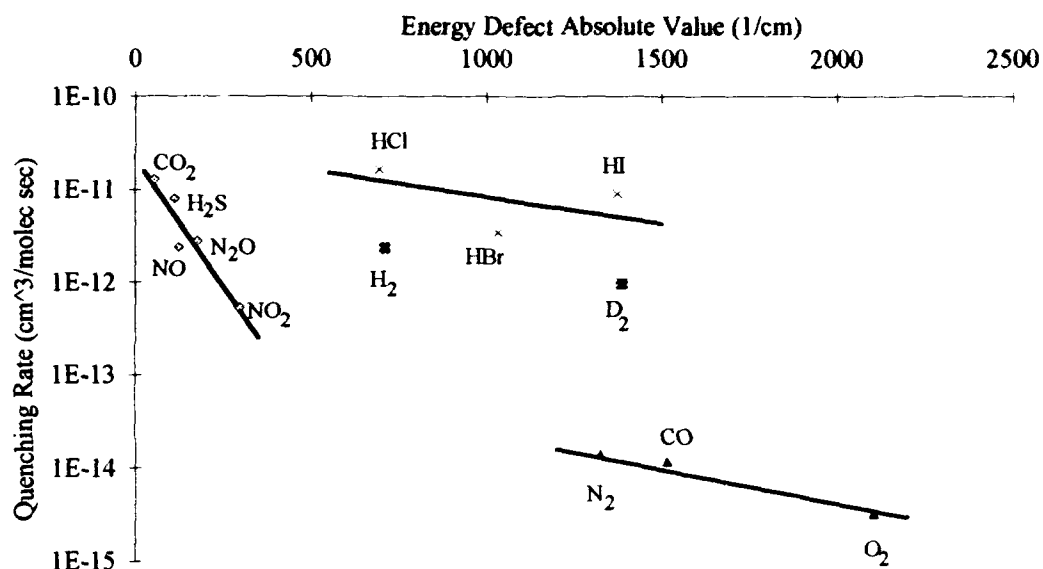


Figure 3.32. Buffer gas quenching rate versus energy defect showing correlation of increasing quenching rate with decreasing energy defect. Linear regressions are shown to identify trends in the data.

The trend with ΔE continues for H₂S, NO, N₂O, and NO₂. No temperature dependence is seen in the NO or N₂O quenching rate, but a positive dependence is seen for NO₂ which makes the long range forces and curve crossing mechanisms unlikely. Wight considered the $E \rightarrow V$ transfer mechanisms for Br* and NO, and he found the long-range interaction between Br* and NO to be unlikely.²⁹ The weak transition moments of Br* and NO make a long-range resonant mechanism unlikely; also no temperature dependence is seen in the present data. Curve crossing mechanisms are unlikely due to the selectivity in producing NO($v = 2$), which is the resonant channel; 84 percent of the $E \rightarrow V$ transfer collisions excite the

$v = 2$ level.²⁹ Also, the ground-state interaction of $\text{Br} + \text{NO}$ is attractive, as evidenced by the stability of nitrosyl bromide.

The most likely mechanism is a resonant interaction of electronic and vibrational degrees of freedom which could be analyzed using transition probabilities and product vibrational-state distributions. The quenching rate temperature invariance also supports this mechanism. The possible formation of BrNO as an intermediate state complicates the theoretical analysis, and more work is needed to understand the exact $\text{Br} + \text{NO}$ energy transfer mechanisms.

The H_2 and D_2 quenching rate energy defect dependence follows the proper trend for all three theoretical mechanisms. Zimmerman and George expressed the potential interaction of Br^* and H_2 , HD , and D_2 using two adiabatic potential surfaces correlating to $\text{Br}(^2\text{P}_{1/2})$ and $\text{Br}(^2\text{P}_{3/2})$ and nonadiabatic coupling terms.⁴⁰ Rigorous quantum mechanical calculations were carried out for collinear collisions, and quenching cross sections were predicted. Grimley and Houston found the same result qualitatively, but believed that D_2 was not dominated by an $\text{E} \rightarrow \text{V}$ channel.²⁷

The series HCl , HBr , and HI does not exactly follow the energy defect trend, as shown in Figure 3.32. Although a previous HI quenching rate coefficient on Br^* is not available, the HI quenching rate for I^* has a larger rate coefficient than expected.¹⁶ This observation of a larger HI quenching rate may also be seen here considering the similarity in Br^* and I^* rate trends,¹⁶ and if so, it might help explain the unexpectedly high HI quenching rate coefficient.

The entire HX series have Br^* quenching rates that are large relative to their energy defects supporting curve crossing mechanisms. But a very

high percentage of the quenching collisions excite specific vibrational states which supports long-range interactions. The very small temperature dependence of the HCl quenching rate was seen by Reisler and Wittig, and the same trend with temperature is seen in the present data.³² The authors believed that because of the aforementioned reasons, curve crossing rather than long-range attractive interactions are responsible for the energy exchange. The $\text{Br}^* + \text{HX}$ experiments clearly show that $\text{E} \rightarrow \text{V}$ transfer is important even when electronic and vibrational quanta are far from resonance. It seems likely that there are a combination of $\text{E} \rightarrow \text{V}$ mechanisms responsible for these conflicting results.

The quenching rate trend with energy defect for O_2 , CO, and N_2 ($v = 1$ states) is very clear from Figure 3.32. Another notable point of these data is their low quenching rate on Br^* and relatively high ΔE . As mentioned above, the O_2 rate had previously been reported as a much larger value, but the most recent value more closely agrees with the current work.²⁸ The O_2 quenching of Br^* is believed to be explained by curve-crossing theory. Since there are no electronic or vibrational states of oxygen that are nearly-resonant with Br^* , all theoretical models predict a very small quenching rate coefficient. Long-range potential theory, however, does not predict well for large values of ΔE , as is the case here. The energy defect for the relaxation of Br^* and subsequent excitation of one quanta of O_2 is approximately 2100 cm^{-1} . Extrapolating the observed ΔE dependence of the quenching of Br^* by other molecules would predict an oxygen quenching rate coefficient of approximately $10^{-14} \text{ cm}^3/\text{molecule}\cdot\text{s}$.²⁸ The rate obtained in the present study although slightly higher than that obtained by Taatjes, more closely matches the aforementioned prediction.

The quenching rates for the remaining buffer gases are near previously reported values. As previously mentioned, the rate measurements for the rare gases are limited due to diffusion, and the rates reported are an upper bound of the actual quenching rate coefficients. It is of interest to note that Kushawaha found the inert gases to quench N_2O in much the same order as is reported in this research; helium has the largest quenching rate followed by Ar, Ne, Xe, and Kr.³

F. Conclusion

The steady-state photolysis techniques employed in this research offer a rapid means of measuring relative rate coefficients. By anchoring these relative rates with well-known rates from pulsed photolysis experiments, an extensive data base for $\text{Br}(^2\text{P}_{1/2})$ quenching has been produced. These results provide an opportunity for quantitatively assessing the efficiency of an infrared laser candidate using excited atomic bromine as the energy carrier. Additionally, three possible theoretical models for electronic-to-vibrational energy transfer are discussed in light of the experimental results.

IV. Laser Prototype Demonstration

A. Introduction

One of the purposes of the pulsed and steady-state photolysis experiments is to determine those molecules that possess the properties desired for an acceptor molecule in an $E \rightarrow V$ energy transfer laser. This chapter discusses the laser prototype demonstration experiments that led to the observation of stimulated emission and lasing of Br^* , CO_2 , and NO following pulsed photolysis of IBr by a doubled Nd:YAG pump laser operating at 532 nm.

The first section provides the necessary molecular laser background theory. The next two sections present the laser demonstration experiment and the results obtained from the experiment. The final two sections are a discussion of the results from the experiment and their conclusions.

B. Background Theory

1. Candidate Laser Species Analysis

When considering an acceptor molecular species for an $E \rightarrow V$ energy transfer laser, several attributes are desired. Even though not all of the conditions for maximum $E \rightarrow V$ energy transfer are well understood, it is known that energy resonance plays a critical role in this type of energy transfer. Molecules with near-resonant energy levels with Br^* have high fractions of $E \rightarrow V$ energy transfer. For this reason, molecules with

vibrational energy levels near 3685 cm^{-1} are desired. As is usually the case with near-resonant molecules, the candidate laser gas should have a sufficient excited bromine spin-orbit quenching rate to allow for maximum energy transfer to the acceptor species. Transfer to a vibrational level above $v = 1$ is desired so relative and not absolute population inversion is required. For example, by transferring energy into $v = 2$ and subsequently lasing from $v = 2 - 1$, the number of molecules in the upper vibrational level does not need to be greater than the number in the ground vibrational level.

After the energy is transferred to the acceptor molecule's vibrational modes, a favorable stimulated emission cross section is required to allow lasing to occur. The candidate should not be homonuclear due to dipole moment considerations. The candidate species may be a triatomic or greater molecule, but diatomic molecules are preferred because their partition functions do not allow the energy transferred from the excited bromine atoms to divide into as many modes. Finally, the selected candidate should lase at a frequency desirable from an operational point of view.

A partial list of infrared lasing molecules pumped by $E \rightarrow V$ energy transfer from $\text{Br}(^2P_{1/2})$ is listed in Table 4.1.⁴¹ The table lists the molecular species, the observed laser wavelength, and the corresponding vibrational transition.

Table 4.1

List of Infrared Lasing Molecules⁴¹

Molecule	Laser Wavelength (μm)	Transition
CO ₂	4.3	(101)–(100)
CO ₂	≈ 4.3	(021)–(020)
CO ₂	10.6	(001)–(100)
CO ₂	14.1	(101)–(011)
N ₂ O	10.9	(001)–(100)
HCN	3.85	(001)–(010)
HCN	7.25	(100)–(010)
HCN	8.48	(001)–(100)
C ₂ H ₂	7–8	(00100)–(01000)
H ₂ O	7.1	(020)–(010)
H ₂ O	7.3	(020)–(010)
H ₂ O	7.4	(020)–(010)
H ₂ O	7.6	(020)–(010)
H ₂ O	7.7	unassigned
H ₂ O	16.9	unassigned
NO	5.5	$v = 2 - 1$

After considering the quenching rates obtained from the photolysis study and which species had previously been shown to lase, the gases in Table 4.2 were chosen for further consideration. CO₂ and HCN had recently been studied by Pastel and others.¹⁰ The water molecules have large Br* quenching rate coefficients, but the lasing transitions correspond to

atmospheric absorption wavelengths which limit operational utility. NO and N₂O are considered as possible candidates for study, and NO is selected. The second vibrational level of NO is at 3808 cm⁻¹, which is nearly resonant with the 3685 cm⁻¹ of Br* electronic energy; a desired attribute for efficient E → V energy transfer.

Table 4.2

Candidate Laser Acceptor Molecules

Species	Quenching Rate Coefficient (10 ⁻¹² cm ³ /molec-s)	Ground State ω_e ²⁰ or Vibrational Frequencies ²⁶ (cm ⁻¹)
CO ₂	13.2 ± 0.2 *	$\nu_1 = 1388.17$ $\nu_2 = 667.40$ $\nu_3 = 2349.16$
D ₂ O	9.6 2.2 ± 0.4	
H ₂ O	32 62 51 ± 3	$\nu_1 = 3657.0$ $\nu_3 = 1594.7$ $\nu_3 = 3755.7$
HCN	20 ± 2	$\nu_2 = 423$ $\nu_3 = 1475$
HDO	19 ± 4	
NO	2.4 ± 0.1 *	1904.03
N ₂ O	2.8 ± 0.2 *	$\nu_1 = 2223.76$ $\nu_3 = 588.78$ $\nu_3 = 1284.9$

* Rate determined by current research.

Although NO had been shown to lase by Peterson³⁵, the research was primarily directed toward H₂O, and the NO and N₂O results were limited. The NO($v = 2 - 1$) vibrational transition is chosen for the NO laser. With an energy separation of 1817 cm⁻¹, the approximate 5.4 μ m emission is suitable for an infrared countermeasure laser.

As a test of the spectroscopic and kinetic data base, a photo-initiated, gas-phase Br* laser operating at 2.71 μ m is constructed, operated, and characterized. Second, a 4.3 μ m Br* - CO₂ laser is constructed, and the measured operation of this laser is compared to previous research to eliminate systematic errors. Finally, NO is substituted for the CO₂, and an NO laser operating near 5.4 μ m is characterized and the results analyzed. The CO₂ laser is used as a baseline for comparing NO laser output energy, efficiency, and operating parameters.

2. *Laser Physics*

The YAG pump laser photons dissociate the IBr to form Br(²P_{1/2}) atoms. These atoms transfer their electronic energy to molecular laser candidates through collisions. This E \rightarrow V energy transfer rate and cavity gain are the main factors that determine the amount of time after the pump pulse that lasing begins. The threshold condition for lasing is

$$(T_{BW})^4 (R_1 R_2) \exp(2 l \gamma_{th}(\nu)) = 1 \quad (4.1)$$

where

T_{BW} = Brewster window transmissivity (per window)

R_n = cavity mirror reflectivities

l = gain medium length (cm)

$\gamma_{th}(\nu)$ = medium gain coefficient cm^{-1} ; the minimum gain coefficient required for lasing

The threshold gain coefficient can be written as

$$\gamma_{th}(\nu) = \frac{1}{2l} \ln \left(\frac{1}{(T_{BW})^4 (R_1 R_2)} \right) \quad (4.2)$$

For the present research, the gain medium length is 90 cm, and the mirror reflectivities are 99 percent. The minimum gain that will support lasing is $\gamma_{th}(\nu) = 2.31 \times 10^{-3} \text{ cm}^{-1}$.

The gain of the laser is a function of the population inversion between the upper and lower laser levels, ΔN , and the stimulated emission cross section, $\sigma_{se}(\nu)$, as shown in Equations (4.3) and (4.4) where g_n is the degeneracy of level n :

$$\gamma(\nu) = \Delta N \sigma_{se}(\nu) \quad (4.3)$$

$$\Delta N = N_2 - \frac{g_2}{g_1} N_1 \quad (4.4)$$

The stimulated emission cross section is a function of the transition line shape evaluated at the center frequency, $g(\nu_0)$, and the Einstein A coefficient for the laser transition, shown in Equation (4.5):

$$\sigma_{se}(\nu_0) = A_{21} \frac{\lambda^2}{8\pi} g(\nu_0) \quad (4.5)$$

The population in the upper laser level, N_2 , is determined by the amount of Br^* created by the dissociating pump laser and by the transfer rate to the molecular laser species. The initial Br^* concentration is determined by the amount of absorbed pump laser intensity (energy), which is determined by the IBr absorption cross section, path length, and IBr concentration according to Beer's law. These relations are shown in Equations (4.6) and (4.7):

$$I_{\text{absorbed}} = I_p - I_t \quad (4.6)$$

$$I_t = I_p \exp(-\sigma_{\text{IBr}} l [\text{IBr}]) \quad (4.7)$$

where,

I_{absorbed} = average absorbed pump laser intensity (watts cm^{-2})

I_p = incident pump laser intensity (watts cm^{-2})

I_t = transmitted pump laser intensity (watts cm^{-2})

As previously mentioned, the IBr absorption cross section at 532 nm is $8.22 \times 10^{-19} \text{ cm}^2$.³⁷

The initial Br* concentration is related to the absorbed intensity and the Br* photon yield of IBr at 532 nm, $\Phi(\lambda)$, by Equation (4.8):

$$[\text{Br}^*]_{t=0} = \frac{I_{\text{absorbed}}}{\nu_r l h\nu} \Phi(532) \quad (4.8)$$

where ν_r is the pump laser repetition rate in Hz and $h\nu$ is the pump photon energy. The Br* photon yield from IBr at 532 nm is approximately 0.68.^{22, 23}

The temporal Br* concentration is determined by the overall Br* lifetime, τ , by Equation (4.9):

$$[\text{Br}^*]_t = [\text{Br}^*]_{t=0} \exp(-t/\tau) \quad (4.9)$$

where,

$$\frac{1}{\tau} = \sum_i k_i [i] + k_0$$

which is the sum of the constituent cell gas concentrations times their respective quenching rates plus any non-pressure dependent quenching rate. From this data, the Br* concentration is known as a function of time.

The Einstein A coefficients for the NO transitions are taken from Billingsley; $A_{2-1} = 20.43 \text{ sec}^{-1}$, $A_{2-0} = 0.46 \text{ sec}^{-1}$, $A_{1-0} = 10.78 \text{ sec}^{-1}$.⁴³ Assuming low pressure operation, the Doppler-broadened line shape is given

in Equation (4.10), where $\Delta\nu_D$ is the Doppler transition width, given in Equation (4.11):

$$g(\nu_0) = \sqrt{\frac{4 \ln 2}{\pi}} \frac{1}{\Delta\nu_D} \quad (4.10)$$

$$\Delta\nu_D = 7.13 \times 10^{-7} \sqrt{\frac{T}{m}} \nu_0 \quad (4.11)$$

where m is the mass of the lasing molecule in atomic mass units and ν_0 is the center frequency of the lasing transition. The energy difference of the $\text{NO}(\nu = 2-1)$ transition is 1841.15 cm^{-1} ,⁴⁴ yielding a transition wavelength of $5.43 \text{ }\mu\text{m}$. The stimulated emission cross section for $\text{NO}(\nu = 2 - 1)$ is calculated from Equation (4.5) to yield $\sigma_{\text{se}} = 1.81 \times 10^{-15} \text{ cm}^2$. To achieve lasing, the laser condition from Equation (4.2) must be satisfied; $\gamma(\nu) > 2.31 \times 10^{-3} \text{ cm}^{-1}$. This requirement implies a necessary population inversion, ΔN , of $1.28 \times 10^{12} \text{ molecules cm}^{-3}$ to achieve lasing.

Similar analysis yields stimulated emission cross sections for CO_2 and Br^* of 9.57×10^{-18} and $1.61 \times 10^{-17} \text{ cm}^2$, respectively, using 0.18 sec^{-1} for the Einstein A coefficient for $\text{CO}_2(101-100)$ which is actually for the nearby $(001-000)$ transition. The required population inversions for CO_2 and Br^* are $2.41 \times 10^{14} \text{ molecules cm}^{-3}$ and $1.43 \times 10^{14} \text{ molecules cm}^{-3}$, respectively, reflecting the lower stimulated emission cross sections. The population inversion required for the CO_2 laser also reflects the energy penalty that is paid for polyatomic molecules whose rotational partition functions allow much spreading of the transferred energy.

The rotational levels within the vibrational levels are thermally populated. Using the standard Boltzmann rotational distribution function and the rotational constants $B_e = 1.7046 \text{ cm}^{-1}$ and $\alpha_e = 0.0178 \text{ cm}^{-1}$,²⁰ Figure 4.1 shows the thermal distribution of rotational levels in the first NO vibrational level at 300 K.

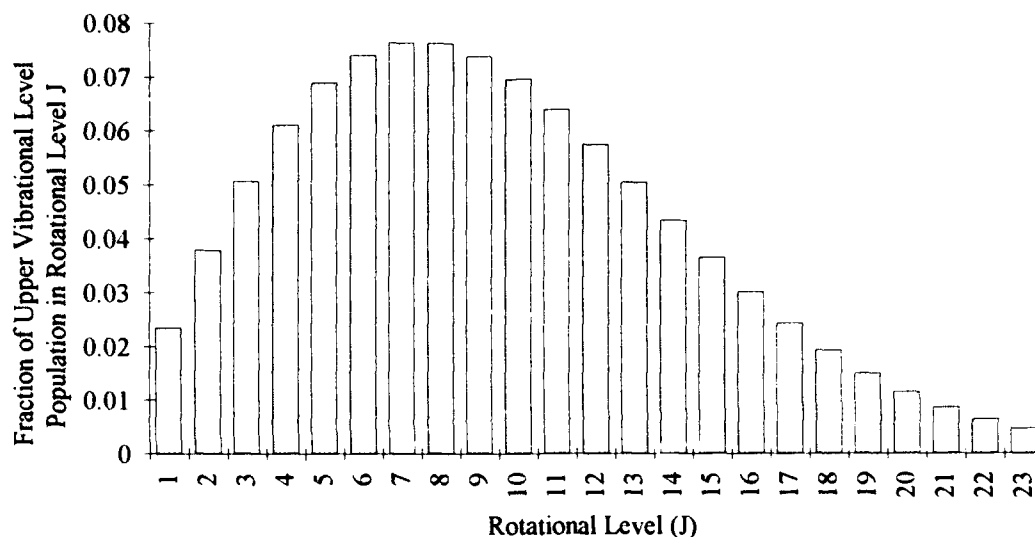


Figure 4.1. Rotational line distribution for NO($v = 1$) showing the fraction of lower level molecules in rotational level J .

The rotational level that has the highest population in both vibrational levels is $J = 7$. The rotational distribution represents a spreading of the transferred Br* electronic energy and the rotational level with the highest population inversion is the most likely to lase first. The tail on the NO laser pulses may be due to a combination of ro-vibrational levels lasing. As is pointed out earlier, Peterson saw pulse-to-pulse variation in the NO lasing wavelength and attributed it to various individual lasing lines.³⁵ Peterson

found the average lasing wavelength to correspond to the center of the NO(2, 1) *P*-branch. The data from the present study is consistent with that finding.

Before lasing begins, the laser levels may be assumed to be thermally populated as a Boltzmann distribution. Considering the vibrational and rotational thermal populations with 300 mTorr of NO and CO₂ present, the populations of the upper ro-vibrational levels of the NO and CO₂ lasers required for lasing are 1.39×10^{12} and 2.42×10^{14} molecules cm⁻³, respectively. The total population required in the NO($v = 2$) and CO₂(101) upper vibrational levels are 1.85×10^{13} and 6.51×10^{15} molecules cm⁻³, respectively.

C. Experiment

The laser demonstration schematic diagram is shown in Figure 4.2. The system design is similar to that used by Pastel and others in their Br* laser research.¹⁰

The gas handling system is essentially the same as that used in the photolysis experiments. A 10-Torr capacitance manometer (CM) is used to measure cell pressure. A sample of iodine monobromide is degassed by repeatedly freezing to 77 K and pumping while thawing to about 200 K. As the sample purity improves, the amount that the cell pressure increases during each freeze-thaw cycle decreases. Phosphorus pentoxide (P₂O₅) is added to the bulb containing the IBr to absorb residual water. When filling the cell, the middle fraction of the IBr gas is used to improve purity.

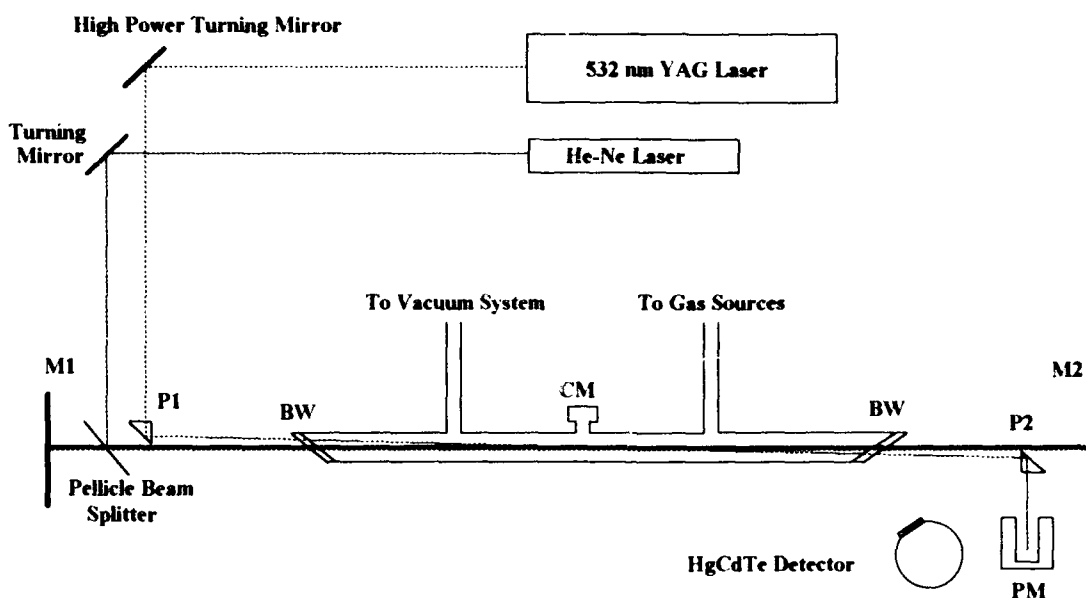


Figure 4.2. Schematic diagram of the laser demonstration apparatus.

The dissociating source is a Quanta-Ray model DCR-3, pulsed Nd:YAG laser. The maximum YAG output energy is 150 mJ in a 10–20 ns pulse. The laser is operated at repetition rates of 20 Hz.

The 90 cm long gas cell is constructed of 1/2 inch OD glass tubing. Both calcium fluoride (CaF_2) and barium fluoride (BaF_2) are used as Brewster windows. The wide infrared bandpass of BaF_2 is preferred, but CaF_2 has a higher damage threshold; both were used in all laser experiments. Both types of window suffer from a buildup of contaminants after approximately one hour of operation. This buildup primarily occurs at the location of the YAG pump laser energy on the window, but it can spread to the entire Brewster window and stop lasing. The resonator consists of two 2 inch gold-coated, high-reflective (0.99) mirrors separated by 1.5 m. One of

the mirrors, M1, is flat, and the second mirror, M2 has a 5 m radius of curvature.

In order to maximize the absorption path length and avoid damage to the laser mirrors, the YAG laser energy is brought into the gain medium via a right angle prism, P1, and passes out of the gas cell via prism P2 into a power meter. The 532 nm beam must travel the length of the gas cell at a small angle with respect to the laser axis to allow maximum $E \rightarrow V$ energy transfer from Br^* to the acceptor molecule.

The stimulated emission is measured by an infrared detector positioned very near the Brewster window. Infrared light scattered from the Brewster window is detected by a Kolmar Technologies HgCdTe infrared detector model KV103-0.1-A-2-2SMA(.2). The LN_2 -cooled detector is AC-coupled, and has two active elements: 1 mm square and 2 mm square. Both elements have an RC-limited bandwidth exceeding 100 MHz with response times rated at 1.6 ns. The small element is faster, and is used in all experiments. The detector response to the YAG laser pulse is compared to the response of an FND-100 detector and found to yield equivalent results.

OCLI bandpass interference filters are placed in front of the detector window to block all light except the desired laser wavelengths. The Br^* laser experiment uses the same narrow $2.71 \mu\text{m}$ filter as is used in the photolysis experiments. The CO_2 laser experiment uses a filter centered at $4.32 \mu\text{m}$ with a $0.28 \mu\text{m}$ FWHM. The NO laser experiment uses a filter centered at $5.35 \mu\text{m}$ with a $0.70 \mu\text{m}$ FWHM.

A He-Ne laser and pellicle beam splitter are used to align the laser cavity. The details of the YAG pump beam, prisms, cavity mirrors, and detector alignment procedure are in Appendix C.

As previously mentioned, when Br_2 and NO are combined, BrNO may be photolytically formed.²⁹ To reduce the BrNO reaction time for the NO and Br_2 created from bromine atom recombination, a black cloth covers the entire laser apparatus during all NO laser experiments. Experiments are performed using the absorption diagnostic which show that when 2 Torr of Br_2 is mixed with 100 mTorr of NO, the cross section for absorption for the mixture does not change until after several hours indicating the absence of the BrNO reaction. Since the reaction to form BrNO is photolytic, by keeping the sample from light, the amount of BrNO formed can be kept small.

D. Results

1. Br Laser*

The normalized Br^* laser emission intensities for a family of YAG pump laser energies from 25 to 125 mJ per pulse are shown in Figure 4.3.

At the maximum pump energy of 125 mJ per pulse, the Br^* laser pulse begins about 300 ns after the pump pulse ($t = 0$) and is approximately 300 ns FWHM in duration. The pulse shapes are shown for an IBr pressure of two Torr. The time to threshold decreases with increasing pump energy as the initial Br^* population inversion increases. Operation is stable for several hours on a single IBr fill, and efficiency is typically limited by deposits on the inside of the Brewster windows, primarily at the pump laser entrance.

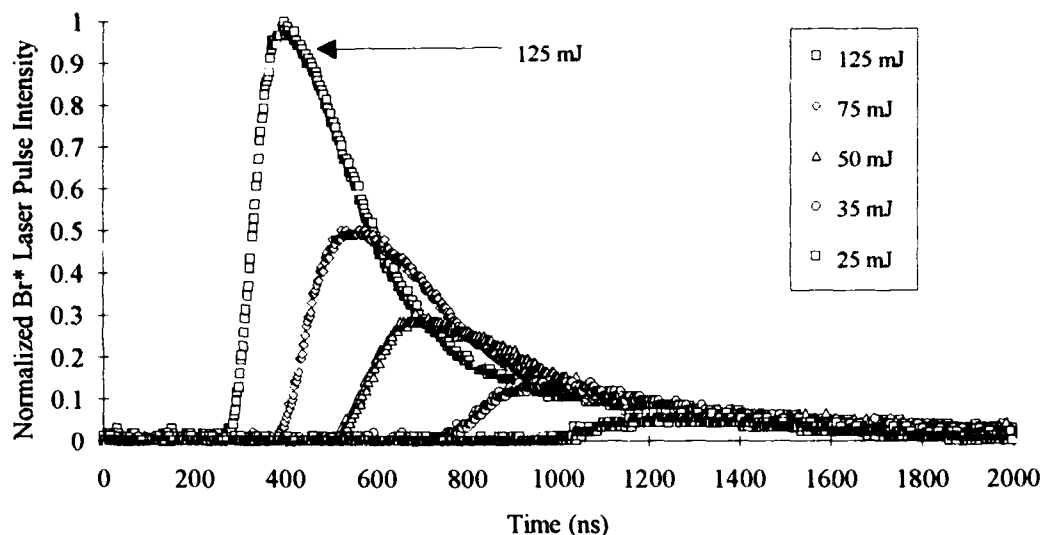


Figure 4.3. Family of Br* laser pulse shapes showing the variation in time to threshold as a function of YAG pump energy per pulse with 2 Torr IBr.

Figure 4.4 shows the area of each pulse in Figure 4.3 plotted as a function of 532 nm pump laser energy. The Br* laser pulse area is proportional to laser pulse energy. From this figure a pump laser energy threshold of 20 to 25 mJ per pulse is established. The increase in the Br* pulse energy decreases slightly with increasing laser pump energy. That is, the slope of the curve in Figure 4.4 tends to decrease with increasing pump power. This effect may be due to photo-bleaching of the IBr at higher pump energies. The absorption cross section of IBr at 532 nm³⁷ is $8.22 \times 10^{-19} \text{ cm}^2$, and bleaching may deplete the IBr concentration on the pump-laser axis when the total pump energy is much greater than $Ah\nu / \sigma$, where A is the pump beam area. The diameter of the pump beam is approximately 4.0 mm, which implies substantial bleaching occurs when the pump beam energy is greater than 100 mJ per pulse.

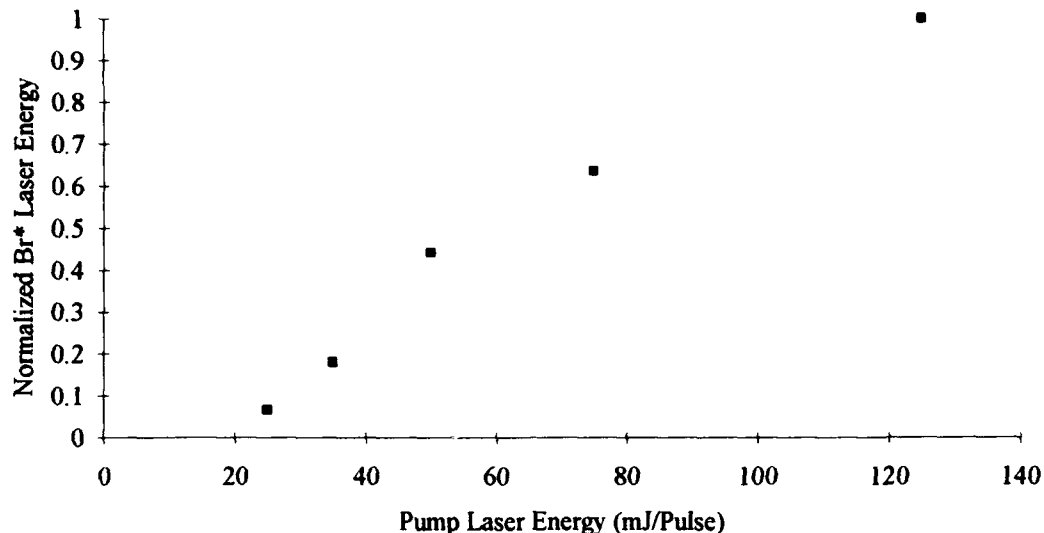


Figure 4.4. Normalized Br* laser energy as a function of YAG pump energy showing lasing threshold near 20 mJ/Pulse.

The Br* laser pulse temporal profiles for a family of IBr pressures are plotted in Figure 4.5, and the Br* energy as a function of IBr pressure is shown in Figure 4.6. Lasing is observed for IBr pressures from 600 mTorr to 6.5 Torr with a pump laser energy of 125 mJ per pulse. Figure 4.5 shows that the time delay before lasing begins decreases as the IBr pressure increases. Note also that the energy per pulse, shown in Figure 4.6, decreases at higher IBr pressures as also shown in the data collected by Pastel.¹⁰ The discontinuity in the pulse energy seen in Figure 4.6 at IBr pressures of about 2.5 Torr is due to a reduction in the duration of the laser pulse, not the amplitude, which is evident in Figure 4.5. Pastel points out that the gradual decrease in pulse energy for IBr pressures above 3 Torr may be due to an increase in the iodine atom concentration which quenches Br* at $1.8 \times 10^{-11} \text{ cm}^3/\text{molecule}\cdot\text{s}$.¹⁰

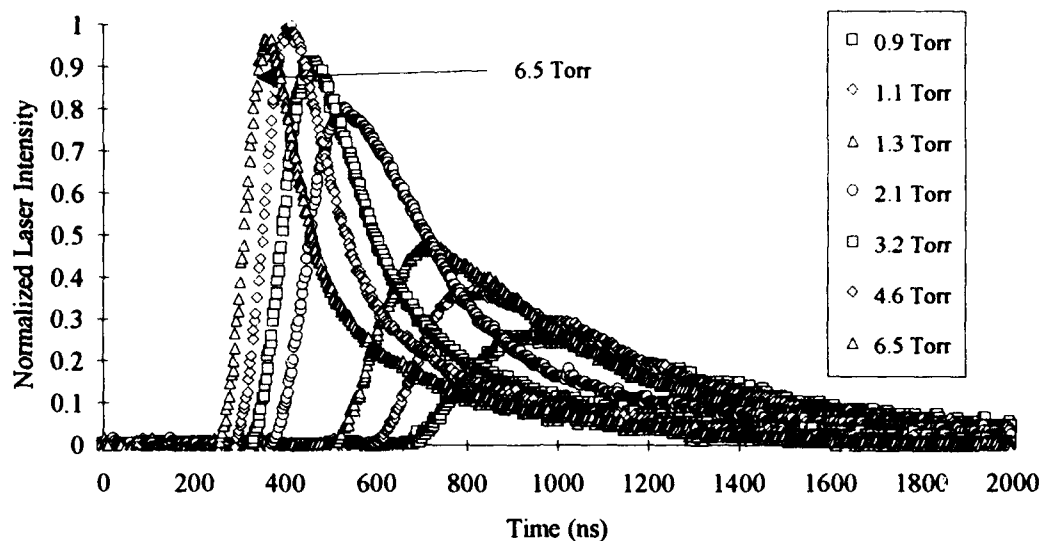


Figure 4.5. Family of Br* laser pulse shapes for IBr pressures from 0.9 to 6.5 Torr at a pump energy of 125 mJ per pulse.

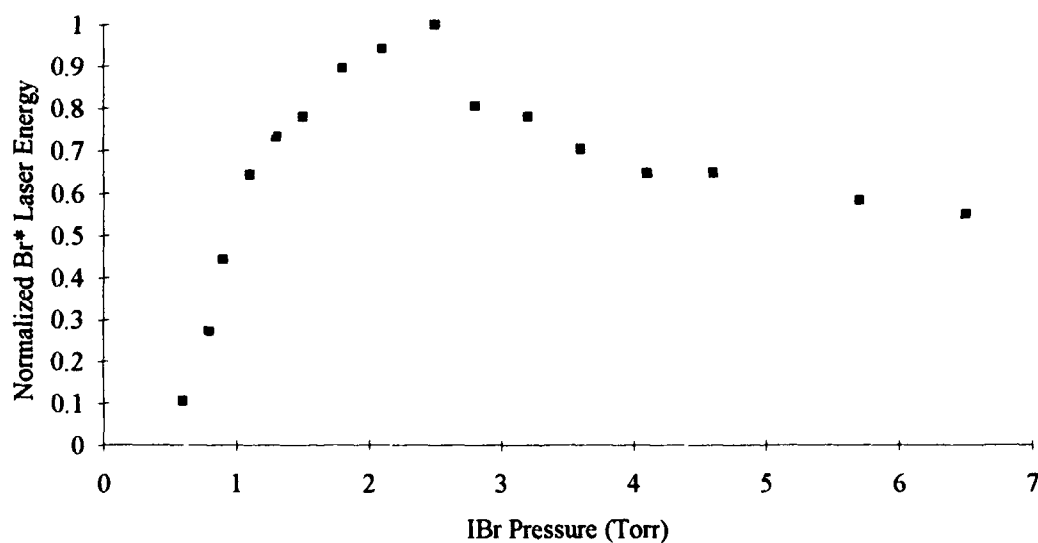


Figure 4.6. Normalized Br* laser pulse energy as a function of IBr pressure showing a reduction in pulse energy at IBr pressures above 3 Torr.

2. CO_2 Laser

Having achieved lasing with Br^* , CO_2 is added to the apparatus to obtain CO_2 lasing at $4.3\text{ }\mu\text{m}$. After adding CO_2 , small adjustments are made to the cavity mirrors and detector position to achieve lasing. The $4.3\text{ }\mu\text{m}$ interference filter is used to observe the desired transition. As previously mentioned, most of the Br^* electronic energy is transferred to the (101) vibrational level of CO_2 .⁶ The lasing transition is from the (101) vibrational level to the (100) vibrational level at $4.3\text{ }\mu\text{m}$.⁶

As seen in Figure 4.7, with 1.8 Torr IBr and 300 mTorr CO_2 , the lasing pulse begins approximately 200 ns after the pump pulse at the maximum pump energy. As in the Br^* laser, the pulse delay also increases with decreased pump energy.

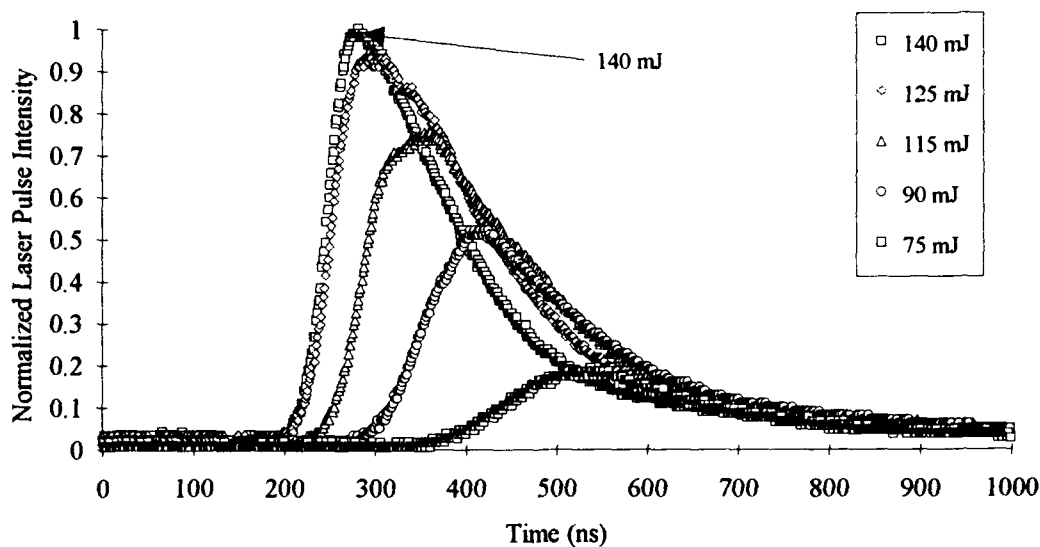


Figure 4.7. Family of CO_2 laser pulse shapes showing the variation in time to threshold as a function of YAG pump energy per pulse for 1.8 Torr IBr and 300 mTorr of CO_2 .

When the energy of the CO₂ laser pulse is plotted versus pump energy, as shown in Figure 4.8, the pump-laser energy threshold calculated from the zero-area intercept on the abscissa is near 65 to 70 mJ, which is a higher threshold than was observed in the Br* case. Part of the effect may be attributed to the use of a different set of Brewster windows which may not have the same losses. The decrease in the area of the CO₂ laser pulses for higher pump energies may be caused from IBr bleaching as discussed above.

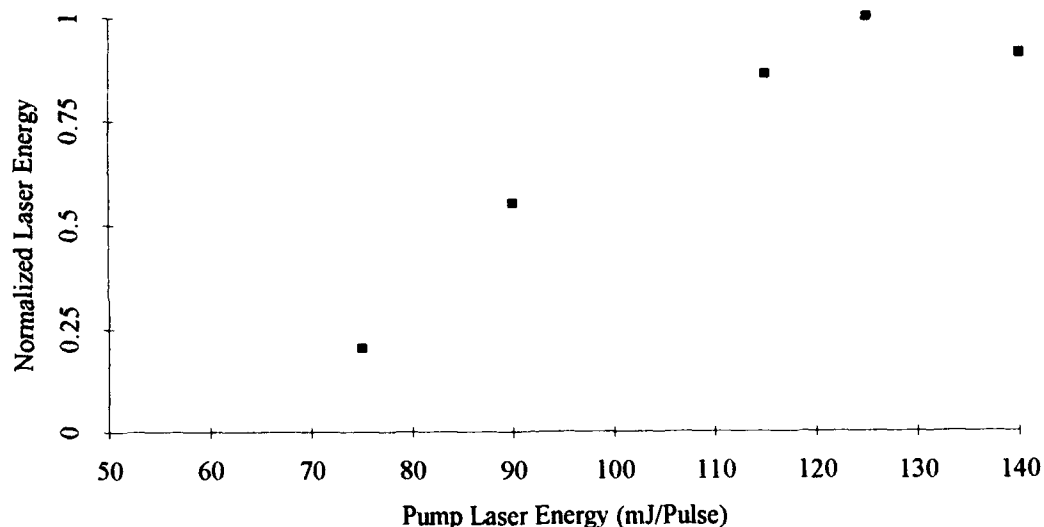


Figure 4.8. Normalized CO₂ laser energy as a function of YAG pump energy showing lasing threshold near 70 mJ/Pulse.

With 2 Torr IBr, the CO₂ laser pulse temporal profiles for a family of CO₂ pressures are plotted in Figure 4.9, and the pulse energy as a function of CO₂ pressure is shown in Figure 4.10. The peak energy occurs for a CO₂ pressure of 400 mTorr, and drops off sharply at higher CO₂ pressures, as seen in the figures. This decrease in the pulse energy is due to the rapid rate

at which ground state CO_2 molecules quench molecules in the (101) vibrational level. The quenching rate for the excited molecule removal by ground state CO_2 is $1.3 \times 10^{-10} \text{ cm}^3/\text{molecule}\cdot\text{s}$.⁴²

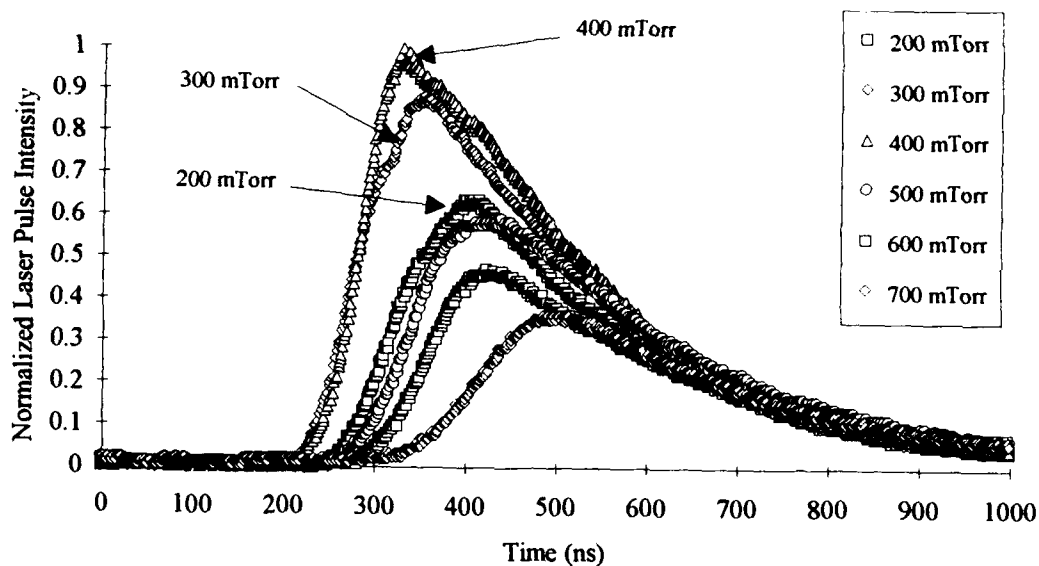


Figure 4.9. Family of CO_2 laser pulse shapes for CO_2 pressures from 200 to 700 mTorr at a pump energy of 125 mJ per pulse and 2 Torr IBr.

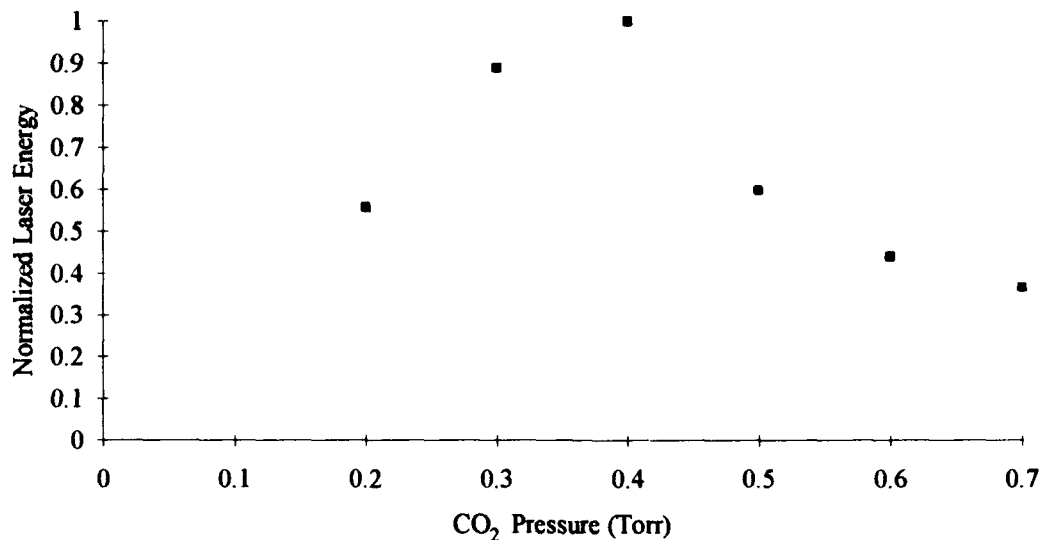


Figure 4.10. Normalized CO₂ laser energy as a function of CO₂ pressure showing a peak in energy at 400 mTorr of CO₂ at a pump energy of 125 mJ per pulse and 2 Torr IBr.

3. NO Laser

Nitric oxide lasing is achieved when NO is added to 2.8 Torr of IBr. Again, slight adjustments are made to the mirrors and detector to initiate lasing. The NO laser temporal behavior for a family of YAG pump laser energies from 25 to 140 mJ per pulse is shown in Figure 4.11. A 5.3 μm interference filter is used to observe the NO($v = 2 - 1$) transition. The NO laser pulse begins approximately 150 ns after the pump pulse and lasts for a few hundred nanoseconds. The pulse widths decrease rapidly with decreasing pump power.

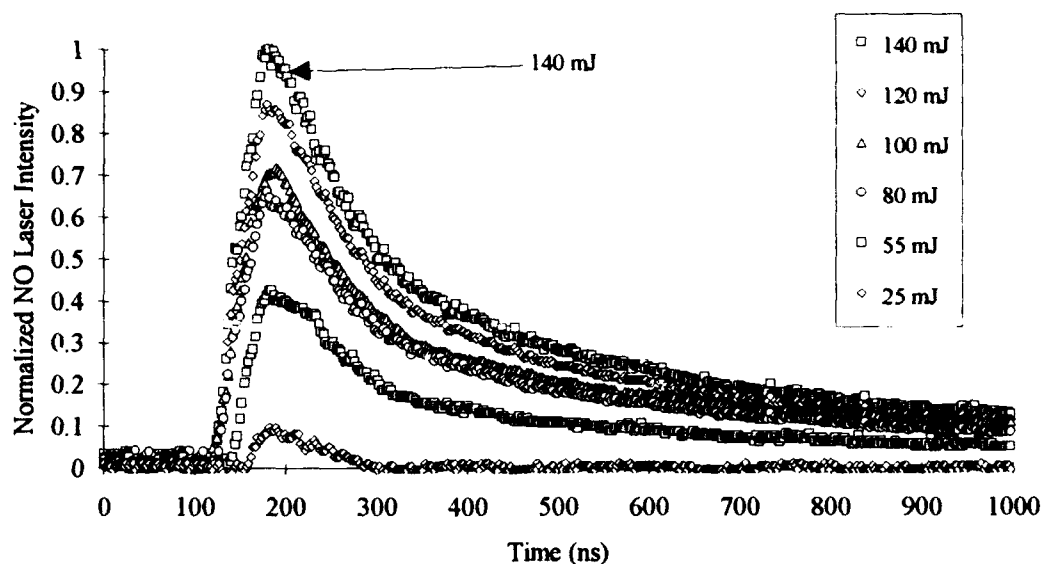


Figure 4.11. Family of NO laser pulse shapes showing the variation in time to threshold as a function of YAG pump energy per pulse with 2.8 Torr IBr and 200 mTorr of NO.

The NO laser pulse area plotted versus pump energy is shown in Figure 4.12. The pump-laser energy threshold calculated from the zero-area intercept on the pump energy axis is near 25 mJ per pulse. This threshold is only slightly higher than the Br* laser threshold shown earlier. This plot of pulse area continues to increase for increasing pump energy unlike the CO₂ laser case. This fact makes the IBr bleaching argument less plausible. This observed increase in area may be due to the long tail in the laser pulses which may be due to a cascading of rotational lasing transitions within the $v = 2, 1$ vibrational levels.

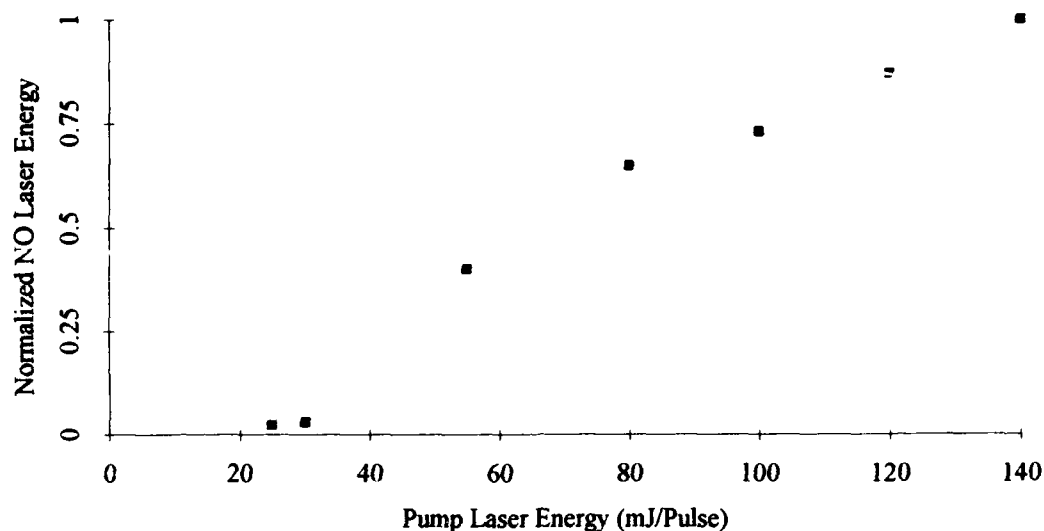


Figure 4.12. Normalized NO laser energy as a function of YAG pump energy showing a lasing threshold near 25 mJ per pulse.

With 2.8 Torr IBr, the NO laser temporal pulse profiles for a family of NO pressures are plotted in Figure 4.13, and the pulse energy as a function of NO pressure is shown in Figure 4.14. The figures show a limited region of optimum performance as the pulse area drops off rapidly as the NO pressure increases. This effect is thought to be due to $V \rightarrow V$ energy transfer or self relaxation of $\text{NO}(v = 2)$ molecules by NO which occurs at a rate of $1.2 \pm 0.4 \times 10^{-12} \text{ cm}^3/\text{molecule}\cdot\text{s}$.²⁹ Finally, any BrNO formation can reduce the population in the upper level, which quenches $\text{NO}(v = 2)$ at $1.5 \pm 0.2 \times 10^{-11} \text{ cm}^3/\text{molecule}\cdot\text{s}$.³⁰

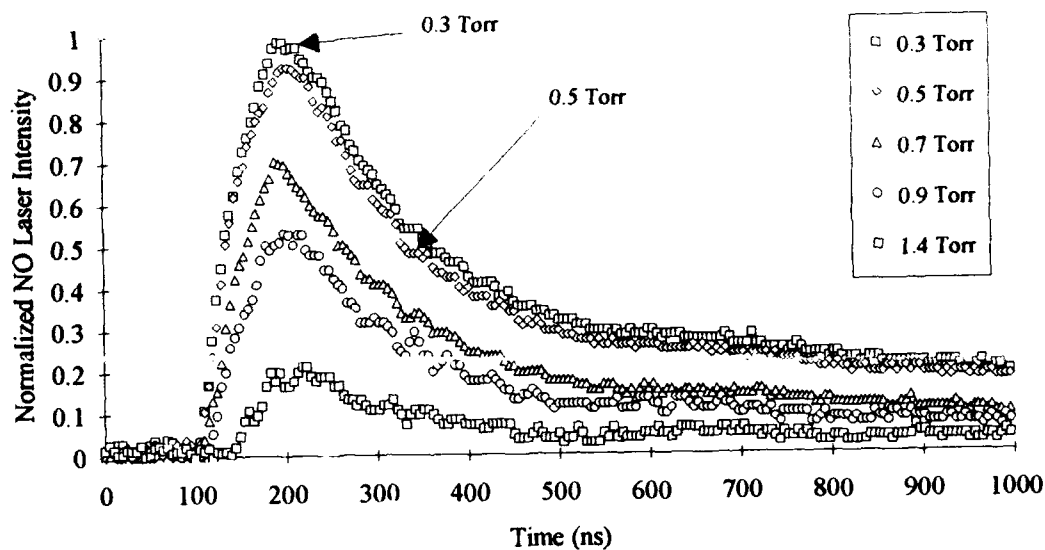


Figure 4.13. Family of NO laser pulse shapes for NO pressures from 0.1 to 1.4 Torr at a pump energy of 140 mJ per pulse and 3 Torr IBr.

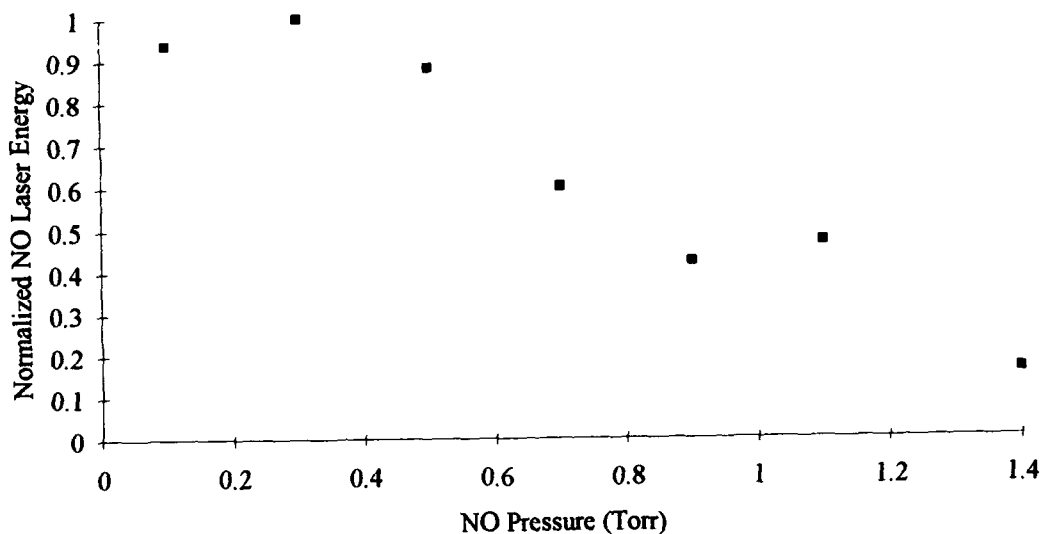


Figure 4.14. Normalized NO laser energy as a function of NO pressure showing a peak in laser energy at NO pressures near 300 mTorr with 3 Torr IBr.

E. Discussion

Pulses for the CO_2 and NO laser systems are shown in Figure 4.15. Pastel found the energy produced by a similarly-designed $\text{Br}^*\text{-CO}_2$ laser to be approximately 0.1 mJ per pulse at a pump energy of 85 mJ per pulse.¹⁰ The ratio of the CO_2 and NO maximum pulse areas is approximately 10:1. The detector efficiency is essentially unchanged between these wavelengths, and the bandpass filters' transmittances are approximately equal. By comparing the energy ratio and using Pastel's absolute value for the CO_2 energy, the relative NO energy is found to be 0.01 mJ per pulse. This value is only an approximation since differences in detector position and pump beam alignment affect the output energy. It is clear from the data, however, that *the NO energy is significantly less than the CO_2 energy in all cases.*

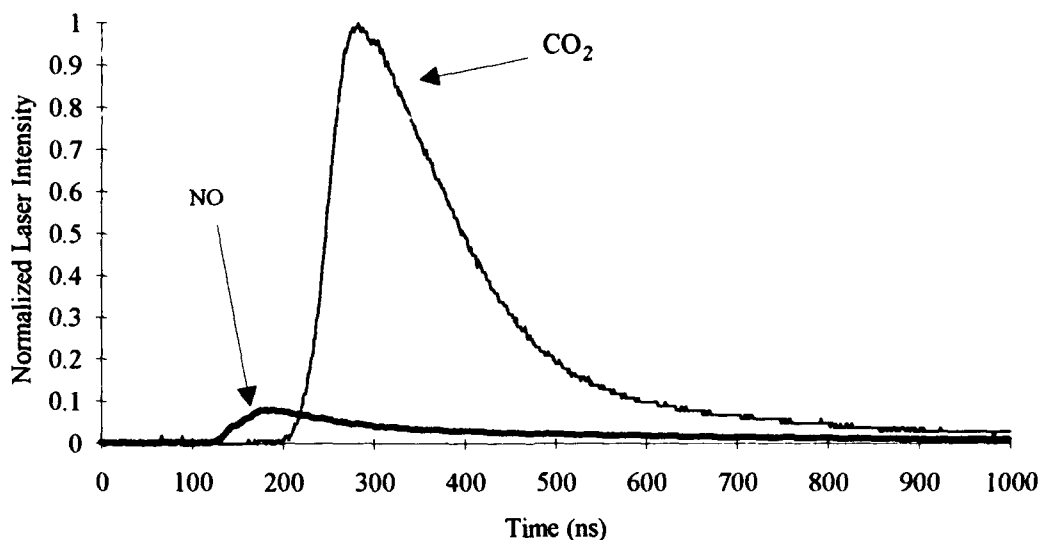


Figure 4.15. Temporal profile of CO_2 and NO laser pulses showing an approximate 10:1 ratio in laser output energies.

The maximum energy conversion efficiency for the CO₂ laser occurs at a CO₂ pressure of 400 mTorr and a pump energy of 125 mJ per pulse. The maximum conversion efficiency for these conditions is 0.16 percent. The maximum NO conversion efficiency occurs at 300 mTorr of NO and a pump energy of 85 mJ per pulse. The corresponding maximum energy conversion efficiency of the NO laser is 0.012 percent. The maximum energy per pulse for the Br* laser occurs at an IBr pressure of approximately 2.5 Torr for pump energies from 50 to 125 mJ per pulse. Considering the detector response and the transmissivity of the 2.71 μm filter, the maximum conversion efficiency of the Br* laser is 0.71 percent.

From Equation (4.8), for 2 Torr of IBr, a laser energy of 125 mJ per pulse and a pulse repetition rate of 20 Hz, the initial concentration of Br* is 1.99×10^{16} molecules cm^{-3} . Assuming Br* is quenched primarily by IBr, NO, I₂, and Br₂,⁵ the Br* lifetime is found from Equation (4.9) where

$$\frac{1}{\tau} = k_{\text{IBr}} [\text{IBr}] + k_{\text{NO}} [\text{NO}] + k_{\text{I}_2} [\text{I}_2] + k_{\text{Br}_2} [\text{Br}_2] \quad (4.12)$$

and where

$$k_{\text{NO}} = 2.4 \times 10^{12} \text{ cm}^3/\text{molecule-s}$$

The amount of I₂ and Br₂ are small, about four percent each,²³ according to the equilibrium: $\text{I}_2 + \text{Br}_2 \rightleftharpoons 2 \text{IBr}$, $K_{\text{eq}} = 480$,⁵ and make minimal contributions to the observed lifetime.

The Br* gives up energy to NO($v = 2$) at an electronic-to-vibrational energy transfer rate, $k_{\text{E-V}_2} = 2.01 \times 10^{12} \text{ cm}^3/\text{molecule-s}$ and to NO($v = 1$) at $k_{\text{E-V}_1} = 3.35 \times 10^{13} \text{ cm}^3/\text{molecule-s}$.²⁹ NO is quenched by $\text{V} \rightarrow \text{V}$, T

relaxation by ground state NO, and by the cell gases IBr, Br₂, and I₂. The relaxation rate due to ground-state NO, $k_{2-0} = 1.2 \times 10^{-12} \text{ cm}^3/\text{molecule-s}$.²⁹

In order to understand some of the properties of the NO energy transfer laser, the following simple model is utilized. The concentration in the upper laser level, NO($v = 2$), is denoted N_2 , and the concentration in the lower laser level, NO($v = 1$), is denoted N_1 . The concentration in the ground vibrational level of NO is denoted by N_0 . The approximate time evolution of the upper and lower laser levels is given by Equations (4.13) and (4.14):

$$\begin{aligned} \frac{d N_2(t)}{dt} = & N_0 k_{E-v_2} [\text{Br}^*]_{t=0} \exp(-t/\tau) \\ & - N_2(t) (N_0 k_{2-0} + k_{\text{IBr}} [\text{IBr}] + (A_{21} + A_{20})) \\ & - I(t) (N_2(t) - N_1(t)) \frac{\sigma_{\text{SE}}}{h \nu} \end{aligned} \quad (4.13)$$

$$\begin{aligned} \frac{d N_1(t)}{dt} = & N_0 k_{E-v_1} [\text{Br}^*]_{t=0} \exp(-t/\tau) - N_1(t) A_{10} \\ & - I(t) (N_1(t) - N_2(t)) \frac{\sigma_{\text{SE}}}{h \nu} + N_2(t) A_{21} \end{aligned} \quad (4.14)$$

where

σ_{SE} = stimulated emission cross section (cm^2)

evaluated at the transition center frequency

The intensity, I , of the photons in the cavity is given by the rate equation

$$\begin{aligned} \frac{d I(t)}{dt} = & I(t) (N_2(t) - N_1(t)) c \sigma_{SE} \\ & + N_2(t) \frac{c^2 \sigma_{SE} h \nu}{V_M} - \frac{I(t)}{T_C} \end{aligned} \quad (4.15)$$

where

V_M = laser cavity mode volume (cm³)

T_C = photon cavity lifetime (sec)

Equations (4.13) through (4.15) are solved using *Mathematica* with $V_M = 11$ cm³, $T_C = 60$ ns, and the remaining values as previously determined. The lasing intensity as a function of time is shown in Figure 4.16.

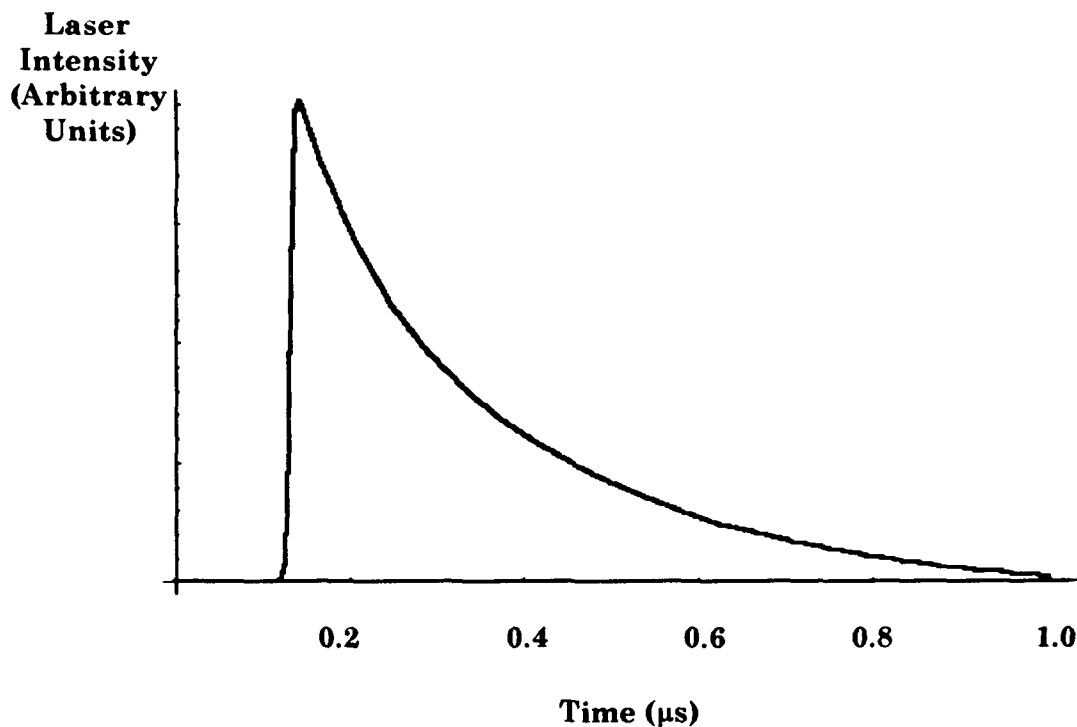


Figure 4.16. Modeled temporal plot of the NO laser intensity.

The initial conditions are $N_1(0) = 1.2 \times 10^{12}$ molecules/cm³ and $N_2(0) = I(0) = 0$. Assuming 3 Torr of IBr, and 300 mTorr of NO, $\tau = 1.5 \times 10^{-7}$ sec. The rate equation model is used to extract the value of $k_{IBr} = 7 \times 10^{-11}$ cm³/molecule-s, which is the quenching rate of IBr on NO($v = 2$). The peak intensity of the modeled pulse appears at about 125 ns, which is near the time of the experimental data peak. The rise time of the modeled pulse appears faster than the experimental data, which may reflect the finite bandwidth of the IR detector. There may still be second order effects taking place in the Br^{*}-NO laser, such as the role of BrNO if present, and V - T relaxation from the NO($v = 1$) level.

F. Conclusion

A photolytic, pulsed Br($4^2P_{1/2} - 4^2P_{3/2}$) laser operating at 2.714 μ m is demonstrated by photodissociation of IBr at 532 nm using a frequency-doubled Nd:YAG laser. Lasing is observed for pump energies from 25 to 125 mJ per pulse and for IBr pressures from 600 mTorr to 6.5 Torr. Pulsed infrared lasers are also demonstrated in which the pumping mechanism is electronic-to-vibrational energy transfer from Br($2^2P_{1/2}$) to CO₂(101) and NO($v = 2$). The CO₂ laser operates on the (101 \rightarrow 100) transition at 4.3 μ m for CO₂ pressures from 200 to 700 mTorr with 2 Torr of IBr and for pump energies from 75 to 140 mJ per pulse. The NO laser operates on the ($v = 2 - 1$) vibrational transition near 5.4 μ m for NO pressures from 100 mTorr to 1.4 Torr and for pump energies from 25 to 125 mJ per pulse. The ratio of laser energy for the CO₂ and NO pulsed lasers is 10 : 1, indicating an approximate NO laser energy of 0.01 mJ per pulse with 85 mJ

per pulse pump energy. This corresponds to an approximate energy conversion efficiency of 0.012 percent, while the CO₂ conversion efficiency is 0.12 percent. The maximum energy conversion efficiencies for the Br*, CO₂, and NO lasers is 0.71, 0.16, and 0.012 percent respectively.

Comparisons are made between the three lasers' stimulated emission cross section, pump energy threshold, and gain. Analysis indicates a threshold for the Br*–NO laser of $2.31 \times 10^{-3} \text{ cm}^{-1}$, which corresponds to a required pump energy of approximately 3 mJ per pulse. Br* and CO₂ laser data matches the results previously obtained.

The poor energy efficiency obtained from the Br*–NO laser seems to make it a poor candidate for an operational infrared laser. Power and weight requirements dictate the development of a more efficient laser with operation in the 3 to 5 μm wavelength band.

V. *Conclusions and Recommendations*

A. *Conclusions*

Two areas of bromine kinetics are examined in this dissertation: phase one, the excitation and quenching of atomic bromine; phase two, an electronic-to-vibrational energy transfer gas-phase chemical laser.

1. *Summary of Bromine Quenching Rate Studies*

When molecular bromine is subjected to laser light near $\lambda = 400$ nm, nearly equal proportions of $\text{Br}(^2\text{P}_{3/2})$ and $\text{Br}(^2\text{P}_{1/2})$ are formed via the repulsive limb of the $\text{B}^3\Pi(0^+)$ state. The resulting weak $\text{Br}(^2\text{P}_{1/2} - ^2\text{P}_{3/2})$ fluorescence at $2.71 \mu\text{m}$ is monitored as a function of buffer gas pressure to determine quenching rate coefficients.

Pulsed lifetime studies are performed using an excimer-pumped dye laser providing 7 mJ per pulse at a wavelength of 480 nm in a 25 ns pulse at 25 Hz. Lifetime measurements of the quenching of $\text{Br}(^2\text{P}_{1/2})$ by Br_2 and CO_2 establish absolute room-temperature rate coefficients of $k_{\text{Br}_2} = 1.2 \pm 0.1 \times 10^{-12}$ and $k_{\text{CO}_2} = 1.5 \pm 0.2 \times 10^{-11} \text{ cm}^3/\text{molecule}\cdot\text{s}$. After establishing the absolute Br_2 quenching rate, steady-state photolysis methods are used to determine the quenching rates for the rare gases, N_2 , O_2 , H_2 , D_2 , NO , NO_2 , N_2O , SF_6 , CF_4 , CH_4 , CO , CO_2 , COS , SO_2 , H_2S , HBr , HCl , and HI relative to that for Br_2 .

Quenching rate temperature dependence is examined for Br_2 , CO_2 , N_2O , HCl , COS , NO , and NO_2 for temperatures from 290 to 420 K. The rates for N_2O , HCl , COS , and NO are essentially unaffected in this temperature

range, but the CO_2 quenching rate displayed a negative temperature dependence while the rate for NO_2 increased with increasing temperature. Analysis of the total atomic bromine concentration with and without the dissociating laser operating indicate that three body recombination does not affect the quenching rate measurements for the pressure regions of these experiments. Analysis further indicates that operation is primarily in the wall-limited pressure regime where diffusion does not affect rate measurements. Finally, experiments are performed to determine the slowest relative quenching rate measurable by this experimental technique.

The results from the steady-state quenching rate measurements are correlated with the energy defect between the quenching species energy and the 3685 cm^{-1} , $\text{Br}(^2\text{P}_{1/2})$ energy. Three theoretical approaches are examined to understand the possible mechanisms responsible for the electronic-to-vibrational energy transfer from $\text{Br}(^2\text{P}_{1/2})$ to the quenching species.

The steady-state photolysis techniques employed in this research offer a rapid means of measuring relative rate coefficients. By coupling these relative rates with well-known rates from pulsed photolysis experiments, an extensive data base for $\text{Br}(^2\text{P}_{1/2})$ quenching is reported. These results provide an opportunity for quantitatively assessing the efficiency of an infrared laser using atomic bromine as the energy carrier.

2. Summary of Laser Prototype Demonstration

Candidate laser molecules are selected based on the amount of energy transferred from $\text{Br}(^2\text{P}_{1/2})$, the acceptor molecules' ability to lase, and the lasing wavelength. Nitric oxide and CO_2 are chosen as prototype laser

systems due to their energy resonance with $\text{Br}(^2\text{P}_{1/2})$ and their reported laser wavelengths.

Initially, a photolytic, pulsed $\text{Br}(4^2\text{P}_{1/2} - 4^2\text{P}_{3/2})$ laser operating at $2.714\ \mu\text{m}$ is demonstrated by photodissociation of IBr at $532\ \text{nm}$ using a frequency-doubled Nd:YAG pump laser. Lasing is observed for pump energies from 25 to 125 mJ per pulse and for IBr pressures from 600 mTorr to 6.5 Torr.

To serve as a baseline for the NO laser, a CO_2 laser is demonstrated operating on the $(101 \rightarrow 100)$ transition at $4.3\ \mu\text{m}$ for CO_2 pressures from 200 to 700 mTorr with 2 Torr of IBr and for pump energies from 75 to 140 mJ per pulse. Then an NO laser is demonstrated operating on the $(v = 2 - 1)$ vibrational transition near $5.4\ \mu\text{m}$ for NO pressures from 100 mTorr to 1.4 Torr and for pump energies from 25 to 125 mJ per pulse. The ratio of laser energy for the CO_2 and NO pulsed lasers is 10 : 1, indicating an approximate NO laser energy of 0.01 mJ per pulse with 85 mJ per pulse pump energy. This corresponds to an approximate energy conversion efficiency of 0.012 percent. This poor energy conversion efficiency makes the NO laser a poor candidate for an operational infrared laser.

B. Recommendations

1. Electronic-to-Vibrational Energy Transfer Laser Development and Analysis

To determine the feasibility of a Br^* electronic-to-vibrational energy transfer laser, and in light of the poor efficiency of the Br^*-NO laser, research should continue on the development of a suitable acceptor molecule.

Analysis of the molecule's energy transfer rate into desired vibrational levels as well as its overall Br^* quenching rate allows better assessment of the candidate's feasibility. This analysis of potential acceptor molecules should be directed at determining the molecule's $\text{E} \rightarrow \text{V}$ energy transfer rate and stimulated emission cross section. By determining the product channels for the deactivation process, the potential population inversion between vibrational levels can be determined. N_2O has vibrational energy levels nearly resonant with Br^* , and should be considered as an acceptor laser species. Studies should also continue to further characterize the CO_2 transfer laser; the $4.3\text{ }\mu\text{m}$ wavelength is ideal for the desired application.

2. Steady-State Bromine Studies

Bromine photolysis research should also include an analysis of specific quenching species' energy channels. The steady-state photolysis techniques employed in this research offer not only a rapid means of measuring relative rate coefficients, but they also offer a means of analyzing steady-state spectroscopic and kinetic energy partitioning issues. Since CW experiments only provide relative quenching rates, pulsed photolysis techniques must be used to establish the absolute time base. Finally, steady-state bromine energy transfer lasers should be researched. The $\text{Br}^*\text{-CO}_2$ laser operating at $4.3\text{ }\mu\text{m}$ is one candidate for a steady-state laser considering its mode-specific energy transfer and the strength of the (101–100) laser transition.

VI. Bibliography

1. R. J. Donovan and D. Husain. "Chemistry of Electronically Excited Atoms," *Chemical Reviews*, 70: 509-516 (1970).
2. A. B. Hariri, Peterson, and Wittig. "Electronic-Vibrational Energy Transfer from Br($4^2P_{1/2}$) to HCN, and Deactivation of HCN(001)*," *Journal of Chemical Physics*, 65: 1872-1875 (September 1976).
3. V. S. Kushawaha. "Electronic to Vibrational Energy Transfer from Br* to N₂O," *Physica Scripta*, 20: 75-80 (1979).
4. S. R. Leone and F. J. Wodarczyk. "Laser-Excited Electronic-to-Vibrational Energy Transfer from Br($4^2P_{1/2}$) to HCl and HBr," *Journal of Chemical Physics*, 60: 314 (January 1974).
5. H. Hofmann and S. R. Leone. "Collisional Deactivation of Laser-Excited Br*($2^2P_{1/2}$) Atoms with Halogen and Interhalogen Molecules," *Chemical Physics Letters*, 54: 314-319 (March 1978).
6. A. B. Peterson, C. Wittig, and S. R. Leone. "Electronic-to-Vibrational Pumped CO₂ Laser Operating at 4.3, 10.6, and 14.1 μ m," *Journal of Applied Physics*, 47: 1051-1054 (March 1976).
7. A. B. Peterson, C. Wittig, and S. R. Leone. "Infrared Molecular Lasers Pumped by Electronic-Vibrational Energy Transfer from Br($4^2P_{1/2}$): CO₂, N₂O, HCN, and C₂H₂," *Applied Physics Letters*, 27: 305-306 (September 1975).
8. F. J. Wodarczyk and P. B. Sackett. "Electronic-to-Vibrational Energy Transfer from Br($4^2P_{1/2}$) to HF," *Chemical Physics*, 12: 65-70 (1976).
9. A. B. Hariri and C. Wittig. "Electronic to Vibrational Energy Transfer from Br($4^2P_{1/2}$) to CO₂, COS, and CS₂," *Journal of Chemical Physics*, 67: 4454-4462 (November 1977).
10. R. L. Pastel and others. "Efficient Br* laser pumped by frequency-doubled Nd:YAG and electronic-to-vibrational transfer-pumped CO₂ and HCN Lasers," *Chemical Physics Letters*, 183: 565-569 (September 1991).
11. C. W. Keenan, D. C. Kleinfelter, and J. H. Wood. *General College Chemistry*. New York: Harper and Row, 1980.

12. J. I. Steinfeld. *Molecules and Radiation*. Cambridge: The MIT Press, 1974.
13. I. A. Boriev and others. "Determination of the Emission Cross Section for the $^2P_{1/2} - ^2P_{3/2}$ Transition of the Bromine Atom," *Optical Spectroscopy (USSR)*, 54: 233-237 (March 1983).
14. G. Herzberg. *Atomic Spectra and Atomic Structure*. New York: Dover Publications, 1944.
15. H. Okabe. *Photochemistry of Small Molecules*. New York: John Wiley and Sons, 1978.
16. P. L. Houston. "Electronic to Vibrational Energy Transfer from Excited Halogen Atoms," *Advances in Chemical Physics*, Vol. 47, edited by J. Jortner, R. D. Levine, and S. A. Rice. New York: Wiley and Sons, 1981.
17. R. S. Mulliken. "The Interpretation of Band Spectra, Part III," *Reviews of Modern Physics*, 4: 1-88 (January 1932).
18. M. C. Heaven "Fluorescence Decay Dynamics of the Halogens and Interhalogens," *Chemical Society Review*, 15: 405-448 (1986).
19. R. F. Barrow, T. C. Clark, J. A. Coxon, and K. K. Yee. "The $B\ ^3\Pi(0_u^+) \leftarrow X\ ^1\Sigma_g^+$ System of Br_2 : Rotational Analysis, Frank-Condon Factors, and Long Range Potential in the $B\ ^3\Pi(0_u^+)$ State," *Journal of Molecular Spectroscopy*, 51: 428-449 (1974).
20. G. Herzberg. *Spectra of Diatomic Molecules*. New York: Van Nostrand Reinhold Company, 1950.
21. R. J. LeRoy, R. G. Macdonald, and G. Burns. "Diatom potential curves and transition moment functions from continuum absorption coefficients: Br_2 ," *Journal of Chemical Physics*, 65: 1485-1500 (August 1976).
22. H. Chang and S. Chen. "Photodissociation of Br_2 and the Electronic Raman Spectra of Br Under Argon Ion Laser Light," *Journal of Raman Spectroscopy*, 17: 453-458 (1986).
23. H. K. Haugen, E. Weitz, and S. R. Leone. "Accurate Quantum Yields by Laser Gain versus Absorption Spectroscopy: Investigation of Br/Br^* Channels in Photofragmentation of Br_2 and IBr ," *Journal of Chemical Physics*, 83: 3402-3412 (October 1985).

24. J. E. Smedley, H. K. Haugen, and S. R. Leone. "Laser Determinations of Hot Band Quantum Yields: $\text{Br}^*(^2\text{P}_{1/2})$ Formation in the Continuum Absorption of Br_2 at 510-550 nm," *Journal of Chemical Physics*, **87**: 2700-2708 (September 1987).
25. R. F. Tate. *Steady-State Production and Quenching of $\text{Br}(^2\text{P}_{1/2})$* . Masters Thesis. Air Force Institute of Technology, Wright-Patterson AFB, OH, October 1991.
26. G. Herzberg. *Electronic Spectra of Polyatomic Molecules*. New York: Van Nostrand Reinhold Company, 1966.
27. A. J. Grimley and P. L. Houston. "Electronic to Vibrational Energy Transfer from $\text{Br}(4^2\text{P}_{1/2})$ to H_2 , HD, and D_2 ," *Journal of Chemical Physics*, **70**: 5184-5189 (June 1979).
28. C. A. Taatjes, C. M. Lovejoy, B. J. Opansky, and S. R. Leone. *Laser Double Resonance Measurements of the quenching Rates of $\text{Br}(4^2\text{P}_{1/2})$ with H_2O , D_2O , HDO , and O_2* , Report to Phillips Laboratory, Advanced Concepts Branch, Kirtland AFB, NM, April 1991.
29. C. A. Wight. "Infrared Fluorescence Studies of Near-Resonant Electronic-to-Vibrational Energy Transfer Collisions: $\text{Br}(4^2\text{P}_{1/2}) + \text{NO}$," *Journal of Physical Chemistry*, **90**: 2683-2687 (1986).
30. A. J. Sedlacek and C. A. Wight. "Infrared fluorescence study of E-V energy transfer from $\text{Br}^*(4^2\text{P}_{1/2})$ to nitrosyl bromide," *Journal of Chemical Physics*, **86**: 2787-2792 (March 1987).
31. A. J. Sedlacek, R. E. Weston, and G. W. Flynn. " $\text{Br}^* + \text{CO}_2$ revisited: An investigation of E-V energy transfer with time-resolved diode laser spectroscopy," *Journal of Chemical Physics*, **93**: 2816-2818 (August 1990).
32. H. Reisler and C. Wittig. "Temperature dependence of the quenching of $\text{Br}(4^2\text{P}_{1/2})$ by CO_2 and HCl with accompanying vibrational excitation," *Journal of Chemical Physics*, **68**: 3308-3309 (April 1978).
33. H. Reisler and C. Wittig. "Temperature dependence of electronic to vibrational energy transfer from $\text{Br}(4^2\text{P}_{1/2})$ to $^{12}\text{CO}_2$ and $^{13}\text{CO}_2$," *Journal of Chemical Physics*, **69**: 3729-3734 (October 1978).
34. J. I. Cline and S. R. Leone. "Temperature Dependence of the Quenching of $\text{I}^*(^2\text{P}_{3/2})$ by I_2 from 300 to 800 K," *Journal of Physical Chemistry*, **95**: 2917-2920 (1991).

35. A. B. Peterson, L. W. Braverman, and C. Wittig. "H₂O, NO, and N₂O infrared lasers pumped directly and indirectly by electronic-to-vibrational energy transfer," *Journal of Applied Physics*, 48: 230-233 (January 1977).
36. G. P. Perram, et al. "Radial diffusion between coaxial cylinders and surface deactivation of O₂(b ¹Σ_g⁺)," *Chemical Physics*, 162: 427-432 (March 1992).
37. D. J. Seery and D. Britton. "The Continuous Absorption Spectra of Chlorine, Bromine, Bromine Chloride, Iodine Chloride, and Iodine Bromide," *Journal of Physical Chemistry*, 68: 2263-2266 (August 1964).
38. J. O. Hirshfelder, C. F. Curtiss, and R. B. Bird. *Molecular Theory of Gases and Liquids*. New York: John Wiley and Sons, 1954.
39. J. J. Ewing. "Calculation of Spin Orbit Relaxation Rates by Near Resonant E → V Energy Transfer," *Chemical Physics Letters*, 29: 50-55 (November 1974).
40. I. H. Zimmerman and T. F. George. "Theoretical Study of Isotope Effects in the Quenching of Electronically Excited Halogen Atoms H₂, HD, and D₂," *J. C. S. Faraday Transactions II*, 71: 2030-2042 (1975).
41. S. Lemont and G. W. Flynn. "Vibrational State Analysis of Electronic-to-Vibrational Energy Transfer Processes," *Annual Reviews of Physical Chemistry*, Vol. 28, edited by B. S. Rabinovitch, J. M. Schurr, and H. L. Strauss. Palo Alto, CA: Annual Reviews, Inc., 1977.
42. J. Finzi and Bradley Moore. "Relaxation of CO₂(10⁰1), CO₂(02⁰1), and N₂O(10⁰1) vibrational levels by near-resonant V → V energy transfer" *Journal of Chemical Physics*, 63: 2285-2288 (September 1975).
43. F. P. Billingsley. "Calculated Vibration-Rotation Intensities for NO(X ²π)," *Journal of Molecular Spectroscopy*, 61: 53-70 (1976).
44. G. Chandraiah and C. W. Cho "A Study of the Fundamental and First Overtone Bands of NO in NO-Rare Gas Mixtures at Pressures up to 10,000 PSI," *Journal of Molecular Spectroscopy*, 47: 134-147 (1973).

Appendix A: Photolysis Experiment System Operation and Procedures

This appendix details the procedures used in the steady-state and pulsed photolysis experiments.

A. Argon Ion Laser and Detector Alignment

The Ar^+ laser beam is centered on the reaction cell entrance window. With the cell at atmospheric pressure, one of the gas inlet connectors is removed. With the argon laser still on, freon or a similar aerosol is sprayed into the cell. The laser light is scattered by the aerosol, and offers a line of 488 nm light which is used to coarse align the InSb detector. After positioning the 50 and 100 mm CaF_2 lens at their respective focal lengths from the Br^* fluorescence line and InSb detector element, the scattered laser light from the aerosol is focused on the detector. Fine adjustments to both lens and detector positions are made to obtain the sharpest image on the detector. A white piece of paper is positioned in front of the detector window to aid in viewing the image. The vertical direction is the most critical for detector positioning; slight adjustments make a large difference in detected signal. When focusing the image on the detector, the image focus is positioned just behind the window since the detector element is a few mm behind the window. After the lens set and detector are coarse aligned, the cell is returned to vacuum.

After the cell pressure reaches less than one mTorr, distilled molecular bromine is flowed into the reaction cell while insuring the cell exit valves are closed. One to two Torr of bromine provides the best emission intensity due

to Br₂ absorption of the photodissociating laser power. With the 2.71 μm filter on the detector, the detector is slowly rastered until the signal on the lock-in amplifier is maximized. The phase of the lock-in amplifier is adjusted for maximum signal either manually or by computer control. Finally, fine adjustments are made to the lens' and detector positions to maximize the signal intensity.

B. Pulsed Laser Alignment and Oscilloscope Signal Averaging

The pulsed laser is aligned by overlapping the dye beam on the Ar⁺ beam. In this way, the detector requires only small changes in position to optimize the pulsed Br* signal on the oscilloscope.

The main problem observed in collecting the pulsed lifetime data is the electrical noise from the excimer laser. *Oscilloscope background subtraction* and signal averaging are used to reduce these noise effects.

With the excimer and dye lasers operating and the reaction cell empty, a signal is collected on the oscilloscope using arithmetic averaging of between 1000 and 3000 samples. This background signal is stored in the oscilloscope memory and then subtracted from the Br* signal. This subtraction method removes the electrical noise component from the Br* signal-plus-noise collected. The number of signals averaged depends on the amount of bromine and buffer gas in the reaction cell. Greater concentrations of Br₂ result in averaged signals with higher signal-to-noise ratios. It is sometimes necessary to store a new background signal if adequate signal-to-noise ratios are not obtained.

C. Gas Handling

During a steady-state experiment, the reaction cell is filled with distilled molecular bromine while monitoring the cell pressure. Bromine is slowly brought into the cell until the desired quiescent Br₂ pressure is obtained. Proper cell *curing* time can be as long as an hour. When the cell reaches the desired pressure, which depends on the buffer gas quenching rate, the data collection software is started, and buffer gas is added to the cell. The buffer gas flow rate depends on its quenching rate, and is adjusted until there is a smooth transition between the initial and final Br* signal intensities. The lock-in amplifier time constant is set to a value that averages out noise in the Br* signal while still responding to changes in the emission intensity; nominally 1 to 3 seconds. Initial lock-in amplifier voltages of 20 to 25 microvolts are nominal, and final voltages are below 5 microvolts. This voltage change insures that the Br* emission intensity changes enough to obtain an adequate quenching-rate fit to the data. After the experiment, absorption data are inspected to insure the Br₂ concentration remained constant during the experiment. If the concentration changed during the experiment, the buffer gas flow and data collection rates are adjusted and another experiment is performed.

During a pulsed photolysis experiment, cell pressure is maintained during each data averaging period to insure the pulse lifetimes are properly correlated with each pressure.

Caution is used during all gas handling since the bromine and many buffer gases are hazardous. On-line detectors are mounted near the reaction cell when NO and HCl are used. Material Safety Data Sheets are reviewed before each buffer gas is used.

After the procedure is completed, all gases are removed from the reaction cell and attached gas tubing through the cold trap. The trap is emptied when all gas has been cleared from the gas lines.

D. Data Collection

All steady-state photolysis experiment data are collected on the personal computer using Metrabyte *TLABLOG* software. The data collection rate is adjusted to provide from 2000 to 4000 data samples per experiment while meeting the constraints of the gas flow and mixing rates. The data are stored as ASCII characters in scientific notation and are then read into a Microsoft Excel spreadsheet for analysis and plotting.

Appendix B: Bromine Distillation and Purification

As mentioned above, proper molecular bromine distillation and purification are necessary to eliminate molecular quenching and emission. Following published guidelines for the transportation of bromine, a sample is placed in one of the two glass bulbs described above and sealed. The figure below shows the two bulbs and the associated valves.

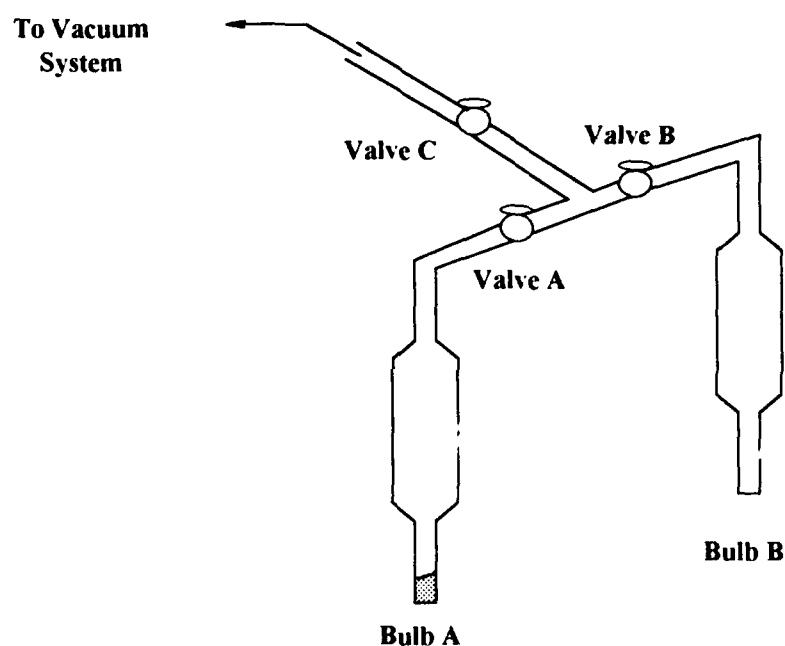


Figure B.1. Bromine distillation and purification schematic diagram.

With a cold trap on the vacuum system, the bulb containing the bromine, bulb A for example, is open to the vacuum by opening valve A on the bulb and valve C to the vacuum system. This procedure removes some of the bromine vapor, but it also removes the air from the bulb. After a few seconds, valve A is closed. Then liquid nitrogen (LN_2) is placed in a vacuum dewar around the empty bulb B. The LN_2 must cover enough of the bulb to

enclose the liquid bromine. Valve C is closed to isolate the bulbs from the vacuum system.

With LN_2 surrounding bulb B, valve A is opened. Immediately bromine vapor is pulled from bulb A to bulb B and freezes on the bulb sides at a level below the LN_2 . The bromine sample in bulb A may also freeze; opening and closing valve A every few minutes will allow the bromine in bulb A to nearly all transfer to bulb B. At that time, valve C is opened while bulb B is still surrounded by LN_2 . Any remaining bromine in bulb A is pulled from the bulb into the cold trap, and contaminants are pulled from the frozen bromine in bulb B. The system is pumped on for a few minutes as the pressure drops to a few millitorr on the Baratron.

This freeze-thaw cycle is repeated several times until few impurities are pulled from the remaining sample. This sample purity is indicated by a small increase in pressure as valve C is opened. In order to remove the molecular contaminants water and carbon dioxide, further purification is necessary.

With bulb A containing the bromine, and with valves A and C closed, bulb A is submerged in an H_2O ice and NaCl salt slurrice. The temperature is monitored with a temperature probe to insure that it is below 0°C . Then with LN_2 surrounding bulb B, valve A is again opened. Any remaining water is frozen in bulb A, and the bromine which has a vapor pressure below 0°C is cryogenically pumped to bulb B. After most of the bromine is removed from bulb A, valve A is closed. Valves B and C are then closed after the pressure reaches a few millitorr.

After removing the LN_2 from around bulb B and allowing the bromine to thaw, a slurrice of acetone and LN_2 is prepared as follows. With a dewar

partially filled with acetone surrounding bulb B, LN_2 is slowly added while monitoring the temperature. The acetone and LN_2 slurry can reach a temperature of -86°C , but for this application, LN_2 is added until the temperature reaches approximately -65°C . This temperature reduces the bromine vapor pressure to near zero while allowing the CO_2 to be pulled off. Next valves B and C are opened, and any CO_2 impurities are removed. Finally, the acetone slurry is removed, and the remaining bromine in bulb A is discarded using approved procedures. Phosphorus pentoxide (P_2O_5) may be added to a reservoir near the bromine storage bulb to remove any residual water vapor.

The purified bromine sample may now be used. After each experiment, the bromine in the reaction cell and tubing is discarded via the cold trap as impurities can be reintroduced into the bromine sample. By LN_2 freezing and vacuum pumping on the bromine sample for a few minutes before each experiment, the sample purity is maintained.

Appendix C: Bromine Laser Cavity and Detector Alignment

This appendix details the procedures used to properly align the YAG pump laser, the bromine laser cavity, and the HgCdTe detector used in the prototype laser demonstrations.

Referring to Figure C.1, the He-Ne beam is turned and directed toward the pellicle beam splitter which splits a portion of the He-Ne beam in the direction of the laser axis. This beam is used to coarse align the cavity mirrors M1 and M2 and the HgCdTe detector. A portion of the Ne-Ne beam travels through the pellicle beam splitter, and proper alignment of the cavity positions light from multiple passes through the pellicle beam splitter onto the initial, first-pass spot. In addition to using this procedure, pin holes are positioned near M1 and M2 to aid the alignment procedure. After the cavity is aligned using the He-Ne, prisms P1 and P2 are positioned approximately 1 to 3 mm from the Ne-Ne beam. The prisms should be as close to the He-Ne beam as possible to insure the YAG pump beam overlaps as much of the aligned cavity as possible without blocking the laser path.

The HgCdTe detector is positioned so the He-Ne light scattered from the Brewster window illuminates the detector element. The detector is positioned as close to the Brewster window as possible to reduce dispersion effects between the He-Ne and infrared wavelengths. An interference filter is positioned before the detector element to select the desired infrared laser wavelength.

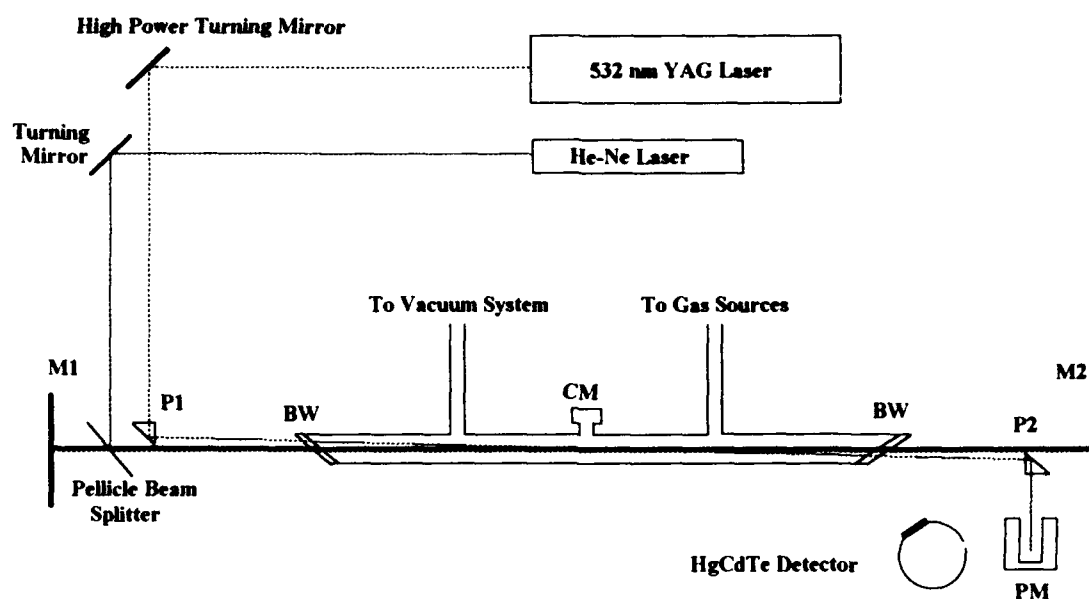


Figure C.1. Laser demonstration apparatus.

The 532 nm doubled YAG output is turned via an Oriel high-power, 1 inch diameter turning mirror which has a maximum reflectivity at 532 nm. The YAG power is kept as low as possible while still maintaining lasing. With the mirrors blocked, the high-power mirror is adjusted to direct the pump laser into prism P1. Prisms P1 and P2 are then aligned to direct the pump beam through the laser tube and into the power meter (PM). Care is taken to insure that the pump energy hits prism P2 which turns the pump beam before it hits the laser mirror M2. By positioning the prisms 1 to 3 mm from the laser axis (He-Ne beam) and the pump beam on the edges of the prisms, differences between the pump and laser beam are kept to 4 mrad or less. This small angle provides sufficient overlap in the pump laser and laser cavity mode volumes while avoiding damage to the resonator optics.¹⁰

After the cavity is coarse aligned, the resonator mirrors are unblocked and the pellicle beam splitter is removed. IBr is flowed into the cell, and the laser experiments begin.

Appendix D: E → V Energy Transfer Theoretical Mechanisms

As stated, the three theoretical models of electronic-to-vibrational energy transfer theories predict a strong dependence of the E → V quenching rate on ΔE and ΔV . This appendix provides more details of these models.

A. Quantum Mechanical Calculations

This theory seeks to determine the probability of E → V energy transfer by treating the electronic and nuclear motions classically. It is then possible to characterize resonant interactions between electronic and nuclear motion. First, the potential energy surfaces correlating to the two spin-orbit split atomic states and two nonreactive surfaces and coupling terms are derived. Then quantum mechanical calculations are carried out for the collisions between the spin-orbit states of the atom and vibrational states of the molecule to determine the transition probabilities. Finally, a kinetic model is used to predict quenching cross sections.⁴⁰

The quantum mechanical calculations correctly predict the experimental observations that the quenching is dominated by the E → V channel and that the quenching rate is a sensitive function of ΔE and ΔV . The main limitations of the model are the time required for the calculations and the inability of including rotational degrees of freedom in an exact way.¹⁶

B. Long-Range Attractive Forces

This theory models the $E \rightarrow V$ energy transfer based on the idea that long-range attractive forces couple the electronic and vibrational degrees of freedom. First order probability theory is used to calculate the probability for the $E \rightarrow V$ transition given by

$$P = \hbar^{-2} \left| \int_{-\infty}^{\infty} \langle i | V | f \rangle \exp\left(\frac{i \Delta E t}{\hbar}\right) dt \right|^2 \quad (\text{D.1})$$

where $\Delta E = \hbar\omega$ and $V(t)$ is the interaction potential.¹⁶ For the case of a small $(\omega b/v)$, where b is the impact parameter and v is the velocity, the dipole-quadrupole interaction averaged over temperature and impact parameter, $V(t)$, is given by

$$V(t) = \frac{3 \pi^2 \mu |\mu_{if}^M|^2 |Q_{if}^X|^2}{64 \hbar^2 \sigma^2 k T} \quad (\text{D.2})$$

where

μ = reduced mass

μ_{if}^M = dipole matrix element term for the molecule

Q_{if}^X = quadrupole matrix element term for the atom

σ = hard-sphere collision diameter

where the matrix element μ_{if}^M correctly predicts the decrease in cross section with increasing ΔV . For large $(\omega b/v)$, the deactivation probability falls off as $\exp(-\omega b/v)$, in agreement with the experimental results. Finally, the

probability term given in Equation (D.2) has an inverse T dependence, and since the transition probabilities are calculated between initial and final vibrational states, the model is state selective in transferring the energy.¹⁶

C. *Curve Crossing Mechanisms*

The curve crossing theory is based on the idea that the $E \rightarrow V$ energy transfer involves a crossing between the zero-order potential curve correlating to $\text{Br}^* + \text{A}(0)$ and that correlating to $\text{Br} + \text{A}(\nu)$. The reactants move along the upper curve until they cross an excited state of the lower curve and then undergo a nonadiabatic transition to the lower curve. This transition results in the deactivation of the atom and the vibrational excitation of the molecule.¹⁶ The probability of a single crossing given by the Landau-Zener formula is

$$P_{EV} = 1 - \exp\left(\frac{-2\pi|V_{if}|^2}{\Delta F \hbar \nu}\right) \quad (\text{D.3})$$

where

V_{if} = the matrix element of the intersection

$\Delta F \approx \Delta E \alpha$

α^{-1} = the length over which the coupling between the potential curves is strong

The matrix element V_{if} which includes the normal vibrational contribution, falls off rapidly as ΔV increases. Also, since ΔF is proportional

to the energy defect, the probability of transfer falls off exponentially as ΔE increases. For low probabilities of transfer, Equation (D.3) predicts that $\ln(P_{EV})$ will have an approximate $T^{-1/2}$ dependence.¹⁶

After a curve crossing occurs, the complex is typically on a steeply-repulsive ground-state potential surface. Vibrational excitation of the molecule is believed to arise mainly from impulsive forces as the collision partners recede. The impulsive interaction generally leads to a broad distribution of vibrational states in contrast to the state-specific energy transfer in the long-range forces model.²⁹

These three theories all predict a strong dependence of the $E \rightarrow V$ energy transfer in ΔE and ΔV . While temperature studies help determine which mechanism is responsible for the energy transfer, it is likely that both short and long range forces play an important role in the energy transfer process.

Appendix E: Error Analysis

The errors quoted in this dissertation are standard deviations from the mean of the individual experiments in each data set. In the case of the pulsed photolysis experiments, the error bars on each data point in the Stern-Volmer plots are standard deviations of the exponential fits to the fluorescence lifetimes. The error associated with each Stern-Volmer linear fit to determine the rate coefficient is consistently less than the error from experiment-to-experiment variations.

The pulsed lifetime data consists of many data points (typically 2000) for each individual gas pressure. The fit to this data typically depends on the data signal-to-noise ratio, which is nominally 15 or greater. Errors associated with lifetime fits are 10 percent or less. Then data for several pressures (usually 20 or less) are then presented in a Stern-Volmer plot. A linear fit is then made to these few data points. Even though the error associated with this rate-coefficient fit is typically greater than that from the lifetime fits, the experiment-to-experiment variation is still greater. One reason for this fact is that results from individual experiments are affected by the combination of all errors, experimental and systematic.

The steady-state experimental data are slightly different. The data are very dense for individual experiments enabling excellent data fits with very high signal-to-noise ratios. Since data are sampled very closely in abscissa points (pressure, temperature, etc.), the data plots are essentially continuous. For example, during quenching experiments, the pulsed data are taken at a few pressures, while the CW experiment provides emission intensity every few milliTorr. In every case, the experiment-to-experiment

variation is greater than the error for individual experiments. The near continuity of the steady-state data is one of the big advantages of CW experiments over pulsed experiments. As shown above, the signal-to-noise ratio obtained from the fluorescence experiments scales approximately with average laser power, and the CW laser provides about four times more average power than the excimer-pumped dye laser.

In addition to the data-fitting and experiment-to-experiment errors mentioned above, there are additional experimental errors. The first error is the measurement of gas pressures. The total cell pressure is measured with a capacitance manometer which is rated at 0.12 percent of the pressure reading. The manometer is zeroed by evacuating the system to 10^{-5} Torr with the diffusion pump. There are also errors due to small changes in pressure during each *constant-pressure* experiment. Even after reaction cell *seasoning*, as explained in the experiment section, bromine and buffer gas is adsorbed by the reaction cell and connecting tubing, thereby changing the total cell pressure during the time of the experiment. Steps are taken to minimize this effect, and typical pressure changes of only a few milliTorr are observed during individual experiments.

Another source of experimental error is gas purity. Impurities in buffer gases can cause errors in quenching rate determinations. Water and carbon dioxide are the main impurities that affect quenching rate measurements. Both impurities have large Br^* quenching rates, and if they contaminate a buffer gas with a very low quenching rate such as the rare gases, errors can occur. The rare gases are typically 99.999 percent pure. If the impurity is fifty percent water, with a Br^* quenching rate of $5.1 \times 10^{-11} \text{ cm}^3/\text{molecule-s}$, rate measurements for buffer gases whose rates are

$1.3 \times 10^{-15} \text{ cm}^3/\text{molecule-s}$ are 20 percent in error. None of the current quenching rate measurements are below $3.3 \times 10^{-15} \text{ cm}^3/\text{molecule-s}$, and the lowest previous rate measurement is for argon; $< 2 \times 10^{-16} \text{ cm}^3/\text{molecule-s}$. These rates indicate that buffer gas impurities only slightly effect the slowest quenching rate determinations.

Considering all sources and the propagation of errors, a total error of 25 percent is estimated for all steady-state and pulsed experiment measured values.

Appendix F: Buffer Gas Purity

The gases used in all experiments are at least laboratory grade, and with the exception of bromine and iodine monobromide, they are used without further purification. Table F-1 provides a list of the gases used and their respective minimum purities.

Table F.1

Table of Buffer Gases, Manufacturer, and Purities

Gas	Manufacturer and Purity
Argon (Ar)	Airco 99.999 %
Bromine (Br ₂)	Spectrum 99.5 %
Halocarbon 14 (CF ₄)	Matheson 99.9 %
Methane (CH ₄)	Matheson 99.97 %
Carbon Monoxide (CO)	Matheson 99.99 %
Carbon Dioxide (CO ₂)	Matheson 99.995 %
Carbonyl Sulfide (COS)	Matheson 97.5 %
Deuterium (D ₂)	Matheson 99.5 %
Hydrogen (H ₂)	Matheson 99.9995 %
Hydrogen Sulfide (H ₂ S)	Matheson 99.0 %
Helium (He)	Airco 99.999 %
Hydrogen Bromide (HBr)	Matheson 99.99 %
Hydrogen Chloride (HCl)	Matheson 99.999 %
Hydrogen Iodide (HI)	Matheson 98.0 %
Iodine Monobromide (IBr)	Aldrich 98 %
Krypton (Kr)	Matheson 99.997 %
Nitrogen (N ₂)	Airco 99.999 %
Neon (Ne)	Matheson 99.996 %
Nitric Oxide (NO)	Matheson 99.0 %
Nitrogen Dioxide (NO ₂)	Matheson 99.5 %
Nitrous Oxide (N ₂ O)	Matheson 99.99 %
Oxygen (O ₂)	Airco 99.994 %
Sulfur Hexafluorine (SF ₆)	Airco 99.9 %
Sulfur Dioxide (SO ₂)	Matheson 99.98 %
Xenon (Xe)	Matheson 99.997 %

Vita

Capt Ray O. Johnson was born in Kansas City, Missouri on 25 May 1955. He enlisted in the United States Air Force on 13 February 1975. He graduated from Oklahoma State University in May 1984 with a degree of Bachelor of Science in Electrical Engineering. He received a commission in the Air Force from Officer Training School in August 1984, where he was an honor graduate. He was assigned to HQ Foreign Technology Division as a Foreign Telecommunications Analyst until entering the School of Engineering, Air Force Institute of Technology (AFIT), in June 1986. Upon graduating with a Masters Degree in Electrical Engineering in December 1987, he was assigned to HQ Strategic Air Command as the Head Quarter's Low Observable Engineer. In July 1990, he returned to AFIT for work on a doctorate. He is a member of Phi Kappa Phi and Eta Kappa Nu, and a past chapter president of Tau Beta Pi. He is married to the former Joan I. Vance, and they have three children.

Next Assignment: WL/AARI

WPAFB, OH 45433

REPORT DOCUMENTATION PAGE			Form Approved OMB No. 0704-0188	
Public reporting burden for this collection of information is estimated to average 1 hour per response, including the time for reviewing instructions, searching existing data sources, gathering and maintaining the data needed, and completing and reviewing the collection of information. Send comments regarding this burden estimate or any other aspect of this collection of information, including suggestions for reducing this burden, to Washington Headquarters Services, Directorate for Information Operations and Reports, 1215 Jefferson Davis Highway, Suite 1204 Arlington, VA 22202-4302, and to the Office of Management and Budget, Paperwork Reduction Project (0704-0188), Washington, DC 20503				
1. AGENCY USE ONLY (Leave blank)	2. REPORT DATE August 1993	3. REPORT TYPE AND DATES COVERED Doctoral Dissertation, Mar 92-Aug 93		
4. TITLE AND SUBTITLE Excited Atomic Bromine Energy Transfer and Quenching Mechanisms		5. FUNDING NUMBERS		
6. AUTHOR(S) Ray O. Johnson, Captain, USAF				
7. PERFORMING ORGANIZATION NAME(S) AND ADDRESS(ES) Department of the Air Force Air Force Institute of Technology/ENP 2950 P Street Wright-Patterson AFB, OH 45433-7765		8. PERFORMING ORGANIZATION REPORT NUMBER AFIT/DS/ENP/93-05		
9. SPONSORING/MONITORING AGENCY NAME(S) AND ADDRESS(ES) Phillips Laboratory (Dr. E. A. Dorko and G. D. Hager) PL/LID Kirtland AFB, NM 87117-6008		10. SPONSORING/MONITORING AGENCY REPORT NUMBER		
11. SUPPLEMENTARY NOTES				
12a. DISTRIBUTION/AVAILABILITY STATEMENT Approved for public release; distribution unlimited		12b. DISTRIBUTION CODE		
13. ABSTRACT (Maximum 200 words) See attached.				
14. SUBJECT TERMS Bromine, energy transfer laser, nitric oxide, spin-orbit relaxation rates, electronic-to-vibrational energy transfer			15. NUMBER OF PAGES 178	
			16. PRICE CODE	
17. SECURITY CLASSIFICATION OF REPORT Unclassified	18. SECURITY CLASSIFICATION OF THIS PAGE Unclassified	19. SECURITY CLASSIFICATION OF ABSTRACT Unclassified	20. LIMITATION OF ABSTRACT UL	